Carbon nanofiber electrodes for PEM fuel cells

Carbon nanofiber electrodes for PEM fuel cells

Serdar Çelebi

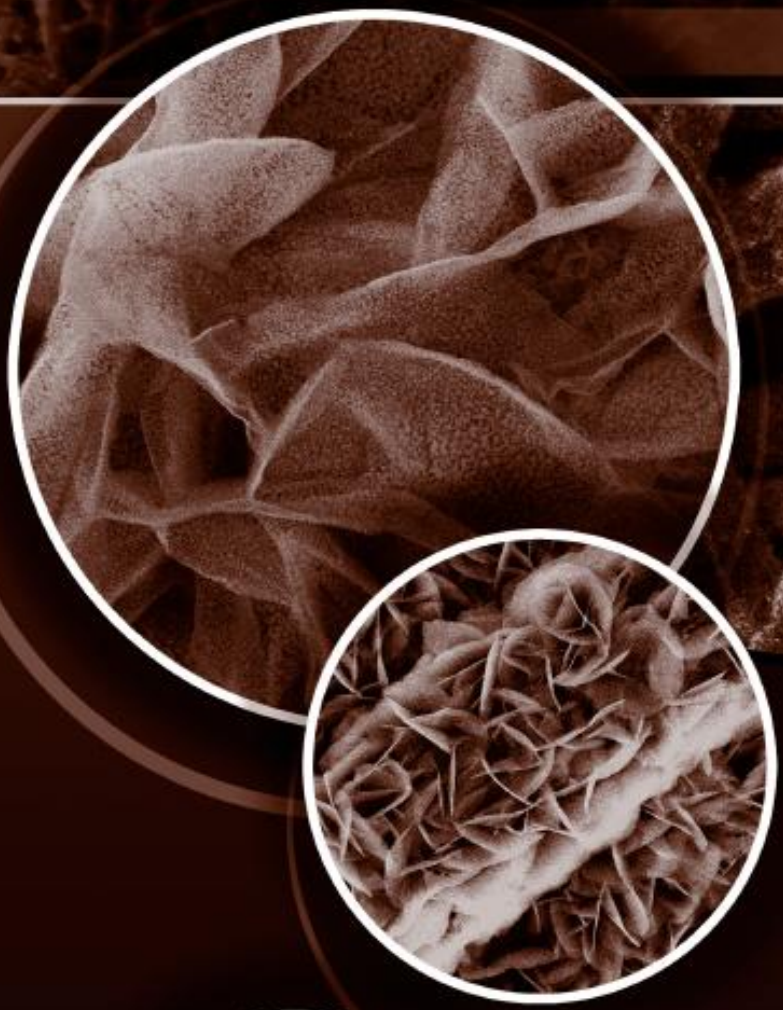

Carbon Nanofiber Electrodes for PEM Fuel Cells

PROEFSCHRIFT

ter verkrijging van de graad van doctor aan de
Technische Universiteit Eindhoven, op gezag van de
rector magnificus, prof.dr.ir. C.J. van Duijn, voor een
commissie aangewezen door het College voor
Promoties in het openbaar te verdedigen
op dinsdag 2 oktober 2012 om 16.00 uur

door

Serdar Çelebi

geboren te Istanbul, Turkije

Dit proefschrift is goedgekeurd door de promotoren:

prof.dr.ir. J.C. Schouten
en
prof.dr. F.A. de Bruijn

Copromotor:
dr.ir. T.A. Nijhuis

The work described in this thesis was carried out at the Laboratory of Chemical Reactor Engineering, Eindhoven University of Technology, The Netherlands and financed by the Dutch Ministry of Economic Affairs within the framework of EOS-LT funded through SenterNovem.

A catalogue record is available from the Eindhoven University of Technology Library
Carbon Nanofiber Electrodes for PEM Fuel Cells
ISBN: 978-90-386-3187-5

Cover design: Marina Khlytina, m.n.khlytina@gmail.com
Printed by Ipskamp Drukkers B.V., Amsterdam, The Netherlands

To my parents,

To my brother,

To my love, Aysun...

Summary

Carbon Nanofiber Electrodes for PEM Fuel Cells

Increasing energy demand in the world and the environmental concerns due to air pollution and the green house effect of fossil fuels stimulate the research into renewable alternative energy resources. Among these alternatives, hydrogen has a life changing opportunity for the human being for the future. The chemical energy stored in hydrogen can be converted into electricity via various types of fuel cells. The proton exchange membrane (PEM) fuel cell is the most promising type providing high power densities at operating temperatures typically less than 100 °C. The necessity of increasing the platinum utilization in PEM fuel cells, due to its cost and availability, requires an optimization of the catalyst support and the gas diffusion layers. In many long term fuel cell tests, a decrease in water removal capacity leads to a gradual decrease of the PEM fuel cell performance. The use of more graphitic and highly oriented carbon as an alternative material for use in the gas diffusion media combines a high electronic conductivity with an acceptable surface area.

One approach, introduced in this thesis, is the direct growth of carbon nanofibers (CNFs) on a gas diffusion layer providing a strong network with a high surface area. Two methods are developed for the direct growth of CNFs on a carbon based gas diffusion layer: CNF growth via nickel complex particles (chapter 2) and via homogeneous deposition precipitation of nickel (chapter 3). The production of CNF grown carbon paper via the nickel complex particles was rather fast compared to the homogeneous deposition precipitation of nickel, since deposition of nickel complex particles on a carbon paper took less than one hour whereas it took more than two days for the homogeneous deposition precipitation of nickel. The time of the deposition of nickel hydroxide in the deposition

precipitation depends upon the decomposition rate of urea at the deposition temperature. Since the deposition was carried out near the boiling point of water, the decomposition rate of urea was nearly constant. It was attempted to increase the total amount of nickel by working with highly concentrated nickel and urea solutions. However, this caused a non-uniform deposition of nickel hydroxide which resulted in the detachment of CNFs during ultrasonic treatments. The loading of the nickel catalyst was controlled precisely during homogeneous deposition precipitation of nickel on carbon paper in this slow deposition process. In addition, the growth of nickel hydroxide layers covered the entire surface of the carbon paper and thereby closed the pores bigger than 1 μm. In our experiments, it was observed that open pores on the CNF grown carbon paper surface caused instabilities in operation due to water accumulation at these locations of the cathode compartment of the PEM fuel cells. Considering the two main factors described here, homogeneous deposition precipitation of nickel was utilized to obtain a highly controlled nickel deposition and thereby a highly controlled CNF loading on the carbon papers.

The decoration of carbon paper with CNFs was investigated as a water management layer (chapters 4 and 5) and as a direct catalyst layer for platinum (chapter 6) in order to give more accessibility for the gas transport. The CNF grown carbon paper provided effective gas diffusion to the catalyst layer when they were used as a water management layer, especially under high gas flows. It suffered from performance losses at the mid-current density region (400-800 $mA \cdot cm^{-2}$), which can be improved by increasing the loading of a hydrophobic polymer. The CNF grown carbon paper can be a good alternative as a catalyst support, however, further optimization of the Nafion-platinum contact is required to get the benefits of using CNF grown carbon paper as a direct catalyst layer.

Table of Contents

1 Introduction

Before the industrial revolution, nobody would imagine that the energy need of our world could exponentially increase in the 20th century, which can also be named as the hydrocarbon century, because of the untouched fossil fuel resources. In today's world, nearly 75 % of the total energy consumption is provided by fossil fuels including petroleum, gas and coal, which brings environmental risks. Primary emissions of fossil fuels such as sulfur, nitrogen and carbon pollute air and decrease the air quality and even produce acid rains directly causing health problems. Massive CO_2 release of fossil fuels used in daily life is one of the key factors for the global warming. The global atmospheric concentration of CO_2 has started to increase exponentially in the 20th century and reached to 390 ppm (2008) from 310 ppm (1958) reported by the Institution of Oceanography (Hawaii, USA) [1]. The average global air temperature rose by between 0.3 and 0.6 °C in this time interval as reported by the climatic research unit in Norwich, UK [2]. Increasing demand for energy in the developing countries and the potential environmental effects of fossil fuels stimulate the research into renewable alternative energy sources. Among these alternatives, hydrogen has a life changing opportunity for the human being for the future. Hydrogen is not a primary energy source like coal or gas, on the contrary; it is a non-toxic energy storage and transport medium. Hydrogen is mostly produced by fossil fuel resources (96 %) including gas (~ 49 %), crude oil (~29 %), and coal (~18 %) and by the electrolysis of water (~4 %) using nuclear energy and renewable sources such as geothermal, solar and wind energy [IHS

chemical, 2010]. Renewable sources are of crucial importance providing carbon-free energy conversion pathways. However, as indicated, the production of hydrogen mainly depends on fossil fuels; therefore the air pollution created by hydrogen is expected to be nearly the same as gasoline or diesel. Moreover, the cost of the installation of the facilities for the production of the renewable energy is rather high in the short term, which extends the time to pass to fully hydrogen fuelled vehicles.

The chemical energy conversion of this lightest, colorless, odorless gas, hydrogen, into electricity is performed by fuel cells as described by Schönbein and Grove in 1839 [3, 4]. A fuel cell is generally described as a device which converts the chemical energy into electricity using an oxidant. The fuel can be hydrogen as well as a fossil fuel like methanol. Fuel cells run on the redox principle where the fuel is oxidized at the anode compartment of the cell and the oxidant is reduced at the cathode compartment with incoming ions passing through the electrolyte and electrons travelling through the external current collectors.

The electrolyte does not only function as an ion conductor but also as a barrier to prevent the mixing of the fuel and the oxidant. Various types of fuel cells are available and classified with respect to the kind of electrolyte material employed in the cell. Proton exchange membrane (PEM) fuel cells, alkaline fuel cells, phosphoric acid fuel cells, molten carbonate fuel cells and solid oxide fuel cells are such examples. The type of the fuel, the operating temperature range, and the catalysts used in these cells are very different from each other, which in turn affect the application area.

1.1 Proton exchange membrane (PEM) fuel cell

A significant effort has been given to develop PEM fuel cells for transport and portable applications. PEM fuel cells produce a higher power density and offer a favorable power to weight ratio and volume compared with the other fuel cell types. They operate at relatively low temperatures around 60-80 °C, which allow a quicker start. They are typically fuelled with pure hydrogen and air. A PEM fuel

cells consists of two catalyst layers where oxidation and reduction take place, gas diffusion layers, microporous layers (water management layers), current collectors and a polymer electrolyte. The sandwich structure of these components illustrated in Figure 1.1 is named as membrane electrode assembly (MEA). In a PEM fuel cell, hydrogen is introduced to the anode side of the MEA, where it is oxidized to protons and electrons on a platinum (Pt) catalyst. The generated protons migrate through a proton exchange membrane to the Pt catalyst at the cathode where oxygen is reduced to water in the presence of protons and electrons.

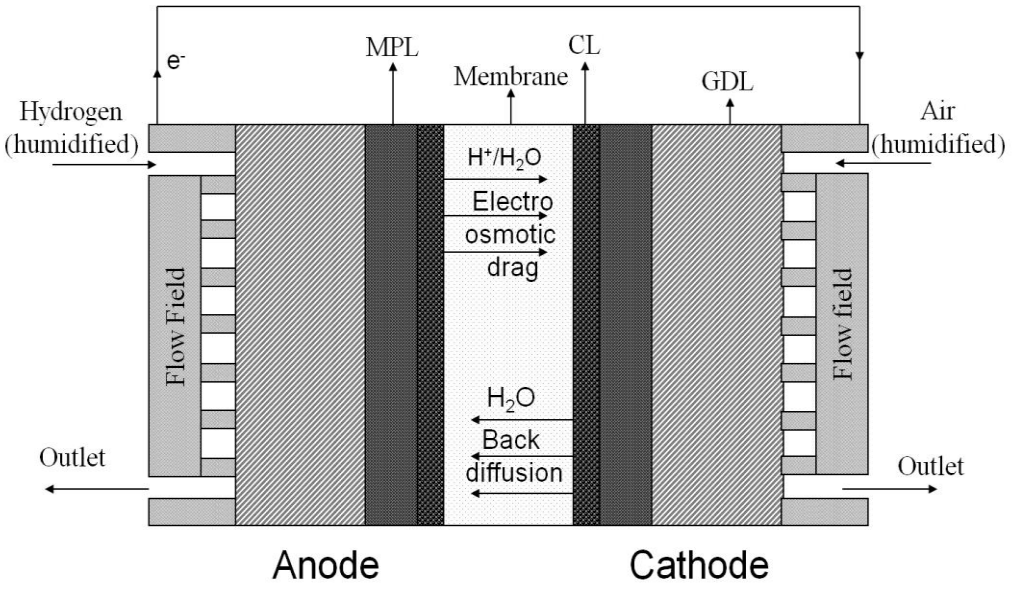

Figure 1.1 Schematic of a PEM fuel cell. MPL: Microporous layer, GDL: Gas diffusion layer, CL: Catalyst layer.

The low operation temperature of PEM fuel cells necessitates a highly active Pt catalyst for the hydrogen oxidation reaction (HOR) at the anode and for the oxygen reduction reaction (ORR) at the cathode. In a PEM fuel cell, the ORR is kinetically much slower than the HOR and determines the entire performance of the cell. Since the electrocatalysts are the main contributors to the PEM fuel cell performance, their cost and durability are the main factors determining the commercialization of the PEM fuel cells. Considering that Pt comprises more than 50 % of the total cost of a PEM fuel cell, non-noble electrocatalysts research is one

of the important priorities in PEM fuel cell research and development although both the activity and the stability of this non-noble catalyst are far from providing enough fuel cell performance compared to Pt. Maintaining the fuel cell performance, the catalyst research is directed to diminishing the amount of Pt used in the electrodes as well. Currently, 0.2 $mgPt \cdot cm^{-2}$ at the anode and 0.4 $mgPt \cdot cm^{-2}$ at the cathode catalyst layer are typically being used by the fuel cell producers [5]. However, even with the most advanced electrodes, effective catalyst utilization is still a major problem. Unsatisfactory gas access to the catalyst layer, inefficient proton access through the membrane, electronic discontinuities and partial flooding problems in the catalyst layer bring the difficulties of the reduction in the amount of Pt catalyst.

1.1.1 PEM fuel cell basics

A PEM fuel cell can be described as a continuous water producer by the redox reactions of oxygen and hydrogen according to the following reactions:

HOR $H_2 \rightarrow 2H^+ + 2e^-$ $E^0 = 0$ V (1.1)

ORR $½O_2 + 2H^+ + 2e^- \rightarrow H_2O$ $E^0 = 1.23$ V (1.2)

The overall electrochemical reaction is given by

$H_2\,(g) + ½O_2\,(g) \rightarrow H_2O\,(l)$ $E^0_{rev} = 1.23$ V (1.3)

The theoretical voltage of the fuel cell, if the enthalpy of formation transformed into electrical energy and the higher heating value of hydrogen (ΔG^0_{HHV}) are used in the calculations (equation 1.4) , is calculated as 1.48 V [6].

$$E^0_{irrev} = -\frac{\Delta G^0_{HHV}}{nF} = -\frac{-286000\ \frac{j}{mol}}{2 \times 96500\ \frac{A.s}{mol}} = 1.48\ V \quad (1.4)$$

Due to the irreversible entropy changes, only the Gibbs free energy portion of the total enthalpy change can be converted into electrical work which is identified as the reversible cell voltage shown in equation 1.3. The difference in the theoretical

voltage and the reversible cell voltage is dissipated as waste heat. Therefore, the maximum theoretical efficiency of a fuel cell is around 83 %. Compared to Carnot engines in which the thermodynamic efficiency increases as temperature increases, the theoretical efficiency of a PEM fuel cell decreases with temperature rise (Equations 1.5 and 1.6).

Carnot engine efficiency: $$\eta_c = \frac{T_{max} - T_{min}}{T_{max}} \quad (1.5)$$

Fuel cell efficiency $$\eta_f = \frac{\Delta G}{\Delta H} = 1 - \frac{T\Delta S}{\Delta H} = \frac{E_{rev}^{\ 0}}{E_{th}} \quad (1.6)$$

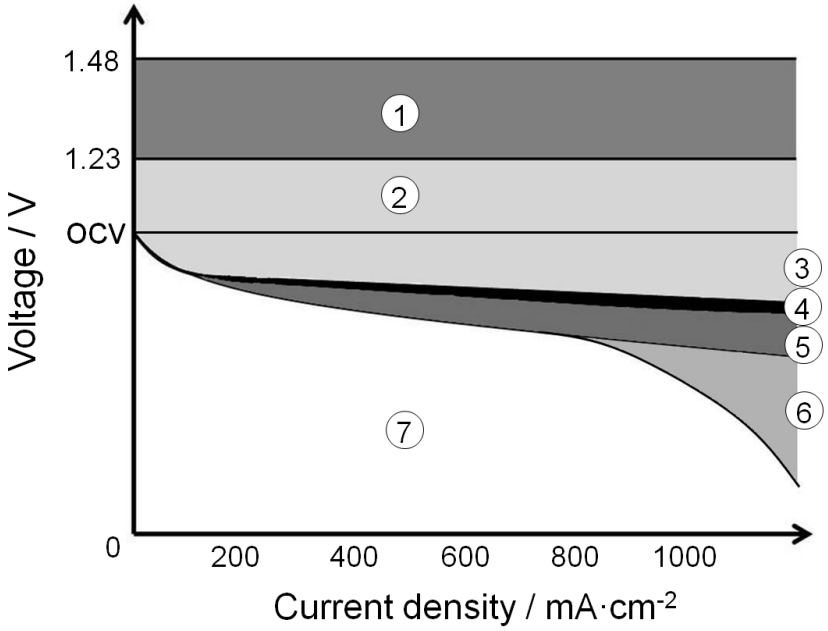

Figure 1.2 Performance characteristics of a PEM fuel cell. (1) Thermodynamic losses, (2) internal currents and fuel crossover (3) cathode overpotential, (4) anode overpotential, (5) Ohmic losses (resistance of polymer electrolyte), (6) concentration polarization (mass transport losses), (7) output power area.

Heat dissipation by the difference in water formation enthalpy and the Gibbs free energy is not the only voltage drop in PEM fuel cells [7]. Figure 1.2 describes the performance characteristics of PEM fuel cells. The reversible cell voltage drops to the open circuit voltage (OCV) because of the small internal current passing through the polymer electrolyte and fuel crossover within the electrolyte (2).

Another voltage loss, called as activation polarization, takes place in the low current density region because of the slowness of the half cell reactions [8]. As seen in Figure 1.2, the cathode overpotential* (3) is always higher than the anode overpotential (4) since the cathode half cell reaction (reduction of oxygen) is much slower than the half cell reaction (hydrogen oxidation) at the anode [9].

The Ohmic losses (5) result from the resistances to the flow of ions in the electrolyte and the electrons through the external current collectors. The corresponding voltage drop is necessarily proportional to the current density. The concentration polarization or the mass transport losses involve the depletion of the reactants at the surface of the Pt catalyst at high current densities. The concentration of the reactants on the surface of the catalyst approaches to zero because the reactants arriving to the catalyst surface immediately react and are consumed. Another loss (6) at high current density is caused by flooding of the catalyst layer because of too much water that is produced at the cathode part of the fuel cell. This thesis is focused more on the concentration polarization losses due to the flooding which brings the necessity of water management in the fuel cell and it will be discussed in the next section.

1.1.2 Water management in PEM fuel cells

Water management has a large influence on the performance and durability of PEM fuel cells [10-12], partly because of the properties of the applied PerFluoroSulfonic Acid type membranes. These membranes have a considerable proton conductivity, but only when their water content is high. Protons cannot move as freely through the membrane when sulfonic acid groups are not dissociated and connected through a continuous water phase [13]. By keeping the membrane in a fully hydrated state, the voltage losses associated with the transport of protons from the anode to the cathode are minimized. Fortunately, water is produced by the ORR at the cathode during fuel cell operation as a linear function of the current density. The electrical current drives the flow of protons from the anode to the cathode and these protons pull water molecules along with them. This

*Overpotential: The potential difference between thermodynamically determined half cell potential and the experimental half cell potential when the reaction takes place.

process, known as “electro-osmotic drag”, can potentially lead to local dehydration of the membrane at the anode (Figure 1.1). A locally ‘dry’ membrane can cause a non-uniform current distribution indirectly causing increased activation polarization losses and it leads to accelerated pinhole formation in the membrane. In contrast, during fuel cell operation, the cathode may suffer from excessive water accumulation due to the electro-osmotic drag. In addition to the product water from the ORR, flooding may occur in the situation where water blocks the pathways of oxidant diffusion to the catalyst layer. However, even under normal operating conditions, a water concentration gradient exists between the anode and the cathode. This gradient drives a process known as “back diffusion” where water is pushed away from the cathode in the direction of the anode. Both “electro-osmotic drag” and “back diffusion” have a large influence on the steady state water distribution across the anode-membrane-cathode, as determined by the MEA design. However, this balance can be significantly influenced by the operating conditions through control over the stoichiometry and humidity of the reactant gas streams [14].

The presence of a Micro-Porous-Layer (MPL) between the catalyst layer and the gas diffusion layer has been demonstrated to improve the fuel cell performance in terms of effective water management in both the anode and the cathode [15, 16]. The typical MPL is fabricated as hydrophobic and is considered as a barrier for water condensation on the gas diffusion layer. Hydrophobic pores less than 1 μm in diameter in the MPL have lower water saturation levels, leading to higher gas transport levels in the catalyst layer [17]. The MPL can be considered as a barrier which increases the “back diffusion”. The MPL exerts a hydrostatic pressure pushing the liquid water towards the anode. Especially at high current densities, the MPL is effective due to the increased amount of water that the cathode has to deal with. The MPL facilitates the water transport by allowing some degree of film formation and functions as a wicking layer for liquid water. In this situation, parallel pathways exist for both oxidant diffusion and water drainage.

The use of carbon nanofibers (CNFs) as MPL on the gas diffusion layer [18, 19] and as a direct catalyst layer for Pt attract attention to integrate the superior properties of CNFs into PEM fuel cells. In the next section, a brief introduction will be given about CNFs.

1.2 Carbon nanofibers

CNFs are one of the most exciting nanomaterials explored in material science. CNFs can be visualized as 1000 times miniaturized human hair. Although the first studies on CNFs were seen at the end of the 19th century [20, 21], the characterization and control at the nanoscale emerged from the invention of transmission electron microscopes (TEM) in the mid of the 20th century. After the first observations of CNFs by Russian scientists Radushkevich and Lukyanovich in 1952 [22], the exploration of their high mechanical strength, electric conductivity, high aspect ratio, and surface area opened the era of tubular carbon structures especially by the discovery of carbon nanotubes (CNTs) by Iijima in 1991 [23].

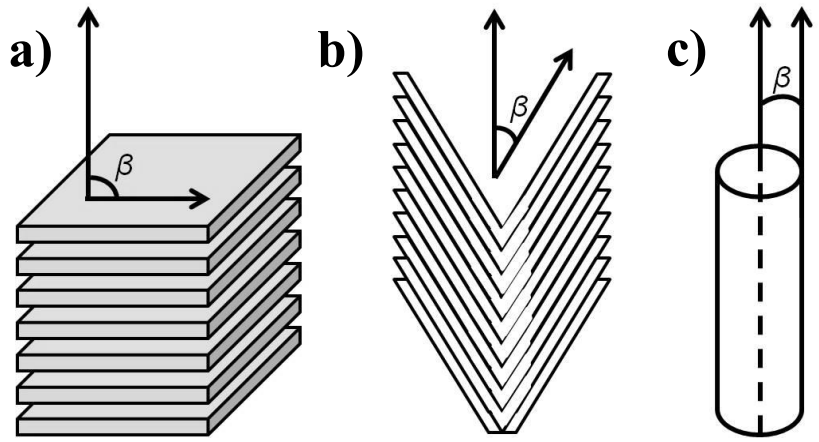

Figure 1.3 Three distinctive forms of carbon nanofibers. a) Platelet: In this form, the growth angle, β, is 90°. b) Herringbone: Here, β is less than 90° c) Tubular: This special form of carbon nanofiber is called as carbon nanotube (β is 0°). β is defined as an angle between the fiber growth axis and the graphene layers.

CNFs are mostly produced via various chemical vapor deposition (CVD) processes, however, laser ablation and arc discharge techniques are also applied [24-27]. In the CVD technique, carbonaceous gases are exposed to the metal particles, usually, cobalt, iron and nickel, at elevated temperatures between 500 and 1200 °C [26]. The carbon containing gas decomposes on the catalyst surface generating carbon which diffuses to the bottom of the metal particle to produce successive graphene sheets, resulting in fibers with a diameter similar to the metal particle. Commonly CNFs are categorized in three groups: platelet, herringbone and tubular (Figure 1.3). Platelet CNFs are composed of graphene sheets inserted on top of each other. The graphene planes can be aligned with respect to the growth axis with an angle by the change of the initial geometry of the metal nanoparticle and they can form herringbone CNFs. When this alignment angle is zero, CNFs are interpreted as CNTs [28]. The type and the thickness of the produced carbon nanofibers depend particularly on the initial size of the metal particle, its geometry and the growth temperature [25].

CNFs are today used as polymer additives [27, 29-32], gas storage materials [33-36], chemical/biological protection materials [37, 38], catalysts supports for many catalytic reactions [25, 39-42] and in many other applications such as nanoprobes, sensors, microelectronics and energy storage [43]. Considerable attention has been devoted to employ CNFs in fuel cells as catalyst support and water management layer [18, 19, 44-57]. Two methods for the incorporation of CNFs in fuel cells were generally applied. In the first method, Pt is deposited on loose fibers and then mixed with polymer and deposited on the gas diffusion layer. Efficiency improvements were claimed by many research groups; however, long term stability of the CNFs was rather poor under the fuel cell operating environment. There is need for a more entangled structure of CNFs on the gas diffusion layer and this need focused the research as a second method toward the direct growth of CNFs on gas diffusion layers.

1.3 Objectives and outline of this thesis

The research on the direct growth of CNFs on carbon paper is focused more on the characterization of the CNF growth. This thesis describes the synthesis of CNFs directly on carbon paper which is used as a gas diffusion material for PEM fuel cells and describes the potential benefits of the CNF grown layer in PEM fuel cell electrodes as a water management and direct catalyst layer (Figure 1.4). The material preparation and characterization of CNF growth on carbon paper are described in the first part of the thesis (chapters 2 and 3) and PEM fuel cell testing is given in the second part (chapters 4, 5 and 6).

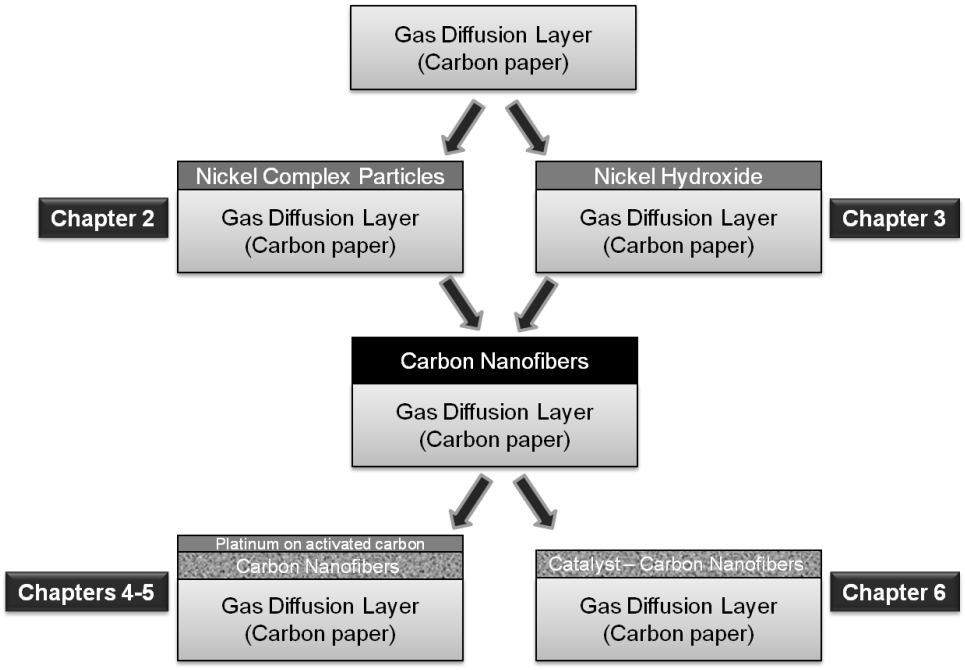

Figure 1.4 Thesis overview.

Chapters 2 and 3 focus on the direct growth of CNFs on carbon paper achieved by using two different catalyst preparation methods. **Chapter 2** is devoted to the catalytic growth of CNFs via nickel complex particles attached on carbon paper. The nickel complex particles were characterized by XRD, XPS, TEM, SEM, and FT-IR spectroscopy techniques. The selective deposition of the particles on one side and throughout the carbon paper was achieved by water and ethanol dispersion

of these particles. Multi-walled CNTs and herringbone CNFs were obtained at the same time for both deposition methods. Although the applied catalyst deposition method is fast, simple, and results in high productivities in terms of mg CNF produced per mg of nickel for both deposition methods, poor reproducibility and the application difficulties in PEM fuel cells forced us to implement a new catalyst deposition method. Since the nickel nanoparticles created a nickel nanoparticle attached carbon paper surface rather than making a network, the CNF growth formed a perfect hairy network on carbon paper fibers however, the gaps larger than 25 μm on carbon paper remain open. That would cause large instabilities in PEM fuel cell operation. **Chapter 3** is focused on the production of completely CNF covered carbon paper via homogeneous deposition precipitation (HDP) of nickel. Nickel hydroxide leaflets were produced relatively with lower CNF productivity with respect to the method described in chapter 2. HDP of nickel has limitations on the molarity of the initial nickel solution and requires a perfect pH control. It is a rather slow process and complete coverage of the carbon paper by $Ni(OH)_2$ takes two to three days. In spite of these difficulties, the CNF grown carbon paper in the applied method is reproducible and more convenient for the PEM fuel cell testing than the CNFs obtained by the nickel nanoparticle deposition on carbon paper.

Chapters 4 to 6 concern with the studies of the PEM fuel cell testing of a CNF grown layer as a water management layer and a direct catalyst layer for Pt catalyst. Special attention was given to the water management. In **Chapter 4**, a reference water management layer on the one side and CNF grown layer on the other side were sandwiched together with a catalyst coated membrane and tested in a PEM fuel cell test station at 65 and 80 °C. The anode and cathode parts of the PEM fuel cell are reversed by switching the gas inlets. The effect of stoichiometric ratio and dry conditions were investigated and the water management properties of the CNF diffusion layer were evaluated. This work directed us into a systematical study on the CNF grown layer which was sandwiched on commercial catalyst coated membranes manufactured by Johnson Matthey. In **Chapter 5,** it is

determined that the CNF grown layer was as good as the reference water management layer. Especially in the high current density region, suitable polymer loading on CNFs improved the hydrophobicity of the CNF grown layer maintaining the acceptable resistance to electron flow. At both operating temperatures, a higher power density was obtained in the high current density region. However, CNF grown carbon paper responds rather slowly to the current withdrawal ramps especially after a current density of 600 $mA \cdot cm^{-2}$. The demand for high current with large ramps results into a fuel starvation since a certain time is needed for the reorganization of the gas diffusion and water removal. Operation of the fuel cell with lower ramps and higher waiting time makes the fuel cell operation more convenient and helpful to attain much better performance than the PEM fuel cells produced by using conventional water management layers. **Chapter 6** presents the PEM fuel cell test results for the Pt deposited CNF layer at the cathode and Pt on active carbon at the anode. The absence of a polymeric coating on the CNF produced a flooding susceptible layer and therefore the performance obtained in these test are much lower with respect to the reference PEM fuel cell constructed by using Pt on active carbon. Even at high stoichiometric ratios the fuel cell performance did not come closer to the performance of the reference PEM fuel cell although the catalyst loadings were similar. This can also be explained by the limitation in effective catalyst utilization of Pt on CNF layer.

Finally in **Chapter 7**, the main conclusions and future perspective of using CNF grown layers in PEM fuel cells are discussed.

References

[1] R.F. Keeling, S.C. Piper, A.F. Bollenbacher, J.S. Walker, Carbon Dioxide Information Analysis Center, Oak Ridge National Laboratory, Oak Ridge, 2009.
[2] P. Brohan, J.J. Kennedy, I. Harris, S.F.B. Tett, P.D. Jones, J Geophys Res, 111 (2006) D12106.
[3] W.R. Grove, The London and Edinburgh Philosophical Magazine and J Science, 14 (1839) 127-130.
[4] C.F. Schoenbein, The London and Edinburgh Philosophical Magazine and J Science, 14 (1839) 43-45.
[5] F. de Bruijn, Green Chem, 7 (2005) 132-150.
[6] J. Xhang, PEM Fuel Cell Electrocatalysts and Catalyst Layers: Fundamentals and Applications, Springer, 2008.
[7] S. Unnikrishnan, PhD thesis, University of Twente, Enschede, 2009, pp. 166.
[8] K. Jayasayee, PhD thesis, Eindhoven University of Technology, Eindhoven, 2011, pp. 183.
[9] H.A. Gasteiger, S.S. Kocha, B. Sompalli, F.T. Wagner, Appl Catal B-Environmental, 56 (2005) 9-35.
[10] S. Litster, C.R. Buie, T. Fabian, J.K. Eaton, J.G. Santiago, J Electrochem Soc, 154 (2007) B1049-B1058.
[11] M.B. Ji, Z.D. Wei, Energies, 2 (2009) 1057-1106.
[12] Y.H. Park, J.A. Caton, Int J Hydrogen Energy, 33 (2008) 7513-7520.
[13] M.A. Hickner, C.H. Fujimoto, C.J. Cornelius, Polymer, 47 (2006) 4238-4244.
[14] T.R. Ralph, D.E. Barnwell, P.J. Bouwman, A.J. Hodgkinson, M.I. Petch, M. Pollington, J Electrochem Soc, 155 (2008) B411-B422.
[15] C.J. Tseng, S.K. Lo, Energy Conversion and Management, 51 (2010) 677-684.
[16] Z.G. Qi, A. Kaufman, J Power Sources, 109 (2002) 38-46.
[17] Z.J. Lu, M.M. Daino, C. Rath, S.G. Kandlikar, Int J Hydrogen Energy, 35 (2010) 4222-4233.
[18] C.Y. Du, B.R. Wang, X.Q. Cheng, J Power Sources, 187 (2009) 505-508.
[19] P.H. Maheshwari, R.B. Mathur, Electrochimica Acta, 54 (2009) 7476-7482.
[20] L.H. Latimer, Patent Number: 252386, in: United States Patent Office, USA, 1882.
[21] T.A. Edison, Patent Number: 299557, in: United States Patent Office, USA, 1889.

[22] L.V. Radushkevich, V.M. Lukyanovich, Zurnal Phizicheskoi Xemei, 26 (1952) 88-95.
[23] S. Iijima, Nature, 354 (1991) 56-58.
[24] A.V. Melechko, V.I. Merkulov, T.E. McKnight, M.A. Guillorn, K.L. Klein, D.H. Lowndes, M.L. Simpson, J Appl Phys, 97 (2005).
[25] K.P. De Jong, J.W. Geus, Catal Rev, 42 (2000) 481-510.
[26] V. Shanov, Y.-H. Yun, M.J. Schulz, J University of Chemical Technology and Metallurgy, 41 (2006) 377.
[27] M.S.P. Shaffer, J.K.W. Sandler, S. Pegel, A.H. Windle, F. Gojny, K. Schulte, M. Cadek, W.J. Blau, J. Lohmar, M. van Es, Nsti Nanotech 2004, Vol 3, Technical Proceedings, (2004) 280-283.
[28] O.M. Dunens, K.J. Mackenzie, C.H. See, A.T. Harris, Nanotechnology Law & Business, 5 (2008) 25-40.
[29] E. Hammel, X. Tang, M. Trampert, T. Schmitt, K. Mauthner, A. Eder, P. Potschke, Carbon, 42 (2004) 1153-1158.
[30] M.C. Paiva, R.M. Novais, R.F. Araujo, K.K. Pederson, M.F. Proenca, C.J.R. Silva, C.M. Costa, S. Lanceros-Mendez, Polymer Composites, 31 (2010) 369-376.
[31] M. Joshi, A. Bhattacharyya, Nsti Nanotech 2004, Vol 3, Technical Proceedings, (2004) 308-311.
[32] J.L. Kang, P. Nash, J.J. Li, C.S. Shi, N.Q. Zhao, Nanotechnology, 20 (2009).
[33] M. Marella, M. Tomaselli, Carbon, 44 (2006) 1404-1413.
[34] C.P. Balde, B.P.C. Hereijgers, J.H. Bitter, K.P. de Jong, Angewandte Chemie-Int Edition, 45 (2006) 3501-3503.
[35] D.J. Browning, M.L. Gerrard, J.B. Lakeman, I.M. Mellor, R.J. Mortimer, M.C. Turpin, Nano Letters, 2 (2002) 201-205.
[36] M. Rzepka, E. Bauer, G. Reichenauer, T. Schliermann, B. Bernhardt, K. Bohmhammel, E. Henneberg, U. Knoll, H.E. Maneck, W. Braue, J Phys Chem B, 109 (2005) 14979-14989.
[37] P.W. Gibson, C. Lee, F. Ko, D. Reneker, J. Engineered Fibers and Fabrics, 2 (2007) 32-40.
[38] L. Qian, J.P. Hinestroza, The Journal of Textile and Apparel Technology and Management, 4 (2004) 1-7.
[39] R. Vieira, Carbon Nanofibers as Macro-structured Catalytic Support in: A. Kumar (Ed.) Nanofibers, InTech, 2010, pp. 13-38.
[40] N.M. Rodriguez, M.S. Kim, R.T.K. Baker, J Phys Chem, 98 (1994) 13108-13111.
[41] P.W.A.M. Wenmakers, J. van der Schaaf, B.F.M. Kuster, J.C. Schouten, J Materials Chem, 18 (2008) 2426-2436.
[42] M.L. Toebes, PhD thesis, Utrecht University, Utrecht, 2004, pp. 175.

[43] M. Endo, M.S. Strano, P.M. Ajayan, Carbon Nanotubes, 111 (2008) 13-61.
[44] C. Wang, M. Waje, X. Wang, J.M. Tang, R.C. Haddon, Y.S. Yan, Nano Letters, 4 (2004) 345-348.
[45] K. Lee, J.J. Zhang, H.J. Wang, D.P. Wilkinson, J Appl Electrochem, 36 (2006) 507-522.
[46] J.S. Zheng, M.X. Wang, X.S. Zhang, Y.X. Wu, P. Li, X.G. Zhou, W.K. Yuan, J Power Sources, 175 (2008) 211-216.
[47] A. Gangeri, G. Centi, A. La Malfa, S. Perathoner, R. Vieira, C. Pham-Huu, M.J. Ledoux, Catalysis Today, 102 (2005) 50-57.
[48] I. Kvande, S.T. Briskeby, M. Tsypkin, M. Ronning, S. Sunde, R. Tunold, D. Chen, Top Catal, 45 (2007) 81-85.
[49] J. Preston, Y. Zou, X. Huang, in: J.S. Douglas (Ed.), MysticMD Inc., 2007, pp. 1-14.
[50] X. Wang, M. Waje, Y.S. Yan, Electrochemical and Solid State Letters, 8 (2005) A42-A44.
[51] J.P. Dodelet, D. Villers, S.H. Sun, A.M. Serventi, S. Desilets, J Phys Chem B, 110 (2006) 25916-25925.
[52] M.M. Waje, X. Wang, W.Z. Li, Y.S. Yan, Nanotechnology, 16 (2005) S395-S400.
[53] P. Ramesh, M.E. Itkis, J.M. Tang, R.C. Haddon, J Phys Chem, 112 (2008) 9089-9094.
[54] W.Z. Li, C.H. Liang, W.J. Zhou, J.S. Qiu, Z.H. Zhou, G.Q. Sun, Q. Xin, J Phys Chem B, 107 (2003) 6292-6299.
[55] F. Yuan, H.K. Yu, H. Ryu, Electrochimica Acta, 50 (2004) 685-691.
[56] T. Bordjiba, M. Mohamedi, L.H. Dao, Nanotechnology, 18 (2007) 1-5.
[57] M. Okada, Y. Konta, N. Nakagawa, J Power Sources, 185 (2008) 711-716.

Carbon nanofiber growth on carbon paper using nickel complex particles

2

Abstract

Nickel complex particles consisting of nickel hydrazine chloride and nickel ammine chloride were used to grow carbon nanofibers (CNFs), either selectively throughout or on only a single side of a carbon paper in thickness of 190 μm for an application in proton exchange membrane fuel cells. Nickel complex particles were prepared by the reduction of nickel chloride with hydrazine and suspended in water to deposit them on a single side of the carbon paper. The same particles suspended in ethanol attached throughout the carbon paper. The reduction of the nickel complex to nickel with hydrogen at 500 °C created nickel nanoparticles on the carbon paper fibers for both deposition methods. The amount of CNFs produced per amount of nickel was higher for single side CNF growth than for the CNF growth throughout the carbon paper. CNF loadings were calculated as 50 wt.% for single side growth (1.0 ± 0.2 wt.% nickel) on the carbon paper and 55 wt.% for the CNF growth (2.0 ± 0.2 wt.% nickel) throughout the carbon paper. Air exposure at room temperature to CNF grown carbon paper formed nickel oxide, which indicated that most of the nickel nanoparticles were not encapsulated by carbon after CNF growth.

2.1 Introduction

Carbon nanofibers (CNFs) have received considerable attention as a catalyst support due to their high electrical conductivity, mechanical strength, open structure and chemical inertness [1]. The growth of CNFs on a large scale was achieved using chemical vapour deposition, in which CNFs are produced by a metal catalyst (nickel, iron or cobalt) heated at temperatures above 400 °C [2-5].

The use of CNFs in proton exchange membrane (PEM) fuel cells was described recently as a means to decrease the amount of platinum (Pt) catalyst used in the cell by increasing the Pt utilization efficiency [6, 7]. It has been reported that when CNF grown carbon paper is used as a self-humidifying electrode, a high power output is obtained in a single cell test of a PEM fuel cell [8]. Most of the research of CNF growth on carbon paper has been directed to the CNF growth throughout the carbon paper, carbon cloth or carbon felt [9-11], however, selective growth of CNFs on a single side of carbon paper has been reported in limited number of studies [12, 13]. The use of CNFs as a catalyst support in PEM fuel cell requires single sided growth since the proton conductivity of the membrane decreases when the Pt is deposited on CNFs grown throughout the carbon paper. The growth of CNFs in the interior parts of the carbon paper decreases the porosity of the carbon paper and may decrease the number of pathways for gas delivery to the catalyst layer and water removal from the catalyst layer. As the gas diffusion medium for PEM fuel cells generally consists of a gas diffusion layer coated with a dense microporous layer on top of it, one should aim such a single sided deposition.

Pham Huu and co-workers investigated the growth of CNFs with incipient wetness impregnation of nickel and reported a productivity of CNFs reaching 50 gram CNFs per gram of nickel catalyst deposited throughout a carbon felt [10]. In this chapter, we present a fast and practical way of growing CNFs throughout and on a single side of carbon paper with a high CNF productivity per amount of nickel catalyst. Nickel complex particles (consisting of a mixture of nickel hydrazine chloride ($Ni(N_2H_4)_2Cl_2$) and nickel ammine chloride ($[Ni(NH_3)_6]Cl_2$)) are suspended in either ethanol or water. These suspensions are used to deposit the

nickel complex particles on a carbon paper support selectively, after which the particles reduced to nickel to achieve proper attachment with the carbon paper fibers. The growth of CNFs with the as-prepared nickel complex particles is extremely efficient for the fast development of CNF-carbon paper decorated structures which can be used as a light weight and high surface area support for PEM fuel cells and for many catalytic reactions [9, 14-17].

2.2 Experimental

2.2.1 Synthesis of the nickel complex particles

Nickel complex particles were synthesized by a reduction reaction of nickel chloride hexahydrate ($NiCl_2 \cdot 6H_2O$) with hydrazine (N_2H_4). Typically, 3.6 g of $NiCl_2 \cdot 6H_2O$ was dissolved in 150 ml deionized water and 9.5 ml of N_2H_4 was added rapidly at 60 °C. The colour of the solution turned immediately into blue and gradually shifted to a blue-violet colour. The reaction solution was stirred one hour and subsequently cooled to room temperature. The precipitate was filtered and washed three times with deionized water and then dried at 80 °C for an hour to obtain the nickel complex particles.

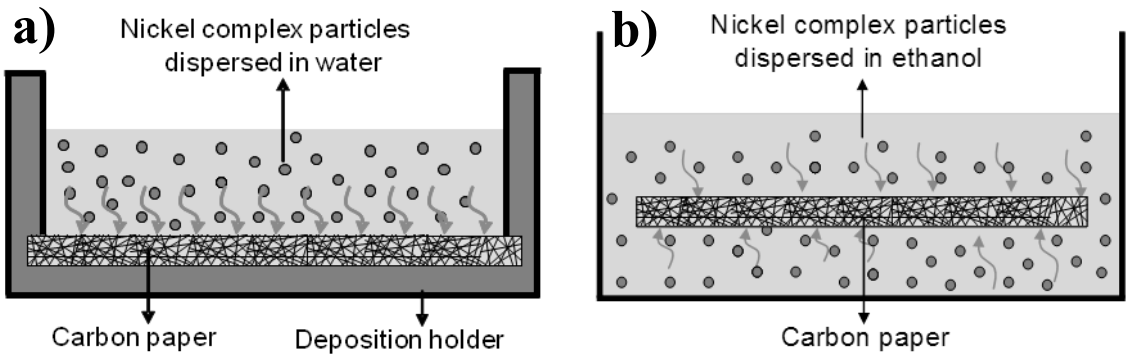

Figure 2.1 Schematic of nickel complex particle attachment on carbon paper using a) water, b) ethanol as a suspension solution.

For the nickel complex particle attachment on a single side of the carbon paper with a thickness of 190 μm and a BET surface area of 0.2 $m^2 \cdot g^{-1}$ (TGP-H-060, Toray), a 40 mm diameter single sided open window holder (Figure 2.1-a) was

used. A nickel complex particle suspension in water of 1 mg·ml^{-1} was prepared and ultrasonicated for 30 minutes to breakup big particles into smaller particles. This suspension was stirred at room temperature with a magnetic stirrer. 5 ml of the suspension was applied on the carbon paper (TGP-H-060, Toray, 4.0 cm in diameter and 106 mg in total) which is placed in a holder. Since the carbon paper surface was hydrophobic, water could not penetrate into the pores of the carbon paper and only the carbon paper fibers available on the top surface of the carbon paper were covered by nickel complex particles. The carbon paper was dried at 80 °C overnight and a nickel loading of 1.0 ± 0.2 wt.% was obtained on a single side of the carbon paper.

Ethanol, compared to water, has a low surface energy and when a droplet of ethanol is put on a carbon paper, it penetrates throughout the carbon paper. Therefore, for nickel complex particle attachment throughout the carbon paper, ethanol was selected as a dispersing solvent and a suspension of nickel complex particles of 5 mg·ml^{-1} in ethanol was prepared. The carbon paper was inserted directly into this suspension (Figure 2.1-b) and shaken for 5 minutes. After the removal of the carbon paper from the suspension, it was dried in an oven at 80 °C for 30 min. A final loading of nickel on the carbon paper of 2.0 ± 0.2 wt.% was calculated from the weight difference.

2.2.2 CNF growth

The carbon paper with the physically attached nickel complex particles was dried at 80 °C and placed in a vertical tubular quartz reactor (5.8 cm inner diameter), for the reduction of the nickel complex particles to nickel before CNF growth. The temperature was increased with 2 °C·min^{-1} to 500 °C in nitrogen (100 ml·min^{-1}) and then 10 vol.% hydrogen was introduced for the reduction keeping the flow rate constant for 2 hours. The temperature was increased to 600 °C and CNFs were grown in the presence of 10 vol.% ethylene and 3.5 vol.% H_2 in N_2 at 100 ml·min^{-1} flow for 4 hours.

2.2.3 Characterization

Transmission electron microscope (TEM) images were recorded with a FEI Tecnai G2 Sphera operated at an accelerating voltage of 200 kV. For TEM analyses, a small amount of CNFs was scratched from the carbon paper and suspended in ethanol. 40 µl of the suspension was put onto a carbon coated copper grid and the grid was dried at ambient temperature. In addition, TEM images were recorded of the as-prepared nickel complex particles. Scanning electron microscopy (SEM) images of the CNFs and the nickel complex particles were taken using a FEI Quanta 3D FEG. The nickel complex particles were deposited on a carbon tape and a 30 nm gold layer was sputtered by a E5100 series II cool sputter coater by Polaron. ImageJ software was used for histogram analyses. The BET surface area and porosity were measured with a Tristar 3000 and Autopore IV 9505 from Micromeritics. Inductively coupled plasma measurements were performed on a Spectra Ciros^{CCD} (ICP-OES). X-ray diffraction analyses were performed by using a Bruker Enduar D4 powder diffractometer using Cu Kα radiation (1.54 Å) at room temperature in 2θ° ranges from $5° < 2\theta° < 90°$ with a $1.2°\cdot min^{-1}$ increments. The data were analyzed by using Diffrac Plus software. FTIR spectra were recorded in KBr on a Bio-Rad Excalibur FTS3000MX infrared spectrometer (four scans per spectrum, resolution: 4 cm^{-1}). X-ray photoelectron spectroscopy (XPS) measurements were conducted with a VG CLAM II hemispherical analyzer equipped with a channeltron detector. The spectrum was recorded using an aluminum anode (Al-$K_{\alpha 1}$ = 1486.6 eV) operating at 150 W under ultrahigh vacuum ($2x10^{-9}$ mbar) at room temperature. Binding energies were calibrated with the Carbon 1s (285.0 eV) as a reference and XPS Casa software; Shirley background correction was used to fit the XPS spectrum.

2.3 Results and discussion

2.3.1 Characterization of the nickel complex particles

Nickel complex particles were characterized by FTIR, XRD, TEM, SEM and XPS. In Figure 2.2, the FTIR spectrum, recorded from 4000 to 500 cm^{-1} (with a

reference dried KBr pellet), indicates the existence of two nickel complexes; bis(hydrazine) nickel(II)chloride ($Ni(N_2H_4)_2Cl_2$) and nickel ammonium chloride ($[Ni(NH_3)_6]Cl_2$). The vibration bands observed at 978 and 1172 cm^{-1} were assigned to (N-N) stretching and NH_2 twisting modes of $Ni(N_2H_4)_2Cl_2$, respectively [18-20]. NH_2 wagging mode vibrations at 1340, 1310 and 1202 cm^{-1} were consistent with the values reported in literature [20]. NH_2 bending modes were assigned at 1605 and 1566 cm^{-1} [20]. Primary N-H stretching mode was characterized by two bands in the region between 3500 and 3250 cm^{-1}. One stretching mode was seen as a broad band around 3500 cm^{-1} and the other N-H stretching mode of $Ni(N_2H_4)_2Cl_2$ and $[Ni(NH_3)_6]Cl_2$ were observed at 3285 with a shoulder band around 3228 cm^{-1} [20]. The vibration bands at 650 and 610 cm^{-1} were attributed to the rocking vibrations of NH_3 ligands in the $[Ni(NH_3)_6]Cl_2$ complex as reported by Park et al. [19].

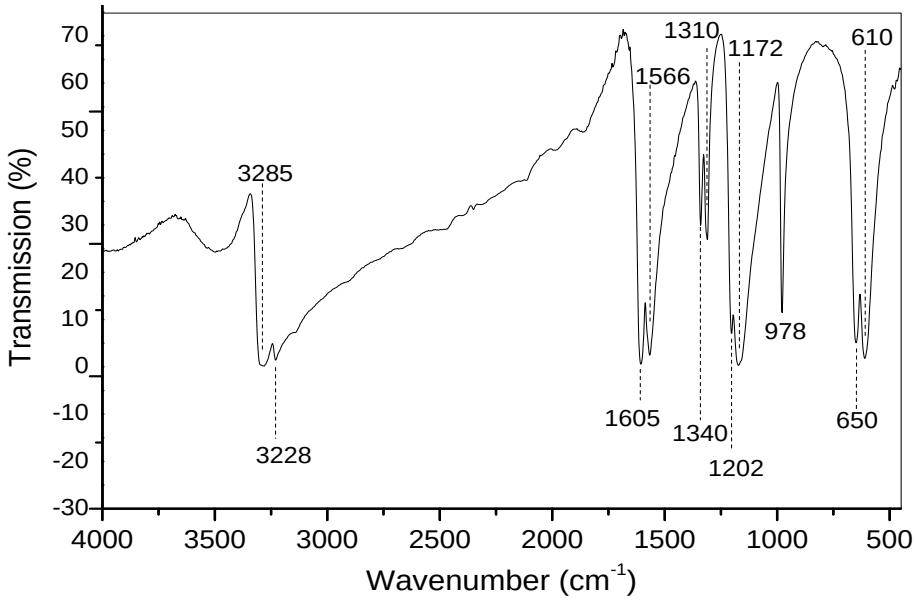

Figure 2.2 FTIR spectrum of nickel complex particles in KBr.

In Figure 2.3, the powder X-ray diagram indicates that the nickel complex particles consist of a mixture of $Ni(N_2H_4)_2Cl_2$ (JCPDS No.20-0098) and $[Ni(NH_3)_6]Cl_2$ (JCPDS No.24-0803). The XRD pattern and the FTIR spectrum together confirmed that tris(hydrazine) nickel(II)chloride ($[Ni(N_2H_4)_3]Cl_2$) was not formed, even though its formation was expected since the hydrazine to nickel ratio

was much higher than the values reported in literature for the production of this complex [19]. This can be explained by the fact that the preparation methods were different. In literature, an aqueous solution of nickel was slowly added to an aqueous solution of N_2H_4 whereas this addition sequence was reversed in the present work. In the powder X-ray diagram (Figure 2.3), a pure nickel phase was not observed. This is in agreement with the XPS spectrum of the nickel complex particles shown in Figure 2.4. Binding energies of nickel complex particles were present both at $2p_{1/2}$ and $2p_{3/2}$ edges at 873.9 and 856.4 eV. The higher binding energy for $2p_{3/2}$ edge compared to Ni^0 (852.9eV) as well as high binding energy satellites confirmed the existence of nickel ions with a divalent state in the nickel complex particles [21].

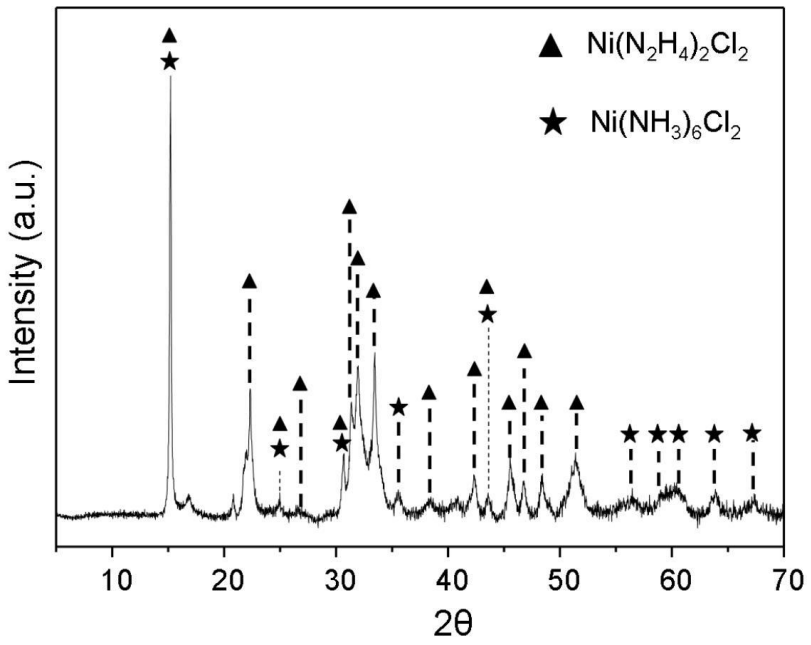

Figure 2.3 Powder X-ray diagram of nickel complex particles.

The nickel complex particles were analyzed by ICP to determine the nickel content. ICP analysis showed that the nickel complex particles contained 31 ± 1 wt.% of nickel. This value corresponds to the atomic mass percentage of nickel (30.3 %) in $Ni(N_2H_4)_2Cl_2$. In TEM analyses, the interplanar distance of the crystalline structure of the nickel complex particles (Figure 2.5-b) was found as 0.59 ± 0.01 nm. This value is in agreement with a study performed on the

crystalline structure of nickel complex nanotubes. The interplanar distance of these nanotubes was found as 0.584 nm and it was assigned to $[Ni(NH_3)_6]Cl_2$ [22]. The interplanar distance of nickel hydrazine chloride was not reported to our knowledge before, however the crystalline structure of zinc hydrazine chloride ($Zn(N_2H_4)_2Cl_2$) was reported as isotypic to $Ni(N_2H_4)_2Cl_2$ [18]. It can be expected that the interplanar distances of $Zn(N_2H_4)_2Cl_2$ (0.58453 nm, JCPDS no.72-0502) and $Ni(N_2H_4)_2Cl_2$ are similar to each other and thereby, the interplanar distance given in TEM analyses (Figure 2.5-b) can be attributed to both $Ni(N_2H_4)_2Cl_2$ and $[Ni(NH_3)_6]Cl_2$. Considering the mass percentage of nickel in $[Ni(NH_3)_6]Cl_2$ (25.3 %), results of ICP for the nickel content in nickel complex particles reveals that the major component in this mixture is $Ni(N_2H_4)_2Cl_2$.

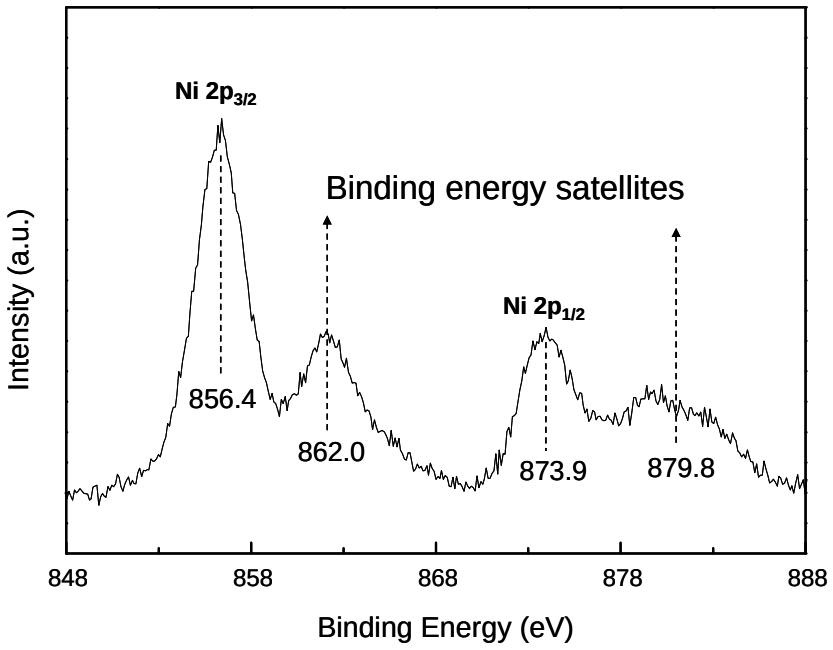

Figure 2.4 XPS of nickel complex particles.

From TEM analyses it was concluded that the as-prepared nickel complex particles have a very broad particle size distribution between 10 and 200 nm (Figure 2.5-a). In Figure 2.5-c, a SEM image of nickel complex particles is shown. It can be seen that the nano-size particles are agglomerated to 50 μm spherical particles. Particles below 1 μm in diameter were also observed, indicating a very broad size distribution (Figure 2.5-d). These results reveal particle agglomeration

and necessitate the ultrasonication of the suspension just before the deposition on the carbon paper fibers.

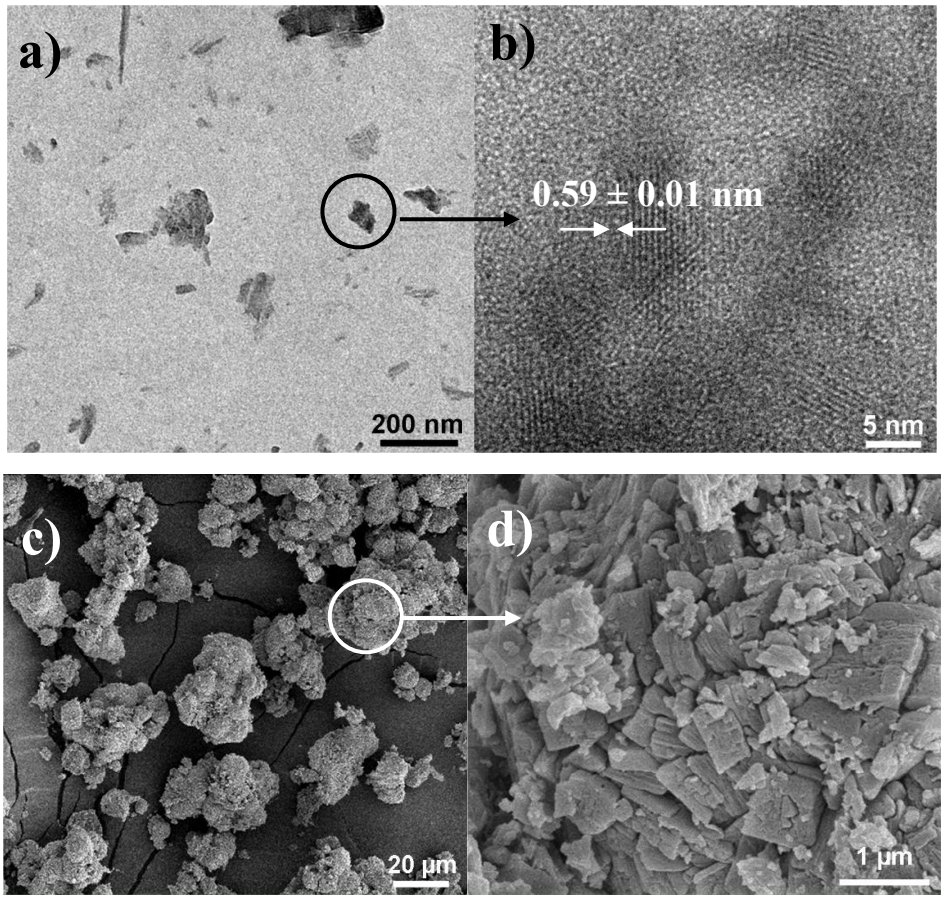

Figure 2.5 TEM (a,b) and SEM (c,d) characterization of nickel complex particles.
a) General overview of the particles after washing, drying and ultrasonication steps. b) High resolution TEM image of a nickel complex particle showing the interplanar distance. c) A SEM image of nickel complex particles after the drying step. d) Magnified view of the particles shown in image c.

2.3.2 Selective deposition of the nickel complex particles

The selective deposition of nickel complex particles on a single side of a carbon paper was achieved by utilizing the hydrophobic property of the carbon paper. Since the contact angle of water with the surface of the carbon paper is high (~130°), water penetration into the pores of the carbon paper is limited [23]. The penetration depth of the nickel complex particles depends on the water contact with the carbon paper fibers. Considering the thickness of the carbon paper fibers, which

is around 7 μm, the nickel complex particles can be found only in a limited depth from the top surface of the carbon paper (Figure 2.6-a).

Nickel complex particles can be attached throughout the carbon paper by using ethanol. Although the ethanol-nickel complex particle suspension was ultrasonicated just before the dipping of the carbon paper, agglomerated particles (20-25 μm) were observed on the carbon paper after reduction with hydrogen (Figure 2.6-b). This size of the particles was also observed in the SEM images of the nickel complex particles indicating a lack of particle breakup to smaller particles during ultrasonication. The size of the nickel complex particles is crucial for the efficient production of CNFs since large nickel complex particles do not contribute to the CNF growth around the carbon paper fibers. The attachment of the nickel complex particles around the carbon paper fibers was achieved by Van der Waals attraction since washing of the carbon paper with ethanol can easily detach the nickel complex particles. A stronger bond between nickel and carbon was formed after the decomposition of the nickel complex upon heating and reduction of nickel since washing or even ultrasonication could not detach the reduced nickel nanoparticles.

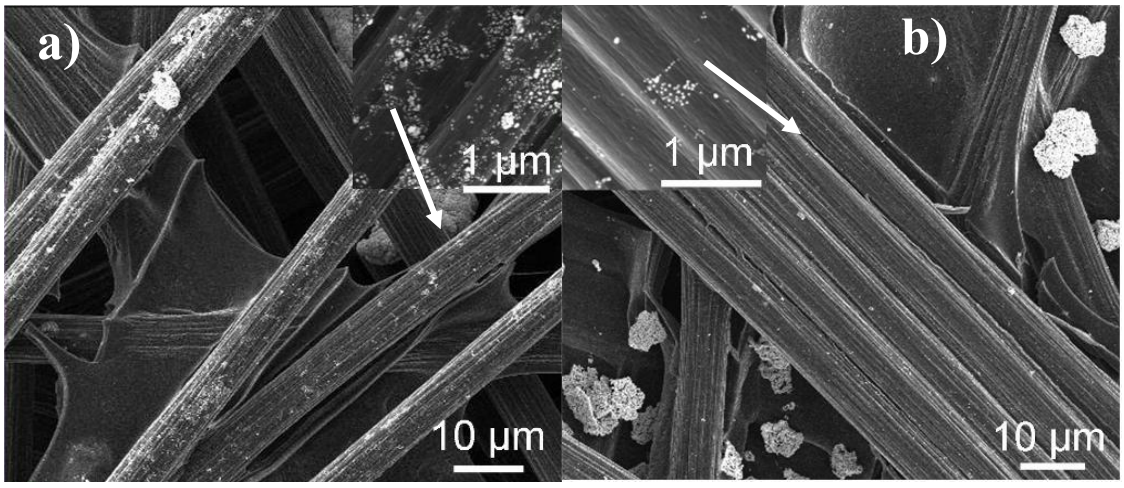

Figure 2.6 SEM images of the nickel nanoparticles on carbon paper after reduction in hydrogen at 500 °C; a) single side deposition of nickel complex particles, and b) deposition of nickel complex particles throughout the carbon paper by using ethanol.

2.3.3 CNF growth

CNF growth on a single side of the carbon paper

Nickel complex particles attached on a single side of the carbon paper were reduced to nickel prior to CNF growth and homogeneously dispersed nickel nanoparticles were obtained. CNFs were grown on the carbon paper fibers by subjecting these nanoparticles to ethylene at 600 °C in the presence of hydrogen and nitrogen. Carbon paper fibers below the upper layer of the carbon paper, seen in the opened pore (big circle in Figure 2.7-a), did not contain any CNFs. This is explained by the absence of Ni particles below the top layer of carbon paper fibers as there was no water penetration. This method favors the CNF growth on a restricted region from the top layer of the carbon paper. A final loading of 50 ± 5 wt.% of CNFs on carbon paper was obtained. The growth productivity of the nickel nanoparticles was calculated as 105 ± 10 $gCNF \cdot g^{-1}$ Ni (Table 2.1).

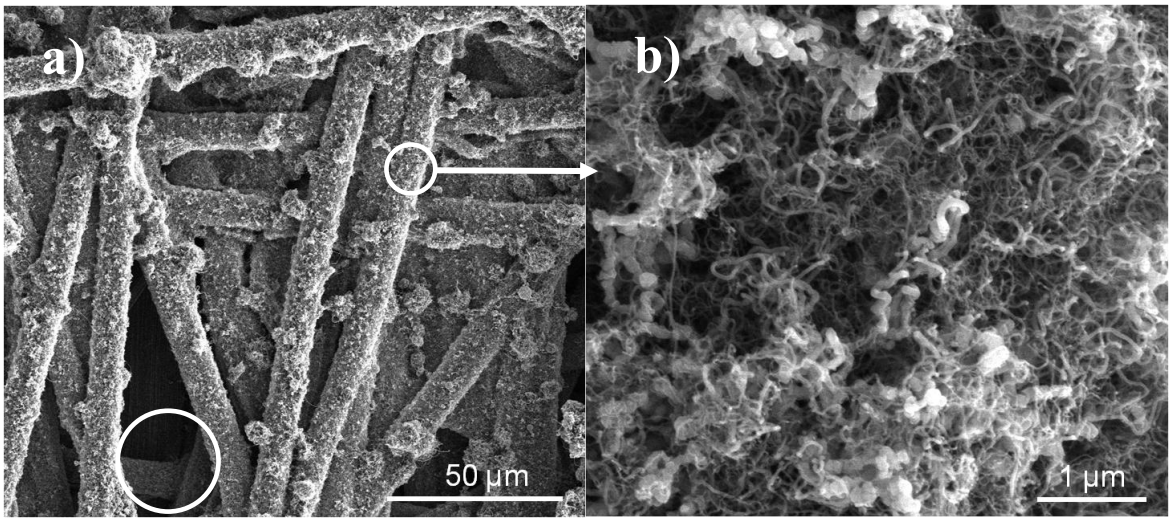

Figure 2.7 CNF growth on carbon paper by the nickel complex particles suspended in water. SEM images of; a) single side CNF growth on carbon paper, and b) magnified CNF layer.

Table 2.1 Properties of the CNF grown carbon paper.

	CNF grown carbon paper		
	Throughout the carbon paper	Single side of the carbon paper	Carbon paper
Nickel loading on carbon paper (wt.%)	2.0 ± 0.2	1.0 ± 0.2	-
CNF loading on carbon paper (wt.%)	55 ± 5	50 ± 5	-
Productivity of nickel (g CNF·g^{-1}Ni)	77 ± 10	105 ± 10	-
CNF-carbon paper BET ($m^2 \cdot g^{-1}$)	80 ± 5	60 ± 5	-
CNF-BET (calculated) ($m^2 \cdot g^{-1}$)	126 ± 5	121 ± 5	0.2 [12]
CNF-carbon paper porosity, %	60 ± 5	65 ± 5	78 [12]

The tabulated results are the averages of three different experiments.

CNF growth throughout the carbon paper

To grow CNFs in the interior parts of the carbon paper, ethanol was used for the complete dispersion of the nickel complex particles. Some of the nickel complex particle aggregates (10-20 μm) did not break up into smaller particles, like in the case of the water suspension (Figure 2.6). These nickel aggregates did not contribute to the CNF growth around the carbon paper fibers (big circle in Figure 2.8-a). Even though the utilization of the nickel nanoparticles decreased, the carbon paper fibers were still completely covered by CNFs (small circle in Figure 2.8-a, and Figure 2.8-b). The uniform thickness of the CNFs showed that the reduction of the nickel complex particles was successful and the attachment of the reduced nickel on the carbon paper was homogeneous. A final loading of 55 ± 5 wt.% CNFs was obtained for a nickel loading of 2.0 ± 0.2 wt.%. The growth productivity was calculated as 77 ± 10 gCNF·g^{-1} Ni (Table 2.1). The productivity was lower in comparison with the single side growth of CNFs on carbon paper since the amount of nickel contributing to CNF growth decreased due to the lack of large nickel complex particle breakup. Less than 5 wt.% loss of CNFs was observed after

ultrasonication for 10 minutes due to the detachment of the loose fibers. The BET areas of the CNFs were calculated as 126 ± 5 $m^2 \cdot g^{-1}$ for the CNF growth throughout and 121 ± 5 $m^2 \cdot g^{-1}$ for the CNF growth on a single side of the carbon paper. In conclusion, the BET area did not show any significant difference with respect to the nickel deposition method. The CNF growth on the carbon paper decreased the porosity to 60 ± 5 % for the CNF throughout the carbon paper and to 65 ± 5 % for the CNF growth on a single side of carbon paper.

CNF growth throughout the carbon paper increased the thickness of the carbon paper fibers by 2 μm on average with respect to bare carbon paper fibers whereas the same increase was 4 μm on a single side CNF growth on carbon paper (Figure 2.9-a,b). This increase in the shell thickness of CNFs in single side growth is due to the increased density of the nickel complex particles on the single side of the carbon paper compared to the nickel complex particles distributed throughout the carbon paper. Small deviations in the shell thickness of the CNFs around the carbon paper fibers (Figure 2.9-b) indicate a narrow distribution of the nickel nanoparticles since the CNF network density can be assumed to be proportional to the amount of nickel seeds attached on the carbon paper fibers.

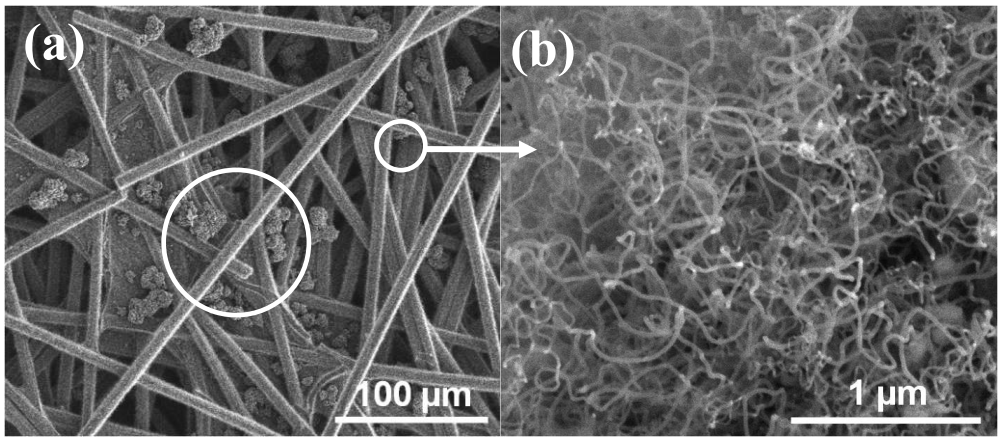

Figure 2.8 a) SEM image of CNFs grown throughout the carbon paper. Big nickel agglomerates are shown in the big circle. b) Magnified CNFs in the same picture shown in (a) as small circle.

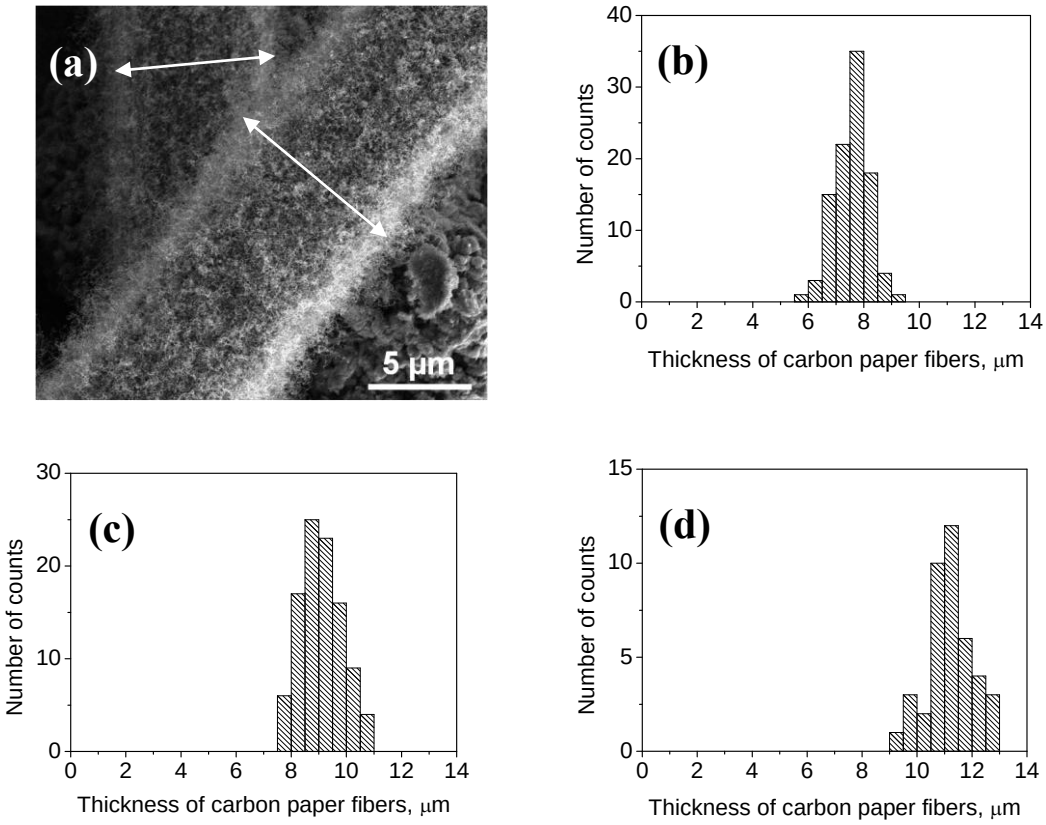

Figure 2.9 a) SEM image of CNF grown carbon paper fibers. The arrows represent the thickness of the carbon paper fibers. Thickness histogram of; b) bare carbon paper fibers, c) carbon paper fibers with CNFs grown throughout the carbon paper, d) carbon paper fibers with CNFs grown on a single side of the carbon paper.

Figure 2.10 shows the morphology of the carbon structures obtained for both catalyst deposition methods. Multi-walled carbon nanotubes (MWCNTs) are observed ranging from 5 to 30 nm thickness and CNFs are seen in the range in between 40 and 60 nm. This indicates that the nanoparticles formed after the reduction of the nickel complex particles split into smaller active nickel nanocrystals giving rise to the formation of the MWCNTs (Figure 2.10-a). The number of graphene planes in most of the MWCNTs (Figure 2.10-c) varies in between 50 and 60, and the interplanar distance between two graphene planes was determined as 0.340 ± 0.005 nm [12, 13, 24, 25]. However, a considerable amount of CNFs is also observed throughout and on only a single side of the carbon paper (Figure 2.10-b). The graphene planes were not continuous but inclined with an

angle of 28° from the growth axis (Figure 2.10-d). The thickness of these CNFs is mostly around 50 nm. For the sake of simplicity, throughout the text, all the grown carbon structures were called as CNFs.

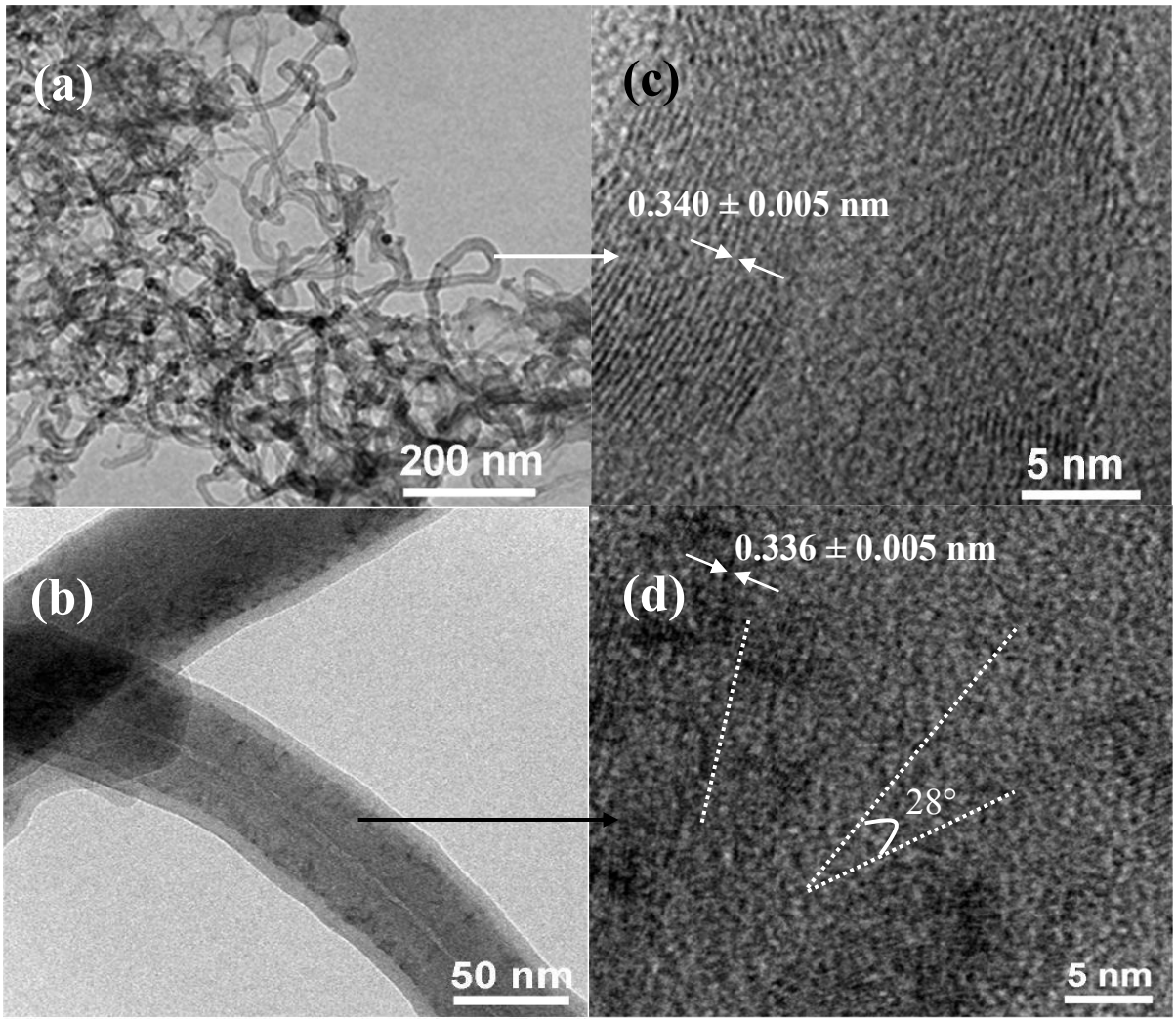

Figure 2.10 TEM images of a) MWCNTs and b) CNFs. High resolution TEM image of c) MWCNT, and d) CNF.

Powder X-ray diagrams of CNFs and carbon paper are shown as plots (a) and (b) in Figure 2.11. The CNF grown carbon paper was taken out from the reactor (which was completely at an oxygen free environment at the reaction condition) at room temperature and an air exposure took place creating nickel oxides. This indicates that most of the nickel nanocrystals were not encapsulated by carbon during the CNF growth and nickel layers were passivated by air exposure at room temperature during the removal of the sample from the reactor.

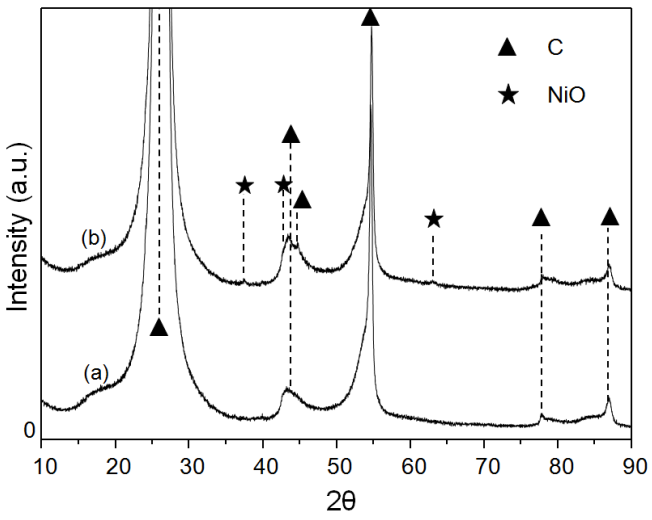

Figure 2.11 Powder X-ray diagrams of (a) carbon paper, (b) CNF grown carbon paper (the same X-ray diagram obtained for both nickel deposition methods).

2.4 Concluding remarks

CNFs and MWCNTs were grown throughout and on a single side of a carbon paper by the selection of a suitable dispersing solvent for the attachment of nickel complex particles. Nickel complex particles composed of $Ni(N_2H_4)_2Cl_2$ and $[Ni(NH_3)_6]Cl_2$ were used for nickel catalyst deposition on the carbon paper fibers. ICP measurements showed that the amount of nickel in the nickel complex particles was close to the mass percentage of nickel in $Ni(N_2H_4)_2Cl_2$. The reduction of the nickel complex particles with hydrogen formed nickel nanoparticles firmly attached on the carbon paper fibers. Herringbone CNFs in thickness between 40 and 60 nm and MWCNTs in thickness between 5 and 30 nm were homogeneously grown on the carbon paper. The productivity of nickel during CNF growth depends on the large particle breakup during the preparation of the nickel complex particle suspensions. The method described in this work can be used to produce large surface area carbon mixtures as an alternative water management layer and direct catalyst layer at the cathode part of PEM fuel cells and can be used in gas phase catalytic reactions by deposition of a suitable catalyst on the CNFs.

References

[1] K.P. De Jong, J.W. Geus, Catal Rev, 42 (2000) 481-510.
[2] V. Shanov, Y. Yun, M. J. Schulz, J University of Chemical Technology and Metallurgy, 41 (2006) 377.
[3] Y. Yamada, Y. Hosono, N. Murakoshi, N. Higashi, H. Ichi-oka, T. Miyake, N. Ikenaga, T. Suzuki, Diamond and Related Mater, 15 (2006) 1080-1084.
[4] K. Takehira, T. Ohi, T. Shishido, T. Kawabata, K. Takaki, Appl Catal A-Gen, 283 (2005) 137-145.
[5] M.L. Toebes, J.H. Bitter, A.J. van Dillen, K.P. de Jong, Catal Today, 76 (2002) 33-42.
[6] A. Caillard, C. Charles, R. Boswell, P. Brault, Nanotechnology, 18 (2007) 1-9.
[7] K. Lee, J.J. Zhang, H.J. Wang, D.P. Wilkinson, J Appl Electrochem., 36 (2006) 507-522.
[8] C.Y. Du, B.R. Wang, X.Q. Cheng, J Power Sources, 187 (2009) 505-508.
[9] S. Perathoner, M. Gangeri, P. Lanzafame, G. Centi, Kinet Catal, 48 (2007) 877-883.
[10] B. Louis, R. Vieira, A. Carvalho, J. Amadou, M.J. Ledoux, C. Pham-Huu, Top Catal, 45 (2007) 75-80.
[11] Z.Y. Shi, X.Z. Wang, Z.M. Ding, Appl Surf Sci, 140 (1999) 106-110.
[12] S. Celebi, T.A. Nijhuis, J. van der Schaaf, F.A. de Bruijn, J.C. Schouten, Carbon, 49 (2010) 501-507.
[13] T. Bordjiba, M. Mohamedi, L.H. Dao, Nanotechnology, 18 (2007) 1-5.
[14] W. Zhu, D. Ku, J.P. Zheng, Z. Liang, B. Wang, C. Zhang, S. Walsh, G. Au, E.J. Plichta, Electrochimica Acta, 55 (2010) 2555-2560.
[15] Y. Motoyama, S.H. Yoon, H. Nagashima, J Synthetic Organic Chemi Japan, 67 (2009) 724-734.
[16] M.J. Ledoux, C. Pham-Huu, Catal Today, 102 (2005) 2-14.
[17] C.D. Taboada, J. Batista, A. Pintar, J. Levec, Appl Catal B-Environmental, 89 (2009) 375-382.
[18] R. Tsuchiya, M. Yonemura, A. Uehara, E. Kyuno, Bulletin of the Chemical Soc of Japan, 47 (1974) 660-664.
[19] J.W. Park, E.H. Chae, S.H. Kim, J.H. Lee, J.W. Kim, S.M. Yoon, J.Y. Choi, Mater Chem and Phys, 97 (2006) 371-378.
[20] D. Nicholls, R. Swindell, J Inorganic & Nuclear Chem, 30 (1968) 2211.
[21] K.S. Kim, N. Winograd, Surface Science, 43 (1974) 625-643.
[22] L. Guo, C.M. Liu, R.M. Wang, H.B. Xu, Z.Y. Wu, S. Yang, J Am Chem Soc, 126 (2004) 4530-4531.
[23] S. Bliznakov, Y. Liu, N. Dimitrov, J. Garnica, R. Sedev, Langmuir, 25 (2009) 4760-4766.

[24] B. Louis, G. Gulino, R. Vieira, J. Amadou, T. Dintzer, S. Galvagno, G. Centi, M.J. Ledoux, C. Pham-Huu, Catal Today, 102-103 (2005) 23-28.

[25] S. Sun, D. Yang, G. Zhang, E. Sacher, J.P. Dodelet, Chem Mater, 19 (2007) 6376-6378.

Carbon nanofiber growth on carbon paper for PEM fuel cells

3

This chapter has been adapted from:

Celebi, S., Nijhuis, T.A., Schaaf, J. van der, Bruijn, F.A. de & Schouten, J.C., 2011. Carbon nanofiber growth on carbon paper for proton exchange membrane fuel cells. *Carbon*, 49(2), 501-507.

Abstract

Homogeneous deposition precipitation (HDP) of nickel has been investigated for the growth of carbon nanofibers (CNFs) on carbon paper for use in proton exchange membrane fuel cells as a gas diffusion layer. Selective CNF growth on only one side of carbon paper is required to transfer the generated protons on platinum catalyst fast enough to avoid any proton mass transfer losses. For this purpose, a mask deposition holder was designed to deposit the nickel hydroxide which is reduced to nickel with hydrogen before catalyzing the CNF growth. The deposition time effect on the catalyst loading and the effect of the catalyst loading variation on the yield of CNF growth on carbon paper were investigated. Both effects had linear dependence in the region of interest. The HDP of nickel on the carbon paper ensured strong attachment of nickel crystals on the carbon paper fibers keeping the porosity at a promising level with an acceptable BET area of CNFs. The HDP method provides fine-tuning in the CNF layer thickness only on one side of the carbon paper with good reproducibility in the deposition of nickel.

3.1 Introduction

Hydrogen fuelled proton exchange membrane (PEM) fuel cells have been attracting great attention for their potential transport and stationary applications as a clean power generation system that produces water as exhaust [1-3]. Before large scale commercialization of PEM fuel cells takes off, the cost of PEM fuel cells presents still a major challenge for most applications among others because of the requirements of high-cost noble metals. Ineffective catalyst utilization, high voltage loss due to oxygen transport limitations, and long term corrosion of carbon in both the catalyst supports as well as the gas diffusion media (GDM) currently used in PEM fuel cells necessitate the development of more effective cell components.

In most PEM fuel cell electrodes, Pt is deposited on a high surface area carbon support, such as Vulcan XC 72 or Black Pearls, yielding small Pt particles ranging 2-4 nm in diameter at loadings as high as 20 – 40 wt % (Figure 3.1-a). An ink solution containing the catalyst support with Nafion dispersed in a suitable solvent is deposited either on the membrane or on the GDM which plays a crucial role in the water management of the PEM fuel cell, both under dry and wet conditions. Under dry conditions, the GDM can help retaining the water in the membrane electrode assembly whereas under wet conditions the GDM does not need to drain the water. A better understanding of the GDM properties and the fuel cell performance is still needed in the further optimization of the PEM fuel cell. The long term stability of GDM is a matter of concern as well. In many long term fuel cell tests, a decrease in water removal capacity leads to a gradual decrease of the PEM fuel cell performance [1]. The corrosion of the GDM could be one of the causes of this performance loss. The use of more graphitic and highly oriented carbon such as an alternative material for use in the GDM combines high electronic conductivity with an acceptable surface area [4]. These properties can yield a GDM with enhanced stability and tunable water properties.

Previously, carbon nanofibers (CNFs) were used instead of amorphous high surface area carbons in the development of PEM fuel cells and the integration scheme using the Nafion-Ink method remained the same as that applied in currently

used carbon supports [5-7]. These structures did not demonstrate improved catalyst utilization in the long term. The detachment of the CNFs from the electrode surface led to the catalyst being incompletely used. The direct growth of CNFs on the carbon paper introduces a stronger binding with the carbon paper fibers and the CNF detachment can be avoided (Figure 3.1-b) [8-10]. In addition, a better control of the gas diffusion layer structure can be gained by growing the CNFs directly on the carbon paper. In some previously reported studies, CNF growth took place throughout the carbon paper [8, 10, 11]. In a wet chemical Pt deposition on CNFs, this results into a Pt deposition throughout the carbon paper, increasing the electronic path and reducing the rate of proton access and thus the Pt utilization [12].

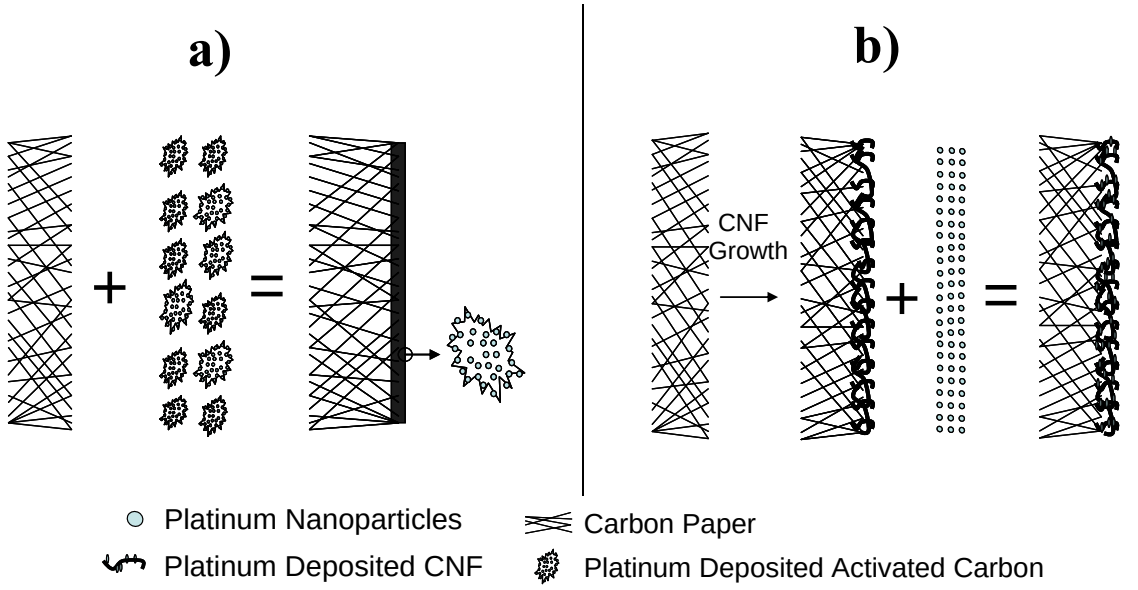

Figure 3.1 a) Integration scheme of platinum deposited activated carbon on carbon paper; b) Direct growth of CNFs on carbon paper and subsequent platinum deposition.

Recently, selective CNF growth on one side of the carbon paper has been demonstrated using electrodeposition of nickel or cobalt catalysts [13]. This chapter presents a more attractive alternative by the deposition of nickel hydroxide ($Ni(OH)_2$) using homogeneous deposition precipitation (HDP) of nickel and subsequent CNF growth on one side of the carbon paper with the purpose to gain control over the GDM. HDP of nickel is a very convenient method which forms a dense and controllable $Ni(OH)_2$ layer on the carbon paper.

3.2 Experimental

3.2.1 Homogeneous deposition precipitation of nickel on carbon paper

The HDP of nickel on carbon paper (TGP-H-060, Toray Industries, Figure 3.2-a,b) was performed with a mask deposition holder (Figure 3.2-c). The holder was placed vertically (carbon paper surface is looking upward) into a deposition chamber containing a nickel salt solution ($Ni(NO_3)_2 \bullet 6H_2O$) of 4.0 mM in 300 ml DI water. The pH of the solution was adjusted to 2.4 using 0.5 M nitric acid at 90 °C. Then, 50 ml 60 mM urea solution was added. The molar ratio of urea to nickel was 2.5 in the final solution. The urea decomposes slowly to ammonium hydroxide and carbon dioxide at this temperature and thereby increases the pH of the solution. The pH increase causes the formation of $Ni(OH)_2$ crystallites. During the $Ni(OH)_2$ precipitation, the pH remains constant. The rate of urea decomposition determines the rate of OH^- formation and thus the precipitation of $Ni(OH)_2$ layers.

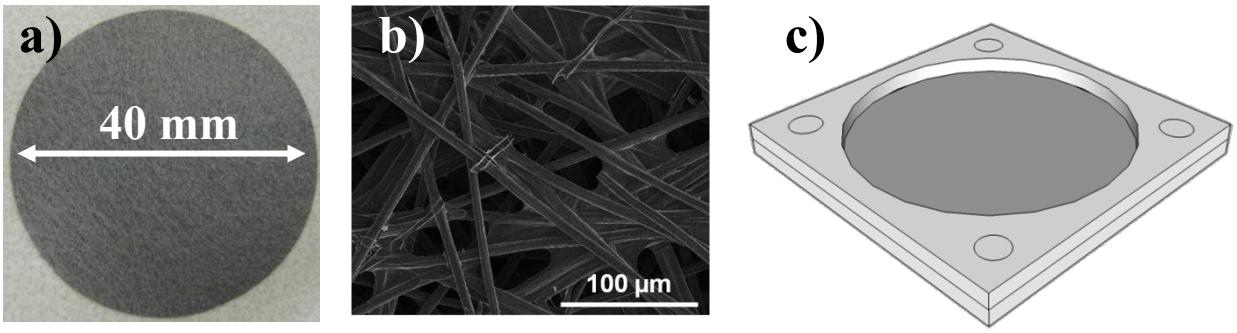

Figure 3.2 a) Picture of the carbon paper. b) SEM image of the carbon paper. c) 40 mm window opened carbon paper holder.

The color of the $Ni(OH)_2$ coated side of the carbon paper was greenish blue after drying at 80 °C for 2 hours. The back side of the carbon paper was the same black color as before the deposition of $Ni(OH)_2$. The $Ni(OH)_2$ deposited carbon paper was ultrasonicated in ethanol for 15 mins to test the binding strength of $Ni(OH)_2$ layers on the carbon paper. No $Ni(OH)_2$ mass loss was observed after the ultrasonication. It is important to note that although an acid pretreatment of the carbon support is often used, when HDP is used to deposit a metal, to increase the

number of anchoring sites on carbon surfaces, this method was not used here. The hydrophobicity of the carbon paper should be high in order to have the $Ni(OH)_2$ crystallization occur only on the open window face of the carbon paper as this prevents the penetration of water into the carbon paper. In experiments with oxidized carbon papers, $Ni(OH)_2$ layers were formed not only on the surface but also inside the carbon paper. The acid treatment was therefore not used here.

3.2.2 CNF growth

$Ni(OH)_2$ deposited carbon paper was placed in a vertical tubular reactor (5.8 cm inner diameter) for the complete reduction of $Ni(OH)_2$ to nickel for CNF growth. The reduction was performed at 500 °C in a hydrogen (H_2, vol. 10% in nitrogen (N_2)) stream with a total flow of 100 ml·min^{-1} for 4 hours. Subsequently, the temperature was increased with 2 °C/min to 600 °C in the presence of 100 ml/min (vol. 100 %) N_2 and then the CNF growth was initiated by introducing vol. 10 % ethylene (C_2H_4), vol. 3.5 % H_2 and balanced N_2 in a total flow of 100 ml·min^{-1} and continued for 4 hours. The use of H_2 during the growth of CNFs extends the encapsulation time of the active nickel nanocrystals by carbon [14].

3.2.3 Characterization

Transmission electron microscope (TEM) images were recorded with a FEI Tecnai G2 Sphera transmission electron microscope at an acceleration voltage of 200 kV. For TEM analysis, a small amount of CNFs was scratched from the carbon paper surface and suspended in ethanol. 30 µl of the suspension was put on a carbon coated copper grid and the grid was dried at ambient temperature. Scanning electron microscopy (SEM) images of the carbon paper were taken using a FEI Quanta 3D FEG. The BET surface area and porosity were measured with a Tristar 3000 and Autopore IV 9505 from Micromeritics. Carbon papers were cut into small pieces with a sharp knife and put into the measurement tube without grinding. Inductively coupled plasma (ICP) measurements were performed using a Spectra Ciros^{CCD} (ICP-OES). X-ray diffraction analysis was performed by using a Riqaku powder diffractometer with Cu Kα radiation (1.54 Å). Data collection was done in

the range of $15° < 2\theta < 80°$ with $1.2°\cdot min^{-1}$ increments. The data were analyzed by using Jade software.

3.3 Results and discussion

3.3.1 Homogeneous deposition precipitation of nickel on carbon paper

The kinetics of HDP of nickel was previously studied on silica and CNF powders [15]. It was shown that the carboxylic acid groups were mainly responsible for the nucleation of $Ni(OH)_2$ on the CNFs. Both CNFs and carbon paper fibers have the same carboxylic acid groups on their surface and it can be expected that the same $Ni(OH)_2$ deposition mechanism is valid for the carbon paper fibers.

In the HDP of nickel, $Ni(OH)_2$ is deposited on the carbon paper only where water contacts with its surface. Since the CNFs grow where $Ni(OH)_2$ is attached, the CNF growth inside the carbon paper depends on the accessibility of water molecules in the interior parts of the carbon paper. The wettability of the carbon paper affects directly this accessibility inside the porous paper substrate. The difference between the advancing and receding contact angles of the carbon paper is very large. Therefore, the carbon paper is hydrophobic but not superhydrophobic. The required pressure to push water inside the carbon paper micropores was measured and it was found that a pressure of over 5.2 kPa was needed to obtain a water flow through carbon paper [16]. The hydrostatic pressure during the deposition of $Ni(OH)_2$ depended on the liquid height, which was mostly 4 cm in our experiments. The hydrostatic pressure was roughly estimated as 0.4 kPa which was much lower than the water penetration pressure inside the pores of the carbon paper.

The deposited amount of $Ni(OH)_2$ depicts a linear relationship with the deposition time in HDP of nickel (Figure 3.3). This linearity shows that the release of OH^- anions by the decomposition of urea is constant during the entire deposition process. For the overall data shown in Figure 3.3, the $Ni(OH)_2$ deposited layer contained ~60 % nickel as determined by ICP. This value is in agreement with the

atomic mass percentage of nickel (63.3 %) in $Ni(OH)_2$. 0.2 mg (nickel)/cm^2 on a carbon paper (total area, 12.6 cm^2) was obtained in 24 hours by the HDP of nickel. When the deposition was stopped after only 8 hours, no $Ni(OH)_2$ deposition was observed under SEM. This indicates that the nucleation of $Ni(OH)_2$ crystallites takes much longer time on a standing carbon paper than for the case of carbon powders stirred in the solution. The absence of acid pretreatment in carbon paper can also account for the increased $Ni(OH)_2$ deposition time with respect to the acid pretreated carbon powders.

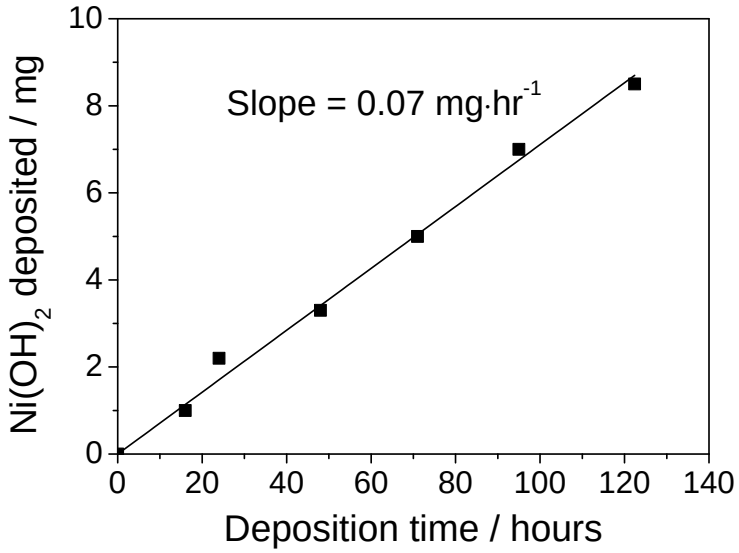

Figure 3.3 The amount of $Ni(OH)_2$ deposited on the carbon paper with respect to the time of deposition.

The deposition time of nickel not only determines the nickel loading on the carbon paper but also the porosity of the top layer. In Figure 3.4-a,b, SEM images of the $Ni(OH)_2$ depositions on carbon paper after 16 hours and after 95 hours are represented. The $Ni(OH)_2$ propagation started on the carbon paper fibers and filled the whole area including the holes present on the carbon paper after 95 hours deposition time.

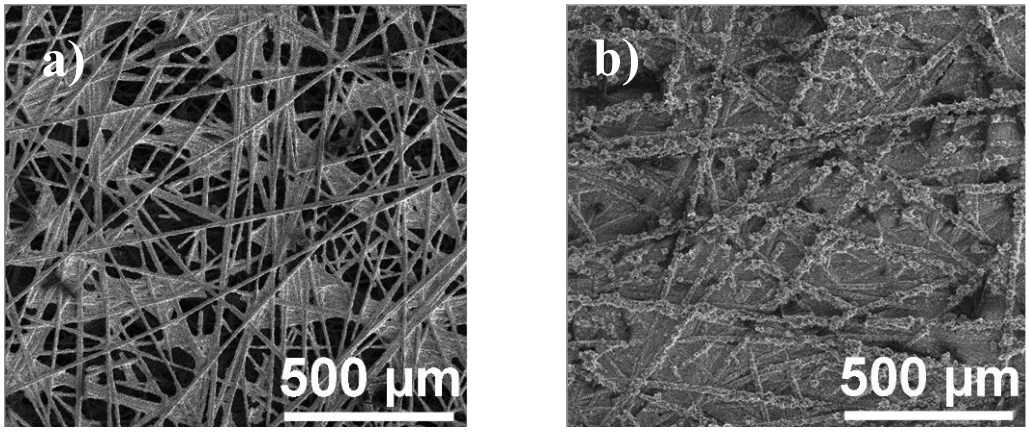

Figure 3.4 SEM images of the $Ni(OH)_2$ deposited side of carbon paper. After a) 16 hours; b) 95 hours of deposition.

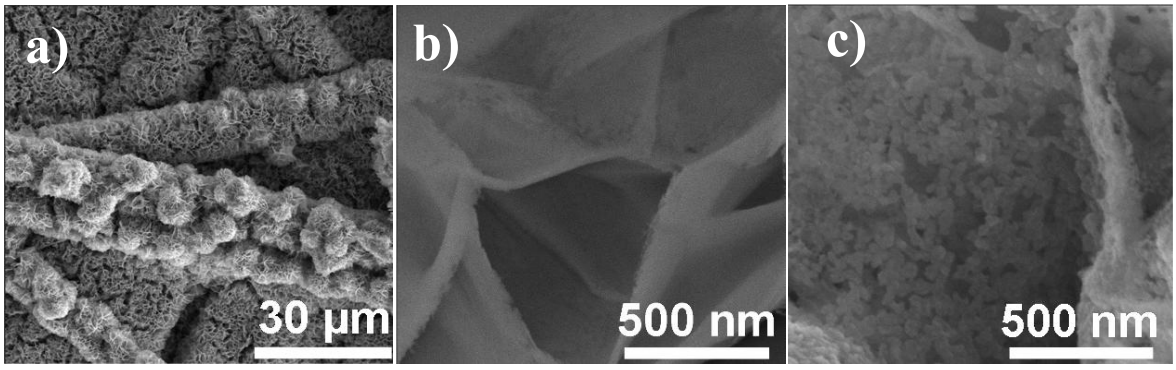

Figure 3.5 SEM images of the carbon paper after 24 hours of $Ni(OH)_2$ deposition: a) 1600x magnified (this image is also observed in the reduced $Ni(OH)_2$ coated carbon paper); b) 100,000x magnified image depicted in a; c) After the reduction of the sample shown in Figure 3.6-b.

It is important to note that the nickel is not deposited on the carbon paper only, but also on the walls of the glass deposition chamber and on the deposition holder. Therefore, the contact area of the nickel salt solution with its surroundings is important for the HDP of nickel on the carbon paper. The contact area of the nickel solution to the carbon paper was about 5 % of the total area of the solution contacting with the glass walls of the deposition chamber. This means that only 5 % of nickel is preferably deposited on carbon paper. Contact area minimization of

HDP can reduce the nickel content in the deposition solution providing a decrease in nickel catalyst cost in CNF growth.

The deposition of $Ni(OH)_2$ on carbon paper did not form a flat surface as seen in Figure 3.5-a,b. The surface of the carbon paper fibers is heterogeneous in terms of oxygen groups for nickel ion adsorption. Nickel ions are expected to be adsorbed only weakly on this hydrophobic and heterogeneous surface. The stronger adsorption of nickel ions on already deposited nickel is the cause of the formation of a leaflet $Ni(OH)_2$ layer with a mean thickness of approximately 15 nm. In the HDP of nickel on silica or alumina powders, flat platelet $Ni(OH)_2$ layers were obtained in recent studies [14, 15]. On a carbon substrate, a flat layer deposition was restricted since the nickel ions were not adsorbed continuously on the surface. This was also observed in the HDP of nickel applied on reticulated vitreous carbon (RVC) to grow CNFs for the development of a fully accessible graphitic catalyst support [17]. However, the obtained crystal structures were not homogeneous and leaflet structures were grown at the specific locations of the RVC. In this work, the $Ni(OH)_2$ crystallization was rather homogeneous in type and only leaflet $Ni(OH)_2$ layers were obtained. Apparently, the morphology of the carbon plays a crucial role in the crystallization of $Ni(OH)_2$. A nickel reduction step with hydrogen prior to the catalytic growth of CNFs removed the hydroxide and formed a complete black nickel layer. SEM images of the carbon paper with reduced nickel (Figure 3.5-c) showed that the macroscopic morphology of the leaflets was maintained (Figure 3.5-b). 100,000 times magnification reveals a porous structure of nickel nanoclusters. In Figure 3.5-c, it is seen that the microstructure changes compared to that of the $Ni(OH)_2$ layer at the same magnification shown in Figure 3.6-5.

XRD analysis performed on carbon paper, $Ni(OH)_2$ deposited carbon paper, reduced nickel carbon paper, and CNF-grown carbon paper are shown in Figure 3.6. The characteristic diffraction peaks and corresponding hexagonal planes assigned to carbon paper (d) are at 26.5°-(002), 42.4°-(100), 54.7°-(004), 77.4°-(110) [5]. $Ni(OH)_2$ peaks shown on (c) are at 33.4°-(100), 38.5°-(101), 59.0°-(110) [7]. After the reduction of $Ni(OH)_2$ with H_2, the $Ni(OH)_2$ peaks disappeared

completely and gave distinct nickel peaks shown on plot (b) at 44.5°-(111), 51.8°-(200), 76.4°-(220). Peaks obtained at 42.4°, 54.7°, 77.4° for carbon paper shown on plot (d) were the same as the peaks obtained for CNF-grown carbon paper. No additional peaks were observed for CNFs in plot (a). This demonstrates that the graphitic nature of the carbon paper and the CNFs is comparable. All the nickel diffraction peaks seen in plot (b) were also observed in plot (a). A weak peak observed at ~37° in plot (b) can be attributed to nickel oxide [18]. Nickel oxide formation was expected since after the reduction of $Ni(OH)_2$ to nickel, the sample was subjected to air at room temperature for the passivation of the catalyst surface. This peak disappeared in plot (a) indicating that the nickel oxide was reduced during the CNF growth to nickel.

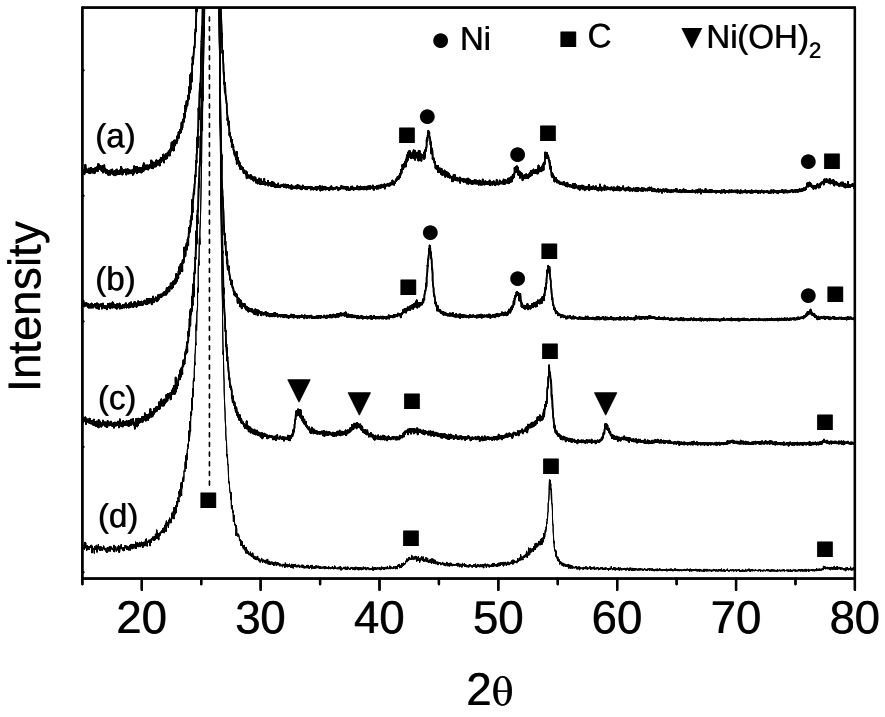

Figure 3.6 XRD analysis on: (a) CNF-grown carbon paper; (b) Reduced $Ni(OH)_2$ carbon paper; (c) $Ni(OH)_2$ coated carbon paper; (d) Carbon paper.

3.3.2 CNF growth on the nickel deposited carbon paper

Figure 3.7-a shows homogeneous CNF growth on the top surface of the carbon paper. Considering the importance of the catalyst layer thickness (5-15 μm) required in PEM fuel cell operations [19], the HDP of nickel on carbon paper fibers is an appropriate method since the amount of nickel deposited on the carbon paper determines the CNF-carbon paper fiber thickness. This thickness is represented by arrows shown in Figure 3.7-a and it is measured by using ImageJ software zooming 100 different locations in each counting. The results are depicted as a histogram plot in Figure 3.7-b. By adjusting the deposited amount of nickel with the time of deposition, the thickness of the carbon paper fibers can be tuned and the desired thickness can be obtained. After the $Ni(OH)_2$ deposition, the average thickness of the carbon paper fibers increased from 7 μm to 13 μm. After the growth of CNFs, the $Ni(OH)_2$ deposited layer was converted to a denser layer of CNFs increasing the average thickness of the carbon paper fibers to 15 μm. The total increase in thickness is approximately 115 %. The adhesion strength of the CNF layer was tested with ultrasonication for 30 minutes in ethanol and no significant loss (< 1 wt. %) was observed.

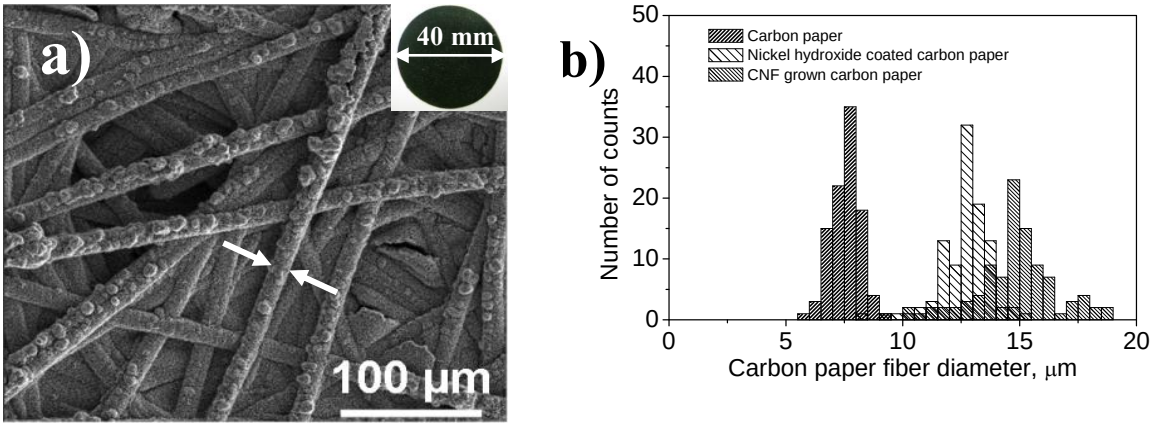

Figure 3.7 a) SEM image of the CNF grown carbon paper surface (24 hours HDP of nickel). Inset is a picture of the whole CNF-grown carbon paper; b) Histogram plots of fiber thicknesses show non-processed, $Ni(OH)_2$ deposited, and CNF grown carbon papers.

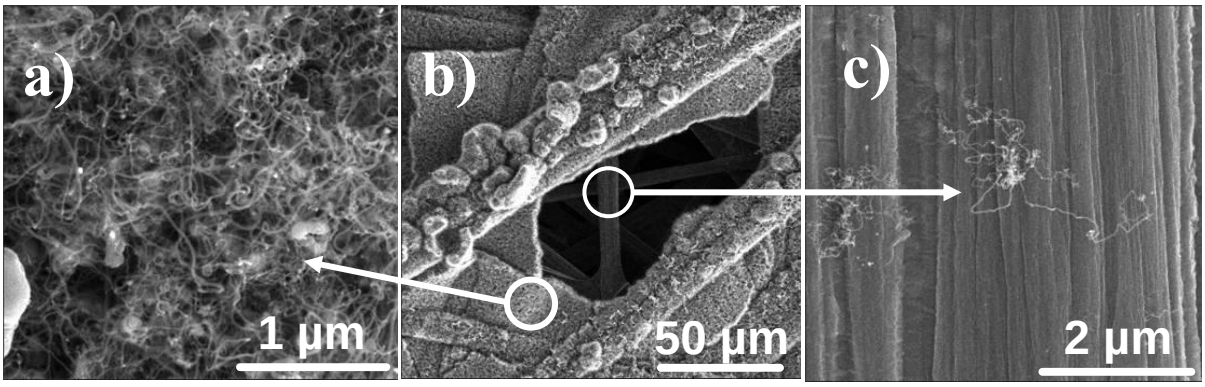

Figure 3.8 SEM images of CNFs on the carbon paper surface (24 hours HDP of nickel): a) Dense CNF regions; b) Top layer and adjacent layer; c) Focused adjacent layer of carbon paper fiber.

On the upper layers of the CNF grown carbon paper (Figure 3.8-a), a dense CNF network was observed since the amount of nickel on this area was relatively high. However, the underlying layer had fewer nickel nanocrystals (Figure 3.8-b). Therefore, only a few CNFs were grown on this layer (Figure 3.8-c) where it is seen that the CNFs grow from a nickel crystal. Multiple CNF growth from a single nickel nanocrystal was explained as octopus growth in a previous study performed with incipient wetness impregnation with a 1 wt.% nickel loading on carbon paper [10]. In this mechanism, active nickel (111) and (100) planes contribute to the CNF growth individually by detaching from the large nickel crystal [20]. Considering the size of the nickel crystallites (40-60 nm) formed after the reduction of $Ni(OH)_2$ (Figure 3.5-c), formation of 5-30 nm CNFs (Figure 3.9-a) provides a strong evidence for this mechanism. High resolution TEM images show (Figure 3.9-a,b) that the CNFs are mainly herringbone type with an angle of 45° to the growth axis. A small amount of CNFs in 50-100 nm thickness was observed in SEM and TEM images in Figure 3.8-a and Figure 3.9-c, respectively.

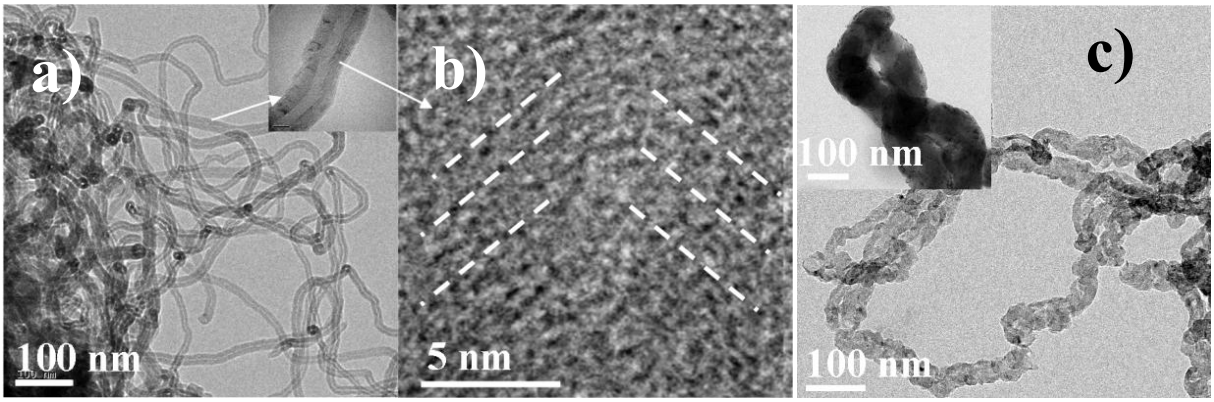

Figure 3.9 TEM images of: a) Herringbone CNFs; b) The inclined graphite planes of herringbone CNFs; c) 50-100 nm CNFs.

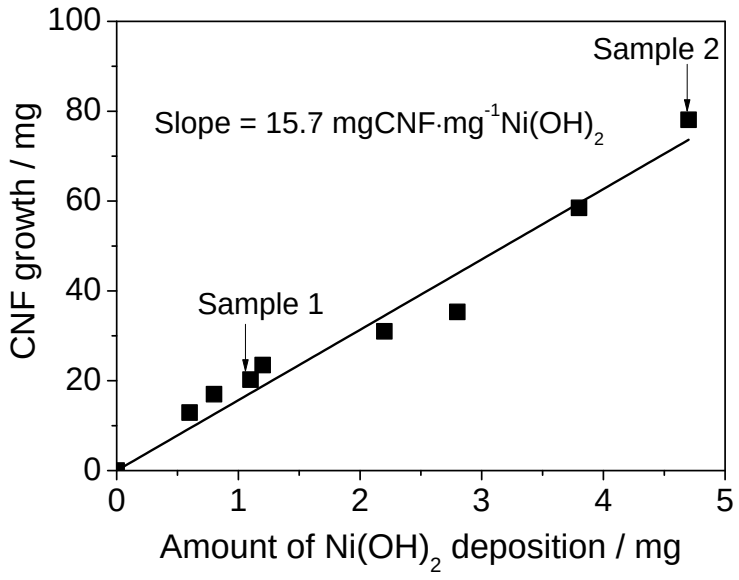

Figure 3.10 The amount of CNF-grown on carbon paper with respect to the amount of $Ni(OH)_2$ deposited.

The amount of CNFs grown on carbon paper has a linear dependence with the deposited amount of $Ni(OH)_2$ (Figure 3.10). This linear behavior shows that the increase in the loading of $Ni(OH)_2$ in the region of interest does not affect the amount of CNFs produced per nickel atom. The samples labeled as sample 1 and sample 2 in Figure 3.10 were analyzed with BET and mercury intrusion porosimetry and the results are tabulated in Table 3.1. The BET area of sample 2 is

approximately two times of the BET area of sample 1. The BET area of the CNF-grown carbon paper increased linearly with the amount of CNFs grown on the carbon paper. The BET areas of the CNFs were calculated as 181 ± 1 for sample 1 and 177 ± 2 $m^2 \cdot g^{-1}$ for sample 2. The BET area did not change with respect to the amount of nickel catalyst deposited on the carbon paper. The constant BET area of CNFs shows that the average CNF thickness remains constant since thicker CNFs decrease the surface to volume ratio of CNFs and therefore the BET area. The CNF growth on the carbon paper decreased the porosity to 66.3 ± 0.1 % from 78 % for sample 1 and to 58.1 ± 0.1 from 78 % for sample 2 (Table 3.1).

Table 3.1 Properties of the CNF grown carbon paper.

	CNF-grown carbon paper		Carbon paper
	Sample 1	Sample 2	
Nickel loading on carbon paper (wt.%)	1.1 ± 0.1	4.1 ± 0.1	-
CNF grown on carbon paper (wt.%)	17.3 ± 0.1	41.1 ± 0.1	-
CNF carbon paper BET ($m^2 \cdot g^{-1}$)	31 ± 1	70 ± 2	-
CNF-BET (calculated) ($m^2 \cdot g^{-1}$)	181 ± 1	177 ± 2	0.2 ± 1.0
CNF-carbon paper porosity, %	66.3 ± 0.1	58.1 ± 0.1	78 ± 0.1

Operation of a PEM fuel cell in the acidic environment of the anode may leach the nickel and decrease the rate of proton transfer through the membrane because of metal poisoning in the membrane. A nickel removal study was performed with 65 vol.% HNO_3 at reflux temperature for 4 hours on CNF grown carbon paper. Such an aggressive treatment did not affect the CNF-carbon paper structure and weight loss was not observed. The presence of nickel in the EDX measurements (figure is not shown here) shows that this acid treatment is not sufficient to remove encapsulated nickel crystals. It had been reported previously that 10 wt.% of the Co-Ni bimetallic CNF growth catalyst was not removed after 4 N of H_2SO_4/HNO_3 treatment at reflux temperature [13]. It was also shown in another metal removal study that more than 10 wt.% of the metal remained on the CNFs after 4 hours treatment at reflux temperature with 4 M HNO_3 [21]. These

reports are in agreement with our study on the removal of nickel and it is believed that the nickel dissolution is not probable in the PEM fuel cell environment. Therefore, nickel crystals will not be harmful in PEM fuel cell operation and no additional removal is required.

3.4 Concluding remarks

This chapter presents the homogeneous deposition precipitation (HDP) of nickel hydroxide ($Ni(OH)_2$) on the carbon paper and the subsequent catalytic growth of CNFs. Selective $Ni(OH)_2$ deposition on one side of the carbon paper was achieved by making use of the hydrophobic nature of the carbon paper. Throughout the deposition procedure, the $Ni(OH)_2$ deposition formed leaflet layers without altering its structure. This indicates that the $Ni(OH)_2$ side planes did not contributed to the $Ni(OH)_2$ deposition after a critical leaflet thickness, and thus the growth of $Ni(OH)_2$ layers was confined in one direction. CNF growth was performed on the nickel deposited carbon paper and herringbone CNFs (45° with growth axis) were obtained. A minor amount of the bigger (> 100 nm) CNFs was produced, most likely by bigger active nickel crystallites. Continuous growth over the surface of carbon paper was obtained in a layer of 5 to15 μm depth of the carbon paper from the top surface. The strong attachment of $Ni(OH)_2$ and CNFs to the carbon paper fibers was confirmed by ultrasonication tests. The HDP of nickel provides a highly controlled nickel deposition with reproducible growth of CNFs on the carbon paper. CNF-grown carbon paper is likely to be suitable for tailoring the water management of the GDM and using as a direct catalyst support for PEM fuel cells.

Appendix: Selection of nickel as a catalyst source

The growth of carbon nanofibers (CNFs) has been achieved with various catalysts on different supports over the last two decades [22-29]. These catalysts are produced in various forms including nanoparticles and metal complexes. These growth techniques are mainly based on the production of loose fibers, which are mainly supported on silica and alumina particles. The direct growth of CNFs on carbon paper has been investigated by many researchers with different catalysts morphologies. Ferrocene impregnation into carbon paper [30], Ni-Co nanoparticle attachment [8, 31, 32], electrodeposition of Co-Ni alloys [13] and Co [33] are such examples. In chapter 3, we have reported the use of nickel hydroxide for the production of CNFs forests directly grown on carbon paper. In this part, nickel hydroxide will be compared with the other two catalysts, iron (II) hydroxide and cobalt hydroxide and the reasons for the selection of nickel will be addressed.

Homogeneous deposition precipitation (HDP) of Ni, Co, Fe (II) on carbon paper (TP-H-060, Toray Industries, Figure 3.3-a,b) was performed with a mask deposition holder as described in the experimental section. The molar ratios of Ni, Co and Fe(II) were kept equal to compare the deposition of the metals and the growth of CNFs. 1.2 mmol of Ni, Co or Fe(II) solutions were prepared in 300 ml DI water and mixed with 50 ml 60 mM urea solution. The pHs of the solutions were adjusted to ~2.4 using 0.5 M nitric acid at 90 °C. Then, 50 ml 60 mM urea solution was added. The molar ratio of urea to Ni, Co or Fe(II) was 2.5 in the final solution. The growth of CNFs was performed in the vertical tubular reactor explained in chapter 3. Scanning electron microscopy (SEM, FEI Quanta 3D FEG) was used to identify the growth of CNFs and the morphology of the hydroxide layers on the carbon paper.

As discussed in chapter 3, $Ni(OH)_2$ deposition on carbon paper completely covers the pores larger than 25 μm. The growth of CNFs makes a dense hairy layer on those regions. The growth of CNFs, in this way, is aimed to prevent the condensation of water molecules in the cathode part of the PEM fuel cell.

The deposition of $Ni(OH)_2$ results in a uniform and completely covered surface if the deposition continues longer than 72 hours. This uniformity and complete coverage was also observed for $Co(OH)_2$ deposition on carbon paper. Compared to $Ni(OH)_2$, which has light green deposition color, a blue colored surface is observed in $Co(OH)_2$ (Figure 3.A.1). However, $Fe(OH)_x$ does not uniformly deposited on the surface. Longer experiments and highly concentrated Fe(II) solutions did not deposit uniform iron hydroxide layers and it makes improper depositions on the carbon paper. As described in chapter 2, pH rise from 2.4 to 7.0 is a critical step in HDP of nickel. The pH rise of cobalt solution is similar to nickel solution but is different from iron solution. Mostly, Fe(II) oxidizes to Fe(III) at higher temperature and can be deposited as different forms of iron oxide. In the X-ray study of the iron deposited carbon paper, various forms of iron have been observed including iron (III) oxide, iron (II) hydroxide, Iron (III) hydroxide. Not only the deposition difficulties and improper coverage (Figure 3.A.2), but also iron deposited carbon paper did not form any observed CNF growth. Therefore, iron hydroxide as a catalyst source was not selected and left out in this study.

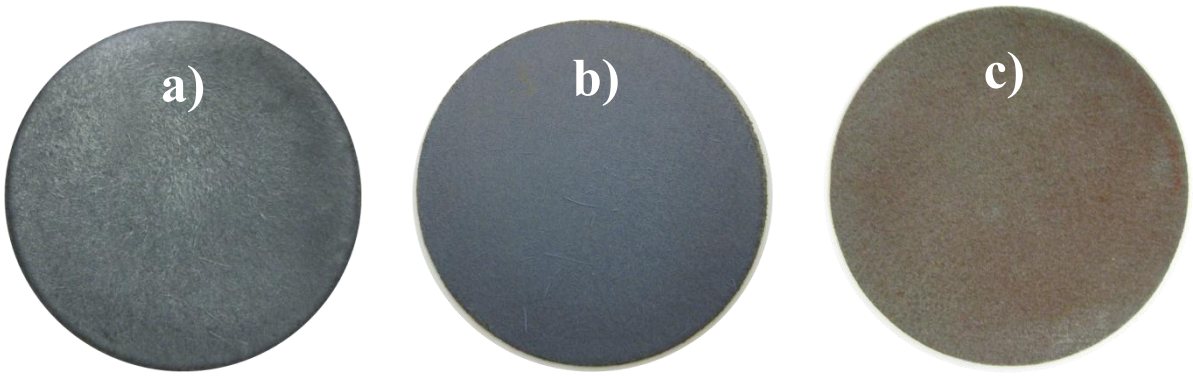

Figure 3.A.1 Images of a) $Ni(OH)_2$, b) $Co(OH)_2$ and c) $Fe(OH)_x$ on 40 mm carbon paper after 72 hours of deposition.

As it was shown in Figure 3.5, the deposition of $Ni(OH)_2$ formed leaflet type structures on the carbon paper surface. These leaflet structures $Ni(OH)_2$ layer

covered the entire carbon paper surface. When the nickel is replaced by cobalt in the same concentration and the molar ratio (urea/Ni or Co), a different morphology

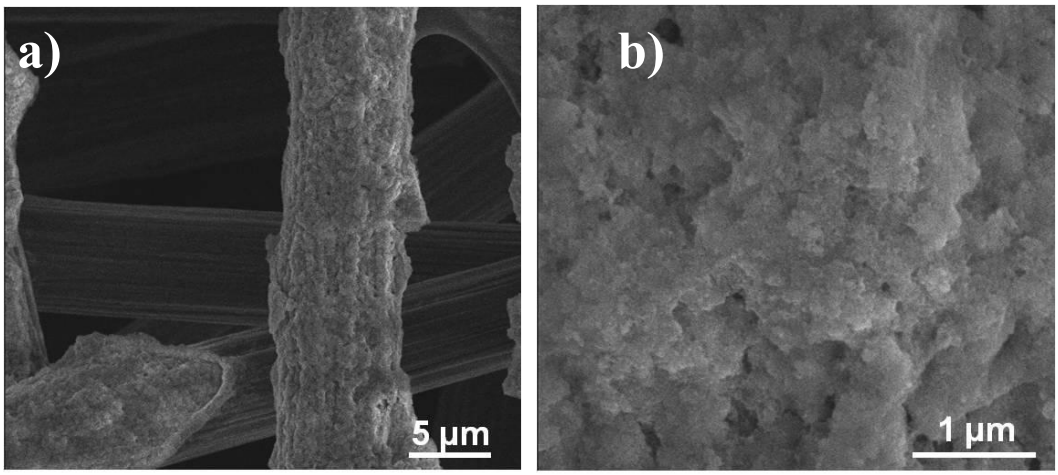

Figure 3.A.2 SEM images of the $Fe(OH)_x$ deposited side of carbon paper. a) General overview, b) magnified view. Here, there is no repeating structure observed on the surface. Disordered iron complexes are formed on carbon paper surface.

is obtained. In Figure 3.A.3, It is seen that $Co(OH)_2$ are grown as tubular fibers and it covers the entire carbon paper area. Changing the metal from nickel to cobalt completely change the deposition morphology. Growth mechanisms of hydroxide layers of nickel and cobalt reveal a significant difference in the coordination chemistry of the hydroxides on these metals during the deposition. Such tubular structures of $Co(OH)_2$ were also observed by Kovalenko et al on a ceramic foam [34] and aluminum oxide [35]. Kovalenko et al reported that the average yield of CNFs on cobalt deposited ceramic foam is five times less than the nickel deposited one. The growth temperature affects the pyrolysis of the carbon source on the cobalt and higher growth temperatures results in longer CNFs on cobalt deposited aluminum compounds. The investigation of the coordination chemistry of metals during the deposition and the pyrolysis of the reactant gas containing carbon on the metals are beyond the scope of this thesis, and thereby nickel was selected as a growth catalyst on carbon paper.

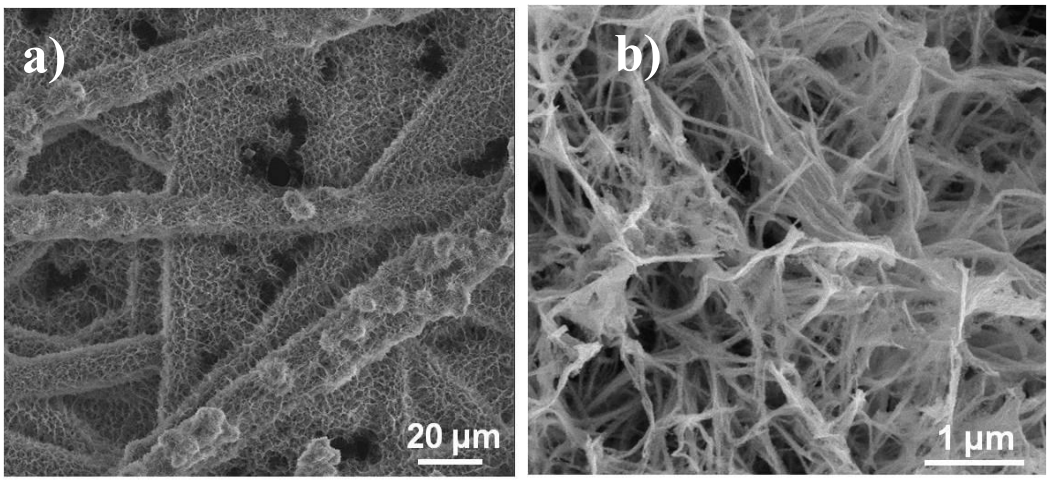

Figure 3.A.3 SEM images of the $Co(OH)_2$ deposited side of carbon paper. a) General overview, b) magnified view. Here, the tubular structures of $Co(OH)_2$ are seen.

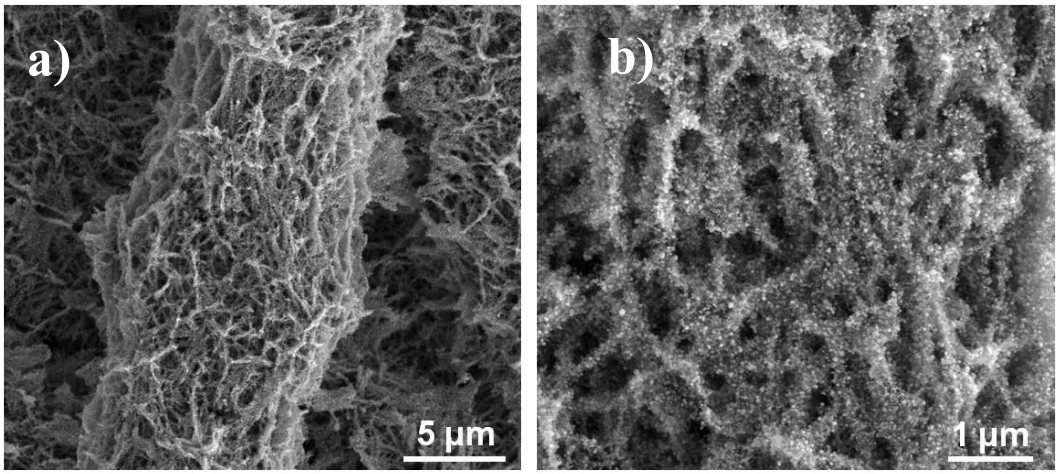

Figure 3.A.4 SEM images of the cobalt deposited carbon paper after CNF growth. a) General overview, b) magnified view.

Comparing the three catalysts, nickel, cobalt and iron, nickel and cobalt make the best continuous and repeating structures on the carbon paper surface without the need of any oxidation on the carbon paper. Although this looks promising for both catalyst to be used in the production of CNFs on carbon paper, it is seen that the growth of CNFs by $Co(OH)_2$ deposited carbon paper was rather unsuccessful as shown in Figure 3.A.4. The tubular structures of $Co(OH)_2$ are reduced to cobalt nanoparticles and many nanoparticles are formed. However, the

general overview did not change as shown in Figure 3.A.4-a. Although cobalt is known as a CNF growth catalyst, under these growth conditions only a few CNFs are grown. The same reduction and growth temperatures in $Ni(OH)_2$ deposited carbon paper results in a production of 15.7 mg CNF per mg of nickel as shown in Figures 3.8 and 3.10. The growth of CNFs by cobalt on carbon paper was rather poor compared to nickel at a growth temperature of 600 °C. The growth temperature of cobalt deposited carbon paper was increased up to 800 °C however, no significant change in CNF yield was observed.

Because of the practical reasons discussed above, nickel was selected as a suitable deposition catalyst in homogeneous deposition precipitation on carbon paper.

References

[1] F.A. de Bruijn, V.A.T. Dam, G.J.M. Janssen, Fuel Cells, 8 (2008) 3-22.

[2] S. Varigonda, M. Kamat, Computers & Chemical Engineering, 30 (2006) 1735-1748.

[3] R.K. Ishii, in: First International Conference on Energy Efficiency and Conservation, Hong Kong, 2003, pp. 57-73.

[4] S. Perathoner, M. Gangeri, P. Lanzafame, G. Centi, Kinet Catal, 48 (2007) 877-883.

[5] W.Z. Li, C.H. Liang, W.J. Zhou, J.S. Qiu, Z.H. Zhou, G.Q. Sun, Q. Xin, J Phys Chem B, 107 (2003) 6292-6299.

[6] P. Ramesh, M.E. Itkis, J.M. Tang, R.C. Haddon, J Phys Chem, 112 (2008) 9089-9094.

[7] F. Yuan, H.K. Yu, H. Ryu, Electrochimica Acta, 50 (2004) 685-691.

[8] C.Y. Du, B.R. Wang, X.Q. Cheng, J Power Sources, 187 (2009) 505-508.

[9] H. Tang, J.H. Chen, L.H. Nie, D.Y. Liu, W. Deng, Y.F. Kuang, S.Z. Yao, J Colloid Interf Sci, 269 (2004) 26-31.

[10] B. Louis, R. Vieira, A. Carvalho, J. Amadou, M.J. Ledoux, C. Pham-Huu, Top Catal, 45 (2007) 75-80.

[11] T. Bordjiba, M. Mohamedi, L.H. Dao, Nanotechnology, 18 (2007) 1-5.

[12] H. Inoue, H. Daiguji, E. Hihara, Jsme. Int J B-Fluid T, 47 (2004) 228-234.

[13] X. Wang, M. Waje, Y.S. Yan, Electrochemical and Solid State Letters, 8 (2005) A42-A44.

[14] M.L. Toebes, J.H. Bitter, A.J. van Dillen, K.P. de Jong, Catal Today, 76 (2002) 33-42.

[15] M.K. van der Lee, A.J. van Dillen, J.H. Bitter, K.P. de Jong, J Am Chem Soc, 127 (2005) 13573-13582.

[16] S. Bliznakov, Y. Liu, N. Dimitrov, J. Garnica, R. Sedev, Langmuir, 25 (2009) 4760-4766.

[17] P.W.A.M. Wenmakers, J. van der Schaaf, B.F.M. Kuster, J.C. Schouten, J Mater Chem, 18 (2008) 2426-2436.

[18] D. Chen, K.O. Christensen, E. Ochoa-Fernandez, Z.X. Yu, B. Totdal, N. Latorre, A. Monzon, A. Holmen, J Catal, 229 (2005) 82-96.

[19] F.A. de Bruijn, R.C. Makkus, R.K.A.M. Mallant, G.J.M. Janssen, K.D.K. T.S. Zhao, N. Trung Van, Chapter Five Materials for State-of-the-Art PEM Fuel Cells, and Their Suitability for Operation Above 100°C, in: Advances in Fuel Cells, Elsevier Science, 2007, pp. 235-336.

[20] I. Alstrup, J Catal, 109 (1988) 241-251.

[21] E. Dujardin, T.W. Ebbesen, A. Krishnan, M.M.J. Treacy, Adv Mater, 10 (1998) 611.

[22] T. Matsuda, M. Mesko, T. Ishikawa, J. Sato, A. Ogino, R. Tamura, M. Japanese J Appl Phys, 47 (2008) 7436-7439.
[23] A. Kukovecz, Z. Konya, N. Nagaraju, I. Willems, A. Tamasi, A. Fonseca, J.B. Nagy, I. Kiricsi, Phys Chem Phys, 2 (2000) 3071-3076.
[24] K. Otsuka, H. Ogihara, S. Takenaka, Carbon, 41 (2003) 223-233.
[25] J.T. Han, J.H. Woo, H.S. Kim, J.G. Jee, B Kor Chem Soc, 24 (2003) 1771-1774.
[26] C. Laurent, E. Flahaut, A. Peigney, A. Rousset, New J Chem, 22 (1998) 1229-1237.
[27] B. Li, C.F. Goh, X.Z. Zhou, G. Lu, H. Tantang, Y.H. Chen, C. Xue, F.Y.C. Boey, H. Zhang, Adv Mater, 20 (2008) 4873.
[28] Y. Yamada, Y. Hosono, N. Murakoshi, N. Higashi, H. Ichi-oka, T. Miyake, N. Ikenaga, T. Suzuki, Diamond and Related Mater, 15 (2006) 1080-1084.
[29] P.M. Campbell, E.S. Snow, J.P. Novak, Appl Phys Letters, 81 (2002) 4586-4588.
[30] P.H. Maheshwari, R.B. Mathur, Electrochimica Acta, 54 (2009) 7476-7482.
[31] M.M. Waje, X. Wang, W.Z. Li, Y.S. Yan, Nanotechnology, 16 (2005) S395-S400.
[32] J.P. Dodelet, D. Villers, S.H. Sun, A.M. Serventi, S. Desilets, J Phys Chem B, 110 (2006) 25916-25925.
[33] C. Wang, M. Waje, X. Wang, J.M. Tang, R.C. Haddon, Y.S. Yan, Nano Letters, 4 (2004) 345-348.
[34] G.A. Kovalenko, N.A. Rudina, T.V. Chuenko, L.V. Perminova, T.G. Terent'eva, A.S. Rozanov, S.N. Zagrebel'nyi, Kinet Catal, 48 (2007) 757-764.
[35] G.A. Kovalenko, N.A. Rudina, L.V. Perminova, O.V. Skrypnik, Kinet Catal, 51 (2010) 449-455.

Preliminary studies of the effect of CNF grown carbon paper on PEM fuel cell performance

4

Abstract

The impact on the performance of a proton exchange membrane fuel cell of using carbon nanofibers (CNFs) grown directly on a carbon paper was investigated. The CNF grown carbon paper was considered as a microporous layer without using polytetrafluoroethylene. The polarization curves showed that in comparison to a commercial microporous layer coated carbon paper, the catalyst layer backed by the CNF grown carbon paper improved the fuel cell performance at high current densities, while flooding occurred at low current densities. Increasing the fuel cell temperature or the reactant gas flow mitigated the flooding, but in this case the positive contribution of the CNF did not surpass the contribution of the commercial microporous layer. The CNF grown carbon paper improved the oxygen diffusion through enhanced water management under wet conditions.

4.1 Introduction

Proton exchange membrane (PEM) fuel cells are electricity generators considered suitable for various applications including automobiles, stationary power sources and portable electric devices [1]. Considerable effort has been given to commercialize PEM fuel cells in the last two decades to reduce the greenhouse effect of fossil fuels. However, there are still some obstacles that need to be tackled for a widespread commercialization of fuel cells, such as the high platinum (Pt) catalyst cost, membrane degradation and the necessity of auxiliary units to maintain an optimal operation environment [2, 3]. Particularly, PEM fuel cells operating at temperatures below 100 °C demand water management in the catalyst layers of the anode and the cathode electrodes in order to minimize unnecessary voltage losses and, thereby achieve high power outputs at high current densities [4-6].

The design of a bilayer diffusion medium constructed with a hydrophobic dense microporous layer (MPL) and a conventional gas diffusion layer (GDL) has improved the fuel cell performance in the recent years [7-12]. The addition of a MPL reduces flooding in the porous cathode and enhances water management by pushing the liquid water across the membrane from the cathode to the anode. This reduces the water saturation levels and enhances the gas transport [13]. The application of CNFs on a GDL as a MPL layer is considered a new enhancement factor in both the electronic conductivity and the gas permeability [14-16].

In chapters 2 and 3, the direct growth of CNFs on a GDL has been discussed. In this chapter, a single side CNF grown GDL was tested in a single cell fuel cell test station in both dry and fully humidified oxygen and air atmosphere. Anode and cathode gas stoichiometries, type of oxidant (pure oxygen or air) and operating temperature of the PEM fuel cell were varied to characterize the CNF grown GDL.

4.2 Experimental

4.2.1 Direct growth of carbon nanofibers on carbon paper

CNFs were directly grown by the decomposition of ethylene on a single side nickel deposited carbon paper (TGP-H-060, Toray, 4.0 cm in diameter and 106 mg in total) at 600 °C in a vertical tubular reactor. Prior to the growth of CNFs, 1.8 mg of nickel hydroxide was deposited and then reduced to nickel in the presence of 10 vol.% hydrogen in nitrogen. 23.5 mg of CNF was grown leading to a final CNF loading of 20 wt.% on the carbon paper (Figure 4.1-a,b). The details of the nickel hydroxide deposition and CNF synthesis procedures are described in chapter 3.

4.2.2 Preparation of membrane electrode assembly

Carbon paper (TGP-H-060, Toray) was used as the base GDL material. The prepared sample with a CNF layer was compared with a commercial GDL containing 10% polytetrafluoroethlene (PTFE) and a thin MPL (based on carbon and 10% PTFE) as supplied by Johnson Matthey. Electrodes were prepared using an ink based on Hispec 9100 Pt (60%)/C catalyst (5%), DE1021 Nafion solution from Ion Power (24%), and 1,2-propanediol as a solvent [17]. This ink was mixed by ultrasonification for one hour and stirred overnight before DEK screen-printing in contact mode. Printing was first attempted on the GDLs, but the prepared CNF grown GDL suffered significantly from ink penetration compared to the commercial GDL. In order to obtain a fair comparison, additional decal printing on skive PTFE sheet was performed using the same ink. Catalyst coated membranes were made by transferring the decals onto a Nafion NRE-211CS membrane at 135 °C and 50 bar pressure for a period of 2 min. The GDL was hot-laminated in a second step at the same temperature but at a lower pressure of 15 bar. The resulting membrane electrode assembly (MEA) contained an asymmetric GDL configuration with the CNF grown GDL (no PTFE) on one side and the commercial GDL on the other side as a reference. The Pt loading at the anode amounted to 0.56 $mg \cdot cm^{-2}$, while at the cathode the Pt loading amounted to 0.68 $mg \cdot cm^{-2}$.

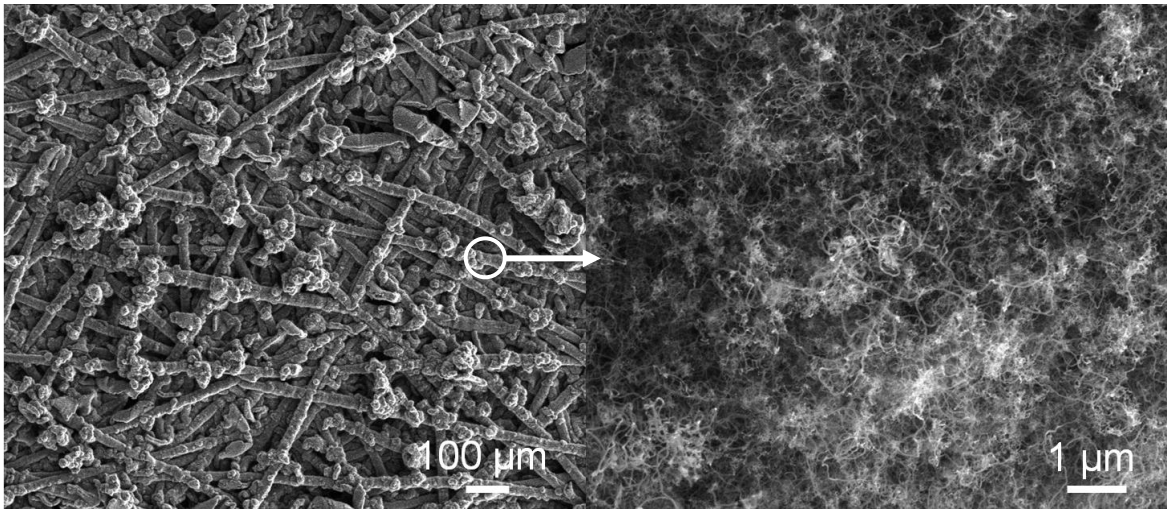

Figure 4.1 SEM pictures of a) single side CNF grown carbon paper and b) CNFs (magnified view).

4.2.3 Cell operation and electrochemical characterizations

The MEA had a circular active area of 8 cm^2 and was installed in 5 W single cell test station located in the Energy Research Centre of the Netherlands (ECN). The graphite flow field consisted of a single serpentine structure with channel dimensions of 1x1 mm^2 cross section at 1 mm spacing (lands). A pneumatic cell compression was used of 2 bar, the sealing provided by Viton O-rings. Heating elements were used to regulate the temperature of the cell as well as the integrated membrane humidifier. Unless this humidifier was bypassed for dry air operation, the dew point of the feed gasses was the same as the cell temperature, here being 65 or 80 °C.

The MEA was conditioned by applying a constant current load of 400 $mA \cdot cm^{-2}$ for a period of at least 24 hours with intermittent open circuit voltage (OCV) exposure for 1 minute in every hour. Polarization tests were conducted starting from the OCV and recording the voltage for at least 1 minute (until stable) while sweeping the current load up to a preset current density, before reversing the sequence and stepping back to the OCV. Both curves are reported to show possible hysteresis effects that may exist during operation under air and oxygen atmosphere.

MEA diagnostic measurements were conducted on a Zahner potentiostat and consisted of Electrochemical Impedance Spectroscopy (EIS), 100 kHz-1 Hz, 5 mV amplitude, hydrogen cross-over (0.43 V vs. NHE, 1 hr) and Cyclic Voltammograms (CV -3rd scan, 0.06 – 1 V, 20 mV·s^{-1}) to determine the catalyst surface area from the H_{upd} peaks under 0.43 V.

The fabricated MEAs were tested at cell temperatures of 65 and 80 °C under fully humidified air and oxygen streams. Initially, the MEA was tested with the CNF grown GDL at the cathode and the commercial GDL at the anode. After the first set of polarization tests, the gas connections on the cell hardware were switched to operate the cell with the CNF grown GDL at the anode and the commercial GDL at the cathode, and the cell performance was re-measured under exactly the same operating conditions to distinguish the influence of the GDLs. Gas switching was repeated after each characterization test to ensure the complete MEA was fully conditioned and both electrodes shared the same history.

4.3 Results and discussion

The combined polarization curves are shown in Figure 4.2 for the MEA with the CNF grown GDL at the cathode. The hysteresis is indicative for the stability of the fuel cell operation, where the current density was first increased from zero to higher values (air down) and then decreased back to zero to reach OCV (air up).

At the operating temperature of 65 °C, a strong hysteresis was observed between air down and air up curves. A typical voltage minimum was observed at a current density of 0.5 A·cm^{-2} on the air down curve which shifted to 0.2 A·cm^{-2} on the air-up curve. Most remarkable is the high level of recovery observed on the kick-up following the minimum, achieving 62 and 67 mV separation between air and oxygen curve at 1 A·cm^{-2} on the air down and air up, respectively. Interestingly, this phenomenon disappeared completely when increasing the cell operating temperature to 80 °C. The oxygen polarization curves showed no such hysteresis and showed similar characteristics at both operating temperatures of 65 and 80 °C.

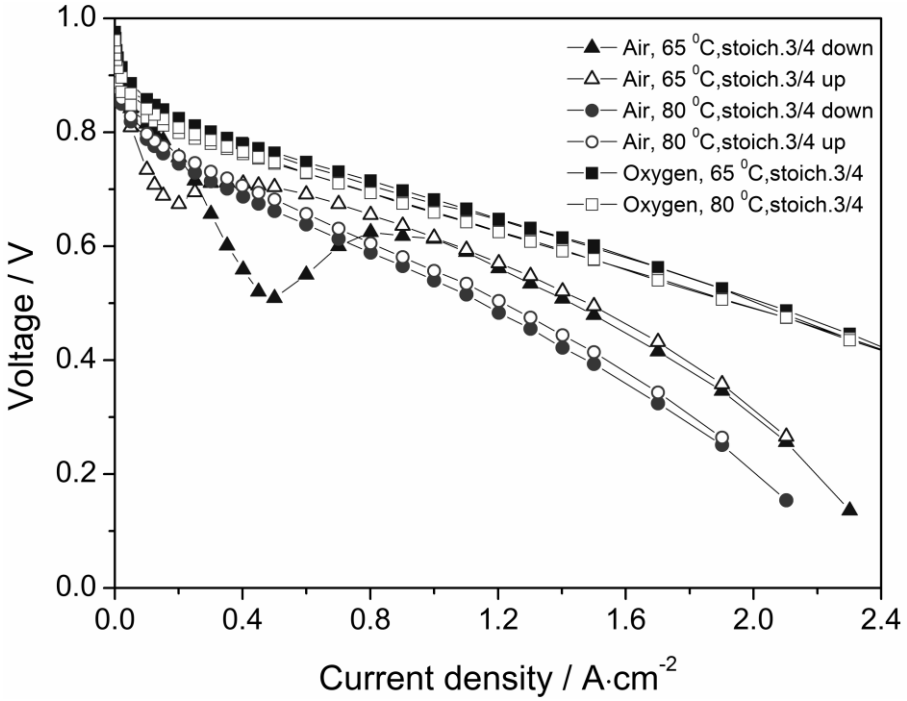

Figure 4.2 Polarization curves of the MEA operated at 65 °C and 80 °C. Here the MEA is operated with a stoichiometric ratio of 3.0 for the anode and 4.0 for the cathode. All polarization curves were swept from OCV to high current density (air down) and back (air up).

The most plausible cause for the voltage minimum is the water accumulation in the electrodes, also known as flooding, limiting the diffusion of oxygen. The limited oxygen diffusion quickly becomes critical under the air atmosphere, as demonstrated by the influence of gas flows. When applying lower stoichiometric ratios of 1.5||2.0* instead of 3.0||4.0, the polarization curve suffered from increased voltage losses and continued to decrease beyond the previously discussed voltage minimum observed at 0.5 A·cm^{-2}. In other words, no recovery was observed. Apparently, the feed gasses require a specific gas flow rate to be able to clear out the water responsible for flooding of particularly the cathode electrode at a fuel cell operating temperature of 65 °C. A high air stoichiometric ratio of 3.0||4.0 also assures that there is no water formation in the graphite flow fields [18].

*1.5||2.0 defines the stoichiometric ratio of the feed gas which is 1.5 at the anode and 2.0 at the cathode.

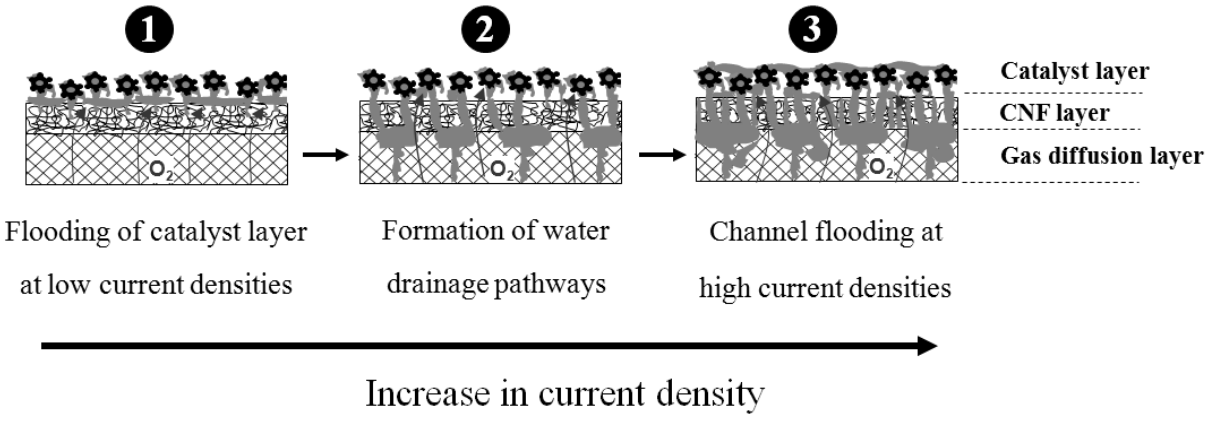

Figure 4.3 Representation of water formation in the catalyst layer, the CNF layer and the GDL. (1) Accumulation of water on the catalyst layer; (2) Capillary drying of liquid water along carbon nanofibers through capillary action; (3) Flooding observed as liquid water fills the open pores in the MPL, blocking the oxygen transport.

The fuel cell with a CNF grown GDL was capable of achieving high air power densities of 0.74 $W \cdot cm^{-2}$ at 65 °C under fully humidified conditions, provided the liquid water did not obstruct the diffusion of oxygen to the catalyst layer. The important factor to consider is not the absolute amount of water, but the water distribution in the cathode electrode. The reason for the performance recovery at the current density of 0.8 $A \cdot cm^{-2}$ and at the temperature of 65 °C is a revived rate of liquid water transport through the capillaries formed within the CNF layer. Assisted by an increased gas flow, the water produced by the oxygen reduction reaction was efficiently drained away from the cathode catalyst layer by capillary drying along the CNF layer, opening up more gas transport channels for the oxygen diffusion. Sequentially, due to operation at a constant stoichiometry, the gas flow was decreased during the up-sweep of the polarization curve to lower current densities and the already open gas transport channels slowly started to fill up with the accumulated liquid water. Again, a voltage minimum was observed, but at a later stage.

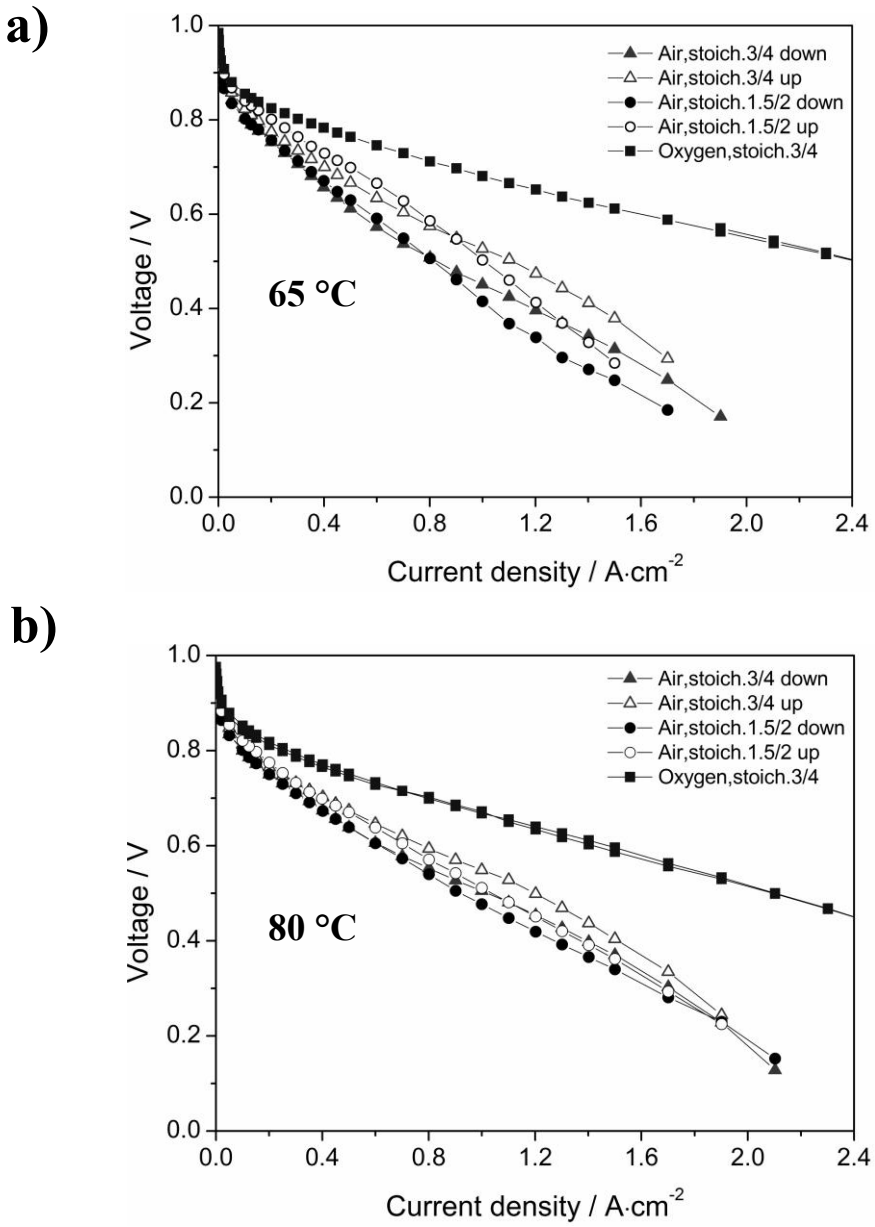

Figure 4.4 Polarization curves of the reverse operation of the MEA. Cathode: commercial MPL-GDL, anode: CNF grown GDL. Voltage-current diagrams at a) 65 °C and b) 80 °C. Stoichiometric ratios are varied in reverse operation from 1.5||2.0 to 3.0||4.0.

The amount of oxygen transported to the catalyst layer is a critical factor in air operation and mass transport limitation of oxygen is observed at current densities between 0.1 and 0.8 $A \cdot cm^{-2}$. Beyond a current density of 0.8 $A \cdot cm^{-2}$, the performance recovered itself and appeared unaffected by flooding until 1.5 $A \cdot cm^{-2}$. Note that the air mass flow controller was at its maximum beyond 1.1 $A \cdot cm^{-2}$ and

the hydrogen mass flow controller beyond 1.9 A·cm^{-2}, so the apparent transient effect on air performance was in fact due to a gradually decreasing stoichiometry.

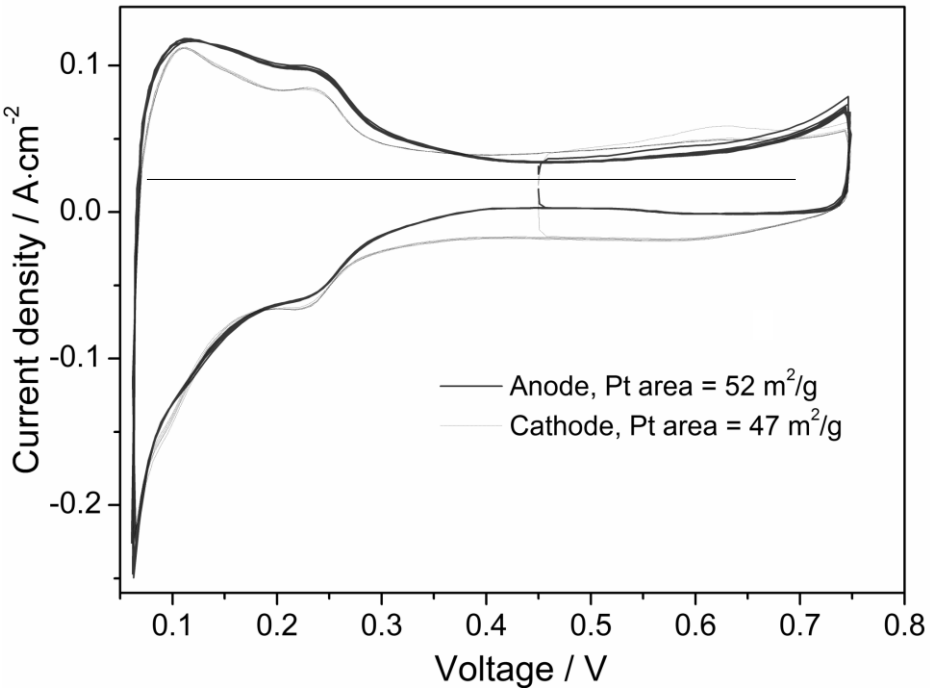

Figure 4.5 Cyclic voltammograms of both the anode and the cathode part of the MEA.

The perceived mechanism of gas-flow assisted water removal via the CNF layer is schematically drawn in Figure 4.3 where the three stages have been depicted. First water accumulates in the smallest pores in the catalyst layer at low current densities, leaving the pores in the MPL sufficiently open for oxygen diffusion. These pores gradually fill up as the liquid water also penetrates into the MPL with increased current density (*i.e.* water production rate). High reaction rates demand increased oxygen supply rates which strain the oxygen diffusion rate, particularly in an air atmosphere. The observed performance recovery in air indicates that at even higher current densities, the oxygen supply is no longer critical, suggesting that the quantity of open pores available for gas diffusion has increased. A change in the distribution of liquid water could explain why the fuel cell air performance can suddenly come so close to the oxygen performance around 1.0 A·cm^{-2} where the small difference is accounted for the higher oxygen partial pressure.

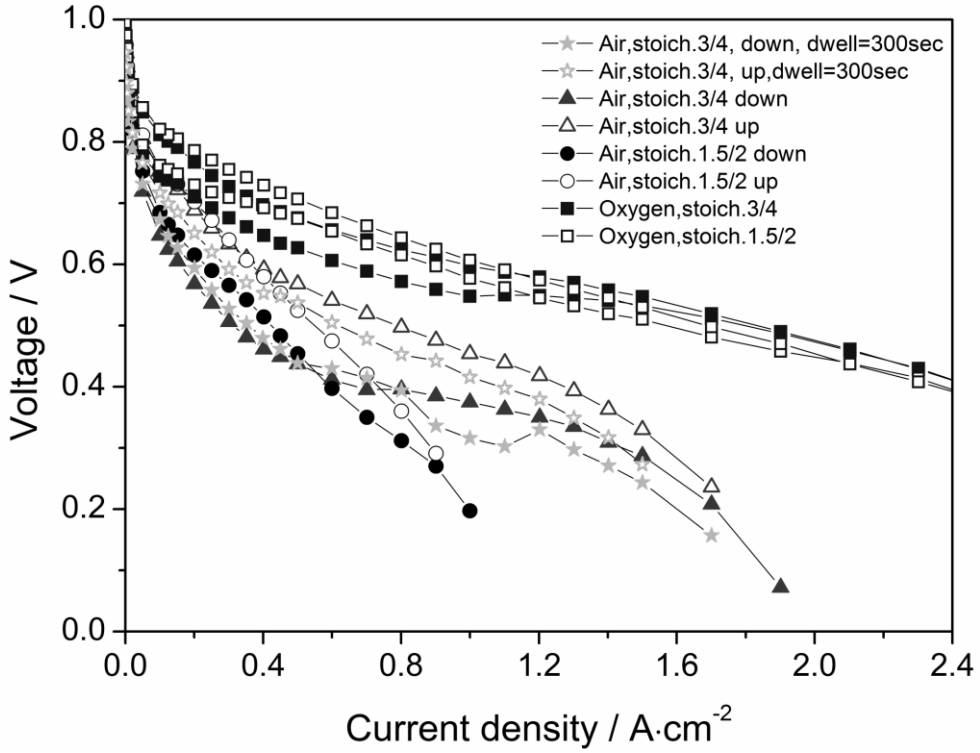

Figure 4.6 Polarization curves of the dry operation of MEA at 65 °C. Dwell time is 30 seconds in all measurements unless otherwise indicated.

The efficiency in the water removal of the CNF layer was compared with the commercial MPL coated GDL by switching the gasses supplied to the cell. In this arrangement, hydrogen was fed to the CNF grown GDL, now serving as anode. Figure 4.4 shows the gas stoichiometry now only has a minor effect on the performance and the hysteresis observed at an operating temperature of 65 °C (Figure 4.4-a) and even less at 80 °C (Figure 4.4-b), in contrast to the results shown in Figure 4.2. Comparing Figure 4.4-a and b, the performance observed with a stoichiometric ratio of 3.0||4.0 is hardly affected by the temperature change whereas at a stoichiometric ratio of 1.5||2.0, the performance increased significantly at 80 °C (Figure 4.4-b). Note that the MEA showed more stable performance when using the commercial MPL coated GDL at the cathode. The absolute performance at 80 °C is comparable with the operation of the CNF grown GDL at the cathode. However, at 65 °C, the use of the CNF grown GDL at the cathode leads to superior performance at high current density.

Cyclic voltammograms of the anode and the cathode showed that the active Pt catalyst surface areas in contact with the membrane were approximately the same, measuring 52 and 47 $m^2 \cdot g^{-1}$ for the commercial MPL coated GDL and the CNF grown GDL, respectively (Figure 4.5). The integrity of the MEA was confirmed through hydrogen cross-over measurements, reading an acceptable maximum value of 2 $mA \cdot cm^{-2}$ during the final end-of-life test. These results indicate that the distinct characteristics observed under air atmosphere are to be attributed to the influence of the GDL composition at the cathode.

Finally the fuel cell was operated using dry air and oxygen, bypassing the cathode humidifier, to re-evaluate the water removal characteristics of the CNF layer in the absence of excess liquid water. The same parameters were varied to measure the effect of gas stoichiometry, oxygen source (air or pure oxygen) and waiting time per data point (dwell time). Figure 4.6 shows that the most dominant effect was drying out of the MEA, since even the oxygen performance suffered from increased resistance and hysteresis effects. Hysteresis is caused by the liquid water, produced at the cathode locally hydrating the electrode and membrane, thus increasing its proton conductivity and lowering voltage losses. As a result, higher output voltages are observed during the up-sweep of the polarization curve as the current density is decreased from higher values (air up curves in Figure 4.6). Increasing the dwell time from 30 seconds to 300 seconds per data point reduced the described hysteresis effect as the system gets closer to equilibrium conditions. Decreasing the gas stoichiometry from 3.0||4.0 to 1.5||2.0 made the fuel cell less susceptible to the drying out effect, and hence reduced the observed hysteresis effect for both air and oxygen performance curves. The elevated stoichiometry helped MEA to achieve higher current densities in air (at 30s dwell time) on the air down curve, which was due to the retained additional product water. This gave a significantly better performance on the air up curve, despite the expected drying out effect dominating at low current densities. All these polarization curves indicate that the CNF grown GDL does not prevent the cathode catalyst layer from drying out, although it retains product water in the short term.

4.4 Concluding remarks

This chapter presents the potential benefits and risks of using a CNF layer as a MPL in PEM fuel cells without any addition of PTFE. Single cell experiments showed that when the less hydrophobic CNF layer compared to a commercial GDL was integrated at the cathode of the MEA, the catalyst layer was prone to flooding at low current density, 1.5||2.0 stoichiometry and 65 °C cell temperature. However, a remarkable performance recovery was observed at high current densities and increased gas stoichiometries of 3.0||4.0, suggesting an internal re-distribution of liquid water enabling superior power densities. This phenomenon needs to be studied in more detail, but correlates to the properties of the CNF layer, since it was not observed when operating the MEA in 'reverse' mode with a commercial reference GDL at the cathode.

Interestingly, similar absolute performance characteristics were observed for both the 'normal' and reverse' mode of operations at a cell temperature of 80 °C under air and oxygen. The same MEA operated under dry conditions suffered from 'drying out' and strong hysteresis effects were observed in the polarization curves.

Although strong arguments exist to prefer fuel cell stability over performance, the question remains how to harness this promising water transport capability of CNF grown GDL structures in addition to the well-known advantages in electrical conductivity.

References

[1] F.T. Wagner, B. Lakshmanan, M.F. Mathias, J Phys Chem Letters, 1 (2010) 2204-2219.
[2] F.A. de Bruijn, International Workshop on Advanced Material for New and Renewable Energy, AIP, Jakarta (Indonesia), 2009, pp. 3-12.
[3] F.A. de Bruijn, V.A.T. Dam, G.J.M. Janssen, Fuel Cells, 8 (2008) 3-22.
[4] S. Litster, C.R. Buie, T. Fabian, J.K. Eaton, J.G. Santiago, J Electrochem Soc, 154 (2007) B1049-B1058.
[5] Y.H. Park, J.A. Caton, Int J Hydrogen Energy, 33 (2008) 7513-7520.
[6] M.B. Ji, Z.D. Wei, Energies, 2 (2009) 1057-1106.
[7] C.J. Tseng, S.K. Lo, Energy Conversion and Management, 51 (2010) 677-684.
[8] Z.G. Qi, A. Kaufman, J Power Sources, 109 (2002) 38-46.
[9] G.J.M. Janssen, M.L.J. Overvelde, J Power Sources, 101 (2001) 117-125.
[10] J. Chen, T. Matsuura, M. Hori, J Power Sources, 131 (2004) 155-161.
[11] U. Pasaogullari, C.Y. Wang, Electrochimica Acta, 49 (2004) 4359-4369.
[12] F. Lufrano, E. Passalacqua, G. Squadrito, A. Patti, L. Giorgi, J Appl Electrochem., 29 (1999) 445-448.
[13] Z.J. Lu, M.M. Daino, C. Rath, S.G. Kandlikar, Int J Hydrogen Energy, 35 (2010) 4222-4233.
[14] G.G. Park, Y.J. Sohn, S.D. Yim, T.H. Yang, Y.G. Yoon, W.Y. Lee, K. Eguchi, C.S. Kim, J Power Sources, 163 (2006) 113-118.
[15] P.H. Maheshwari, R.B. Mathur, Electrochimica Acta, 54 (2009) 7476-7482.
[16] C.Y. Du, B.R. Wang, X.Q. Cheng, J Power Sources, 187 (2009) 505-508.
[17] G.J.M. Janssen, E.F. Sitters, A. Pfrang, J Power Sources, 191 (2009) 501-509.
[18] R. Friedmann, T. Van Nguyen, J Electrochem Soc, 157 (2010) B260-B265.

CNF grown carbon paper as a water management layer for PEM fuel cells

5

Abstract

Carbon nanofiber (CNF) grown carbon paper loaded with two different hydrophobic polymers (Polytetrafluoroethylene and polydimethylsiloxane modified polystyrene-alt-maleic anhydride) was used as a water management layer in a proton exchange membrane (PEM) fuel cell. The influences of the type and loading of the polymer, gas feed stoichiometry, PEM fuel cell operating temperature and the type of oxidant were investigated in order to determine the optimum operating conditions. The membrane electrode assemblies (MEAs) were characterized by electrochemical performance tests, cyclic voltammetry and electrochemical impedance spectroscopy. The results showed that the electrochemical performance of the CNF grown carbon papers used at the cathode part of the MEAs was strongly influenced by feed stoichiometry and polymer loading. None of the constructed MEAs surpassed the performance of the reference MEA, however, using this novel material both at the cathode and the anode as a water management layer showed a stable PEM fuel cell performance with a reduced hysteresis and an acceptable overall resistance.

5.1 Introduction

The atmospheric concentration of CO_2 has rapidly increased in the last century due to fossil fuel consumption by vehicles and heat or electricity generators [1]. The threat of this increase requires the implementation of zero emission power devices [2]. The proton exchange membrane (PEM) fuel cell is a promising power generator using hydrogen and oxygen producing only water as exhaust. The operating temperature of PEM fuel cells remains generally below 100 °C, which allows a rapid start-up. PEM fuel cells are compact and lightweight compared to other fuel cell types, increasing the power produced per unit volume of the fuel cell. These advantages make the PEM fuel cells the best candidate not only for the stationary power applications but also for automotive applications [3-6].

One drawback of operating PEM fuel cells below 100 °C is the management of water distributed within the catalyst layer and the membrane [7-10]. The necessity of membrane hydration and excess water removal from the cathode makes the water management very critical for PEM fuel cells. As explained in chapter 1, flooding (too much water formation) within the catalyst layer and drying of the perfluorosulfonic acid membrane create immediate severe problems like fuel starvation in the catalyst layer, pinholes on the membrane, and long term problems like degradation of the membrane and catalyst [11-13]. Due to the high risk of membrane degradation in dry conditions, humidified (>50%) gas feeds are preferred by the PEM fuel cell operators. In this case, however, too much water can be produced at high current density, resulting in a considerable voltage drop. The feed gas, oxygen, does not reach to the catalyst surface and subsequently the electrochemical performance is reduced. Therefore, a careful control of the water-gas balance at high current density is vital.

The introduction of a microporous layer (MPL) between the catalyst layer and the gas diffusion layer (GDL) improves the water management at high current density [9, 14-19]. The MPLs are typically a mixture of carbon black and polytetrafluoroethylene (PTFE) providing a high degree of electron conductivity and superhydrophobicity. These two properties are of crucial importance for the

PEM fuel cells, since an increase in the electric resistance results in a performance loss and a decrease in the superhydrophobicity causes a complete wetting of the MPL [8]. The carbon-PTFE mixture used in the MPLs is prone to degradation due to the weakness of the carbon black under the PEM fuel cell operating conditions.

A structured GDL as MPL can make the PEM fuel cell more resistant to the high gas and water flows at high current densities. One promising candidate for the replacement of carbon blacks in the MPL is the implementation of the carbon nanofibers (CNFs) as MPL on a GDL. The growth of CNFs on a GDL to be used as a MPL is considered a new enhancement factor in both the electronic conductivity and the gas permeability [20-22]. In the previous chapter, a CNF grown GDL was used as a MPL, for which sudden voltage losses were observed due to the wetting of the CNF layer at low stoichiometric ratios. In this chapter, CNF grown GDLs were loaded with PTFE and PDMS modified PSMA to improve the hydrophobicity of the catalyst backing layer without causing a large increase in the electric resistance. For a better evaluation of the CNF grown GDLs, commercially available catalyst coated membranes (CCMs) were used to eliminate membrane and catalyst effects.

5.2 Experimental

5.2.1 Preparation of CNF grown carbon papers

The growth of CNFs was performed via the decomposition of ethylene on a nickel catalyst. The amount of nickel deposited on the GDL (TGP-H-060, Toray carbon paper) was increased compared to the given values in chapter 3 in order to grow more CNFs and to obtain a CNF layer without large pores (larger than 1 μm on its surface). It was observed that the loading of CNFs on a single side of carbon paper should be higher than ~4.5 $mgCNF \cdot cm^{-2}$ in order to cover all the existing pores in the carbon paper. Uncovered pores result in flooding and instabilities not only at high current densities but also at low current densities as was observed in the preliminary studies. Table 5.1 lists the loadings of nickel and CNF on the

carbon paper, the required polymer loadings and the average contact angles of the polymer-CNF-carbon paper surface.

A PTFE dispersion (60 wt.%) in water was purchased from Sigma Aldrich and diluted to 5 wt.%. The CNF grown carbon paper was first oxidized with 50 vol.% nitric acid at 60 °C for an hour. Nitric acid oxidation facilitates the removal of the nickel used in the CNF growth [23, 24]. The oxidized CNF grown carbon paper was dipped into the 5 wt.% PTFE solution and then dried at 60 °C. The deposition of PTFE was repeated until reaching the desired loading of PTFE (Table 5.1) on the CNF-carbon paper. PDMS modified PSMA is an alternative material to make the CNF grown carbon paper superhydrophobic. 30 mol% of the anhydrides in PSMA copolymer is imidized by mono amine terminated PDMS (PDMS-NH_2) and PSMA30 latex is produced. Both PTFE and PSMA30 make contact angles ~135° on cotton or carbon paper [25]. However, carbon paper or cotton has a lower surface roughness compared to the CNF grown carbon paper. The contact angle measurements on PSMA30 loaded CNF grown carbon papers yielded nearly an angle of 150° with a low contact angle hysteresis.

5.2.2 Preparation of the membrane electrode assembly

To compare the GDLs with each other, the membranes and the platinum (Pt) catalyst loadings should be identical. For this purpose, catalyst coated membranes (CCMs) were purchased from Johnson Matthey Fuel Cell. The Pt catalyst loadings were 0.2 $mg \cdot cm^{-2}$ at the anode and 0.6 $mg \cdot cm^{-2}$ at the cathode. A product of SIGRACET, GDL 25 BC, was selected as a reference MPL [26]. The sizes of the CNF grown carbon papers and GDL 25 BC were reduced to a circular size of 32 mm and then placed on current collector plates which have serpentine flow fields. A Teflon gasket of 150 µm thickness was used on the flow fields as shown in Figure 5.1-a for sealing. One of the carbon paper was inserted on top of the Teflon gasket and subsequently the CCM was attached and then, the other carbon paper was placed on the CCM. Finally, another current collector with a Teflon gasket was attached. The CNF grown carbon papers were sandwiched in the configurations

presented in Table 5.2 in order to obtain information on their performance under fuel cell conditions.

Table 5.1 Properties of the CNF grown carbon paper.

CNF carbon paper	$Ni(OH)_2$ loading	CNF loading	PTFE loading *	PSMA30 loading	Contact Angle***
(#)	$mg \cdot cm^{-2}$	$mg \cdot cm^{-2}$	wt.%	wt.%	°
CNF1	0.55	5.8	11.1	-	148±3
CNF2	0.54	5.5	-	5.1	146±3
CNF3	0.50	4.7	8.9	-	145±4
CNF4	0.52	5.6	-	10.0**	147±2
CNF5	0.58	5.8	19.2	-	145±3
CNF6	0.46	4.5	9.3	-	146±4
CNF7	0.62	4.6	6.9	-	146±3
CNF8	0.53	5.0	-	11.5**	146±3
CNF9	0.60	5.1	-	10.3**	144±3

* **All the PTFE loaded samples were annealed at 350 °C for 1 hour in N_2.**

** **A crosslinker (adipic dihydrazide) was used to make PSMA30 water resistant.**

*** **Contact angles are the averages of measurements at five different locations over 13.2 cm^2 area of the produced CNF grown carbon paper.**

5.2.3 Cell operation and electrochemical characterizations

The MEAs were installed in 5W single cell test stations located at the NedStack Fuel Cell Company in Arnhem, The Netherlands. The flow field consists of a single serpentine structure with channel dimensions of 1x1mm cross/section at 1 mm spacing (Figure 5.1-a). The pneumatic cell compression used in this study was 5 bar. A heating bath was used to heat the water circulating around the MEA and the humidification compartment (Figure 5.1-b). Leak tests were carried out before starting the electrochemical measurements. Before the leak test, the anode flow was set at 20 $ml \cdot min^{-1}$ and the cathode flow was set at 0. This creates a slight pressure difference on both sides of the membrane. Leakage occurring across the

membrane reduces the open circuit voltage (OCV) owing to the hydrogen crossover. If a membrane does not contain any pinholes and does not have any gas leakage, the voltage drop is expected to be linear.

Table 5.2 Configurations of the MEAs used in the measurements.

MEA #	Cathode	Anode
MEA1	GDL 25 BC	GDL 25 BC
MEA2	**CNF1**	GDL 25 BC
MEA3	**CNF2**	GDL 25 BC
MEA4	GDL 25 BC	**CNF3**
MEA5	**CNF4**	GDL 25 BC
MEA6	**CNF5**	GDL 25 BC
MEA7	**CNF6**	**CNF7**
MEA8	**CNF8**	**CNF9**

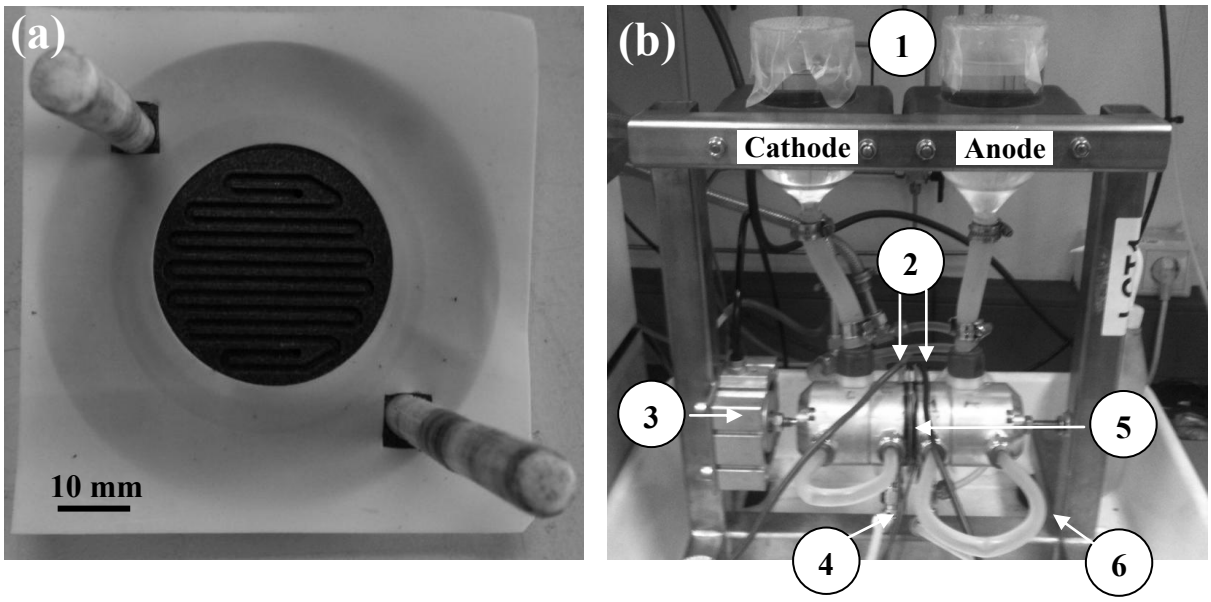

Figure 5.1 a) Teflon gasket with a 32 mm circular hole inserted on a serpentine flow field. b) Single cell fuel cell test station. (1) Cathode and anode humidification vessels. (2) Current load connections. (3) Pneumatic cell compression (Applied pressure is 5 bar). (4) Voltage reading cables. (5) Membrane electrode assembly. (6) Heating elements. An external heater circulates water internally through indicated transparent hoses.

Table 5.3 The measurement sequence of the MEAs depicted in Table 5.2.

Order	Measurement
1	Voltage-current data was obtained by increasing (Air down) the current density at **65 °C** from 0 to the highest current density recorded. The waiting time per point was 2 minutes.
2	Voltage-current data was obtained by decreasing (Air up) the current density at **65 °C** from the highest current density recorded to 0.
3	In the cathode part, air was replaced by oxygen and then the voltage-current data was recorded by increasing the current density at **65 °C** from 0 to 1800 $mA \cdot cm^{-2}$. Since flooding was not effective in oxygen operation, the cell can go up to1800 $mA \cdot cm^{-2}$.
4	The stability test of the fuel cell was performed at **65 °C** and 1150 $mA \cdot cm^{-2}$.
5	Voltage-current data by increasing (Air down) the current density at **80 °C** from 0 to highest current density recorded. The waiting time per point was 2 minutes.
6	Voltage-current data was obtained by decreasing (Air up) the current density at **80 °C** from the highest current density recorded to 0.
7	In the cathode part, air was replaced by oxygen and then the voltage-current data was recorded by increasing the current density at **80 °C** from 0 to 1800 $mA \cdot cm^{-2}$ since flooding is not effective in oxygen run.
8	The stability test of the fuel cell was performed at **65 °C** and 1150 $mA \cdot cm^{-2}$.
9	The impedances of the MEAs were measured at **65 °C** at the current densities of 30, 600, 925, 1150 $mA \cdot cm^{-2}$.
10	Cyclic Voltammograms of the cathode were measured at **65 °C** to determine the electrochemical surface area of the Pt.
11	The cell was operated at high stoichiometry of 3.0 for the anode and 4.0 for the cathode at **65 °C.**

Conditioning of the MEAs is required for the activation of the Pt electrocatalyst, the removal of the dust and the humidification of the MEA. Since the MEAs are compared with each other, they should have the same conditioning and measurement history. The MEAs were first humidified at either 65 or 80 °C, and conditioned at the constant voltage mode operating at 0.2 V for 10 minutes with stoichiometric ratios of 2.0 for the anode and 2.0 for the cathode. The cell

voltage was allowed to increase to 0.8 V for 2 minutes and then decreased back to 0.2 V. The current density at the same voltage is expected to increase at the end of each conditioning cycle. After conditioning, the cell was brought to its operating conditions; stoichiometries 1.25 for the anode and 2.0 for the cathode, and the minimum gas flow rates 20 $ml \cdot min^{-1}$ for the anode and 40 $ml \cdot min^{-1}$ for the cathode. The highest current density of the MEA at 0.2 V is recorded by increasing by 50 $mA \cdot cm^{-2}$ with 10 seconds intervals. The operation of a MEA below 0.2 V may accelerate Pt corrosion and this may reduce the performance of the cell which results in an improper comparison among the MEAs. The measurement program is modified with the highest current density at 0.2 V and the measurements at the lowered stoichiometries were started automatically with a Labview program. In these measurements, voltage was recorded against current density. The measurement steps in Table 5.3 were performed for each MEA shown in Table 5.2.

Polarization tests were conducted starting from the OCV and recording the voltage for 2 minutes while sweeping the current load up to a preset current density (Table 5.3), before reversing the sequence and stepping back to OCV. MEA diagnostic measurements were conducted on the Autolab potentiostat and Booster. The measurements consisted of Electrochemical Impedance Spectroscopy (EIS, 100kHz-1Hz, 5mV ampl., and Cyclic Voltammetry (CV, 10 scans, 0.06 – 1 V, scan rate of 50 $mV \cdot s^{-1}$). CV was used to determine the electrochemical surface area from the hydrogen underpotential deposition (H_{upd}) peaks. CV measurements were only carried out for the cathode due to the absence of a hydrogen connection at the cathode. Therefore, the MEA cannot be reversely operated in the setup. An Autolab PGSTAT302 with FRA2 module in combination with the frequency response analyzer (FRA) software was used for the in situ EIS measurements. It was reported that two electrode configuration with the anode as a reference electrode results in a negligible difference compared to the reversible hydrogen electrode used in the ex-situ measurements [27]. EIS was performed under air operation at 65 °C at four different fixed current densities; 30, 600, 925 and 1150 $mA \cdot cm^{-2}$ to identify the kinetic and mass transport resistances.

5.3 Results and discussion

5.3.1 Leak tests and conditioning of the MEAs

The results of the leak tests are presented in the appendix of this chapter in Figure 5.A.1. All MEAs have low hydrogen crossovers and have voltages higher than 0.2 V even after 120 seconds and thereby, all the MEAs passed the comparison limitations for the electrochemical performance measurements. The Pt catalyst should be activated or conditioned before starting electrochemical performance tests. The results of the conditioning of all MEAs are elaborately described in Figures 5.A.2 and 5.A.3.

5.3.2 Polarization curves

Impact of operating temperature, 65 and 80 °C, on the electrochemical performance

The effect of CNF decoration on the carbon papers is investigated using the same catalyst coated membranes (CCMs) at two different operating temperatures with fully humidified gas feeds. Figure 5.2 shows how the operating temperature influences the electrochemical performance of the MEAs. The stoichiometric ratio of the feeds is kept constant with respect to dry gas content and thereby, when the PEM fuel cell operating temperature increases, the water vapor content of the gas streams also increases. The higher water vapor content boosts the total gas flow rate and thereby the gas velocities within the GDL. Consequently, an increased gas velocity reduces flooding. In Figure 5.2, it is observed that the operating temperature of 80 °C has a sufficient gas velocity to open enough gas channels for all MEAs compared to the operating temperature of 65 °C. At higher temperature, the membrane water content and water diffusivity increase making the membrane homogeneously hydrated [28]. Increase in operating temperature enhances the diffusivity of oxygen, however, its concentration decreases due to the increased water vapor content. Therefore, at a higher operating temperature with fully humidified gases, the overall electrochemical performance of the MEAs decreases

compared to the performances obtained at a lower operating temperature, especially at high current densities. The effect of temperature on the PEM fuel cell performance using a GDL without MPL was investigated and it was shown that the increase in operating temperature enhances the fuel cell performance [29] which is a contradiction with the present work and a publication on the modeling of the liquid water transport within the GDLs [28].

Considering the influence of temperature and the diffusivity of oxygen on flooding, all MEAs showed similar characteristics. At high current densities, higher operating temperature reduced the overall performance, however, the flooding occurred in the Ohmic region disappeared. The performance of MEA2 (PTFE-CNF applied at the cathode) and MEA7 (PTFE-CNF applied on both sides of the MEA) at both operating temperatures are comparable with each other with an acceptable flooding in the Ohmic region. Nevertheless, PTFE loaded CNF grown carbon papers applied at the cathode and on both sides of the MEA are advantageous without a considerable performance loss at this temperature range compared to the reference MEA (MEA1). 19.2 wt.% PTFE loaded CNF grown layer applied at the cathode of MEA6 reduced the cell performance at a higher operating temperature. An increased PTFE loading reduced the hydrophilic pathways within the CNF layer and increased the resistance to the water flow. Consequently, the back diffusion rate (water transport from cathode to anode) increased, causing a negative effect on the Ohmic resistance due to the lowered proton transfer. Popov et al. determined that 20 wt.% PTFE loaded MPL showed an improved performance compared to lower and higher PTFE loaded GDLs at an operating temperature of 75 °C [30, 31]. Ramasamy et al. showed that the capillary pressure increased with the increased PTFE loading on the GDLs [32]. Therefore, a higher capillary pressure decreases the water retention due to the reduction in the number of the hydrophilic pathways. There is an optimum value for the PTFE loading supporting the conclusion drawn here. In the present work, CNF grown GDLs have a considerably higher surface roughness increasing the resistance to water flow with a lower PTFE content compared to the PTFE loadings in literature.

Another polymer, PSMA30, was used in MEA3, MEA5 and MEA8 instead of PTFE. As long as PSMA30 was not crosslinked on the CNFs, flooding caused large instabilities at 65 °C. However, at high current densities, owing to the increased total gas flow, MEA3 achieved much higher current densities than the reference MEA at the same operating voltage. Operating the fuel cell at 80 °C reduced the cell performance of MEA3 to the performance of MEA1 at the same operating temperature (Figure 5.3-a). When the loading of PSMA30 increased to 10 wt.% and PSMA30 was crosslinked (MEA5 in Figure 5.3-b), the flooding effect in the Ohmic region reduced compared to MEA3. However the increase in the loading of PSMA30 reduced the fuel cell performance at 80 °C compared to MEA1. Using PSMA30 on both sides of the MEA (MEA8) enhanced fuel cell performance further at 65 °C keeping the performance same with MEA5 at 80 °C.

Effect of the flooding on hysteresis

Polarization curves can show hysteresis while sweeping the current load between OCV and preset current density in both directions [33]. The curves represented as “air down” refer to the voltage-current density data obtained when the current density set to higher values starting from OCV and “air up” refers to the voltage data obtained by setting the current density values to the lower values till reaching the OCV. In this way, the hysteresis was measured for each MEA at both operating temperatures. One would expect that the cathode side of the MEA is flooding if the air up curve is at a higher potential than the potential of the air down curve at the same current density. Stepping back from a high current density to low current density in a flooding cathode would suddenly reduce the required amount of oxygen on the Pt catalyst, and thereby mass transport limitations of oxygen should no longer be a problem at that instant. Higher voltages and thereby a better performance can be obtained. However, after a sufficient waiting period, the system will balance itself, and gradually, air up and air down curves will reach to the same operating voltage.

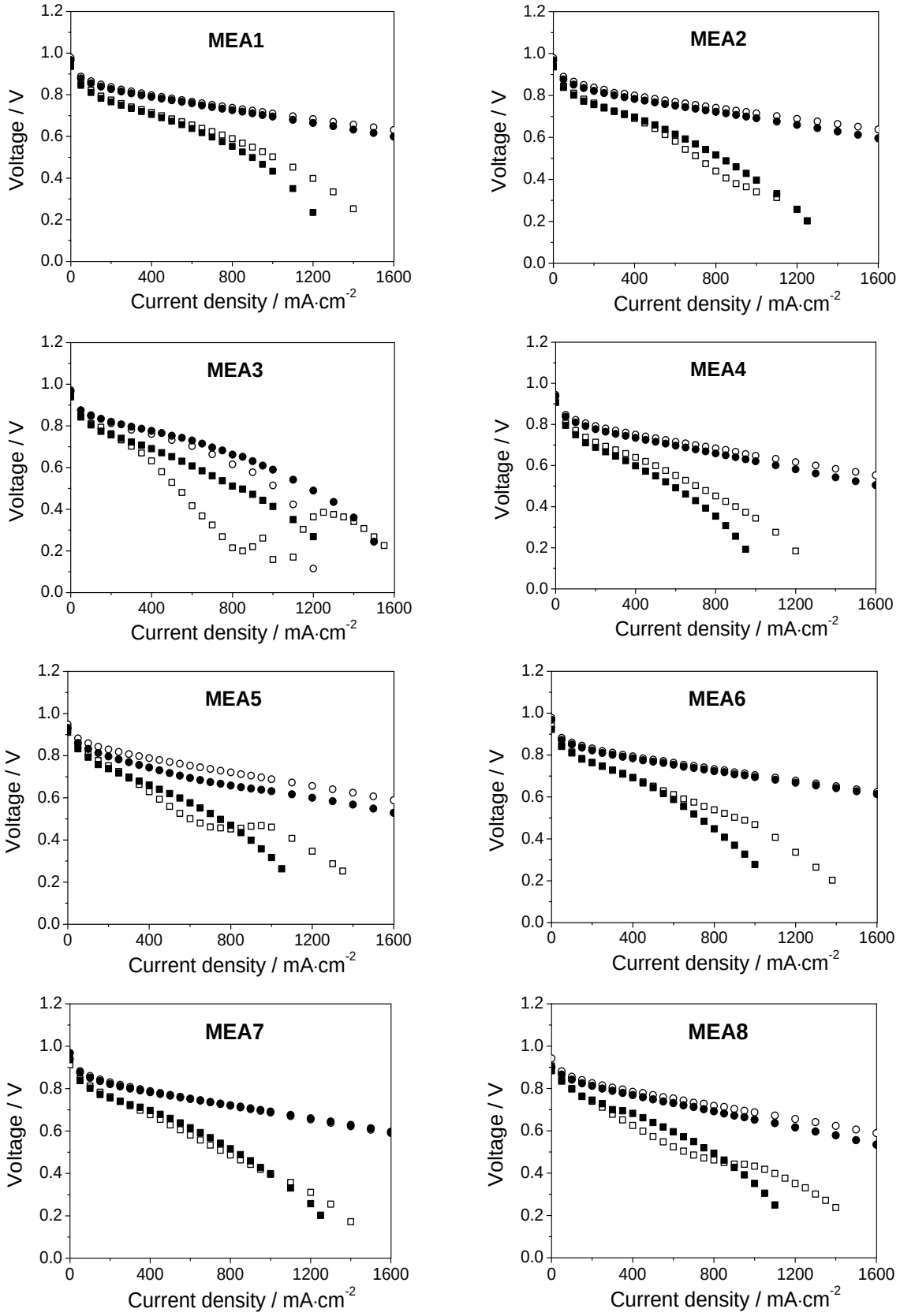

Figure 5.2 Voltage current density diagrams of MEA1, MEA2, MEA3, MEA4, MEA5, MEA6, MEA7, MEA8 at the operating temperatures of 65 and 80 °C. The symbols are identified as: ○ Oxygen at 65 °C, ● Oxygen at 80 °C, □ Air down at 65 °C, ■ Air down at 80 °C.

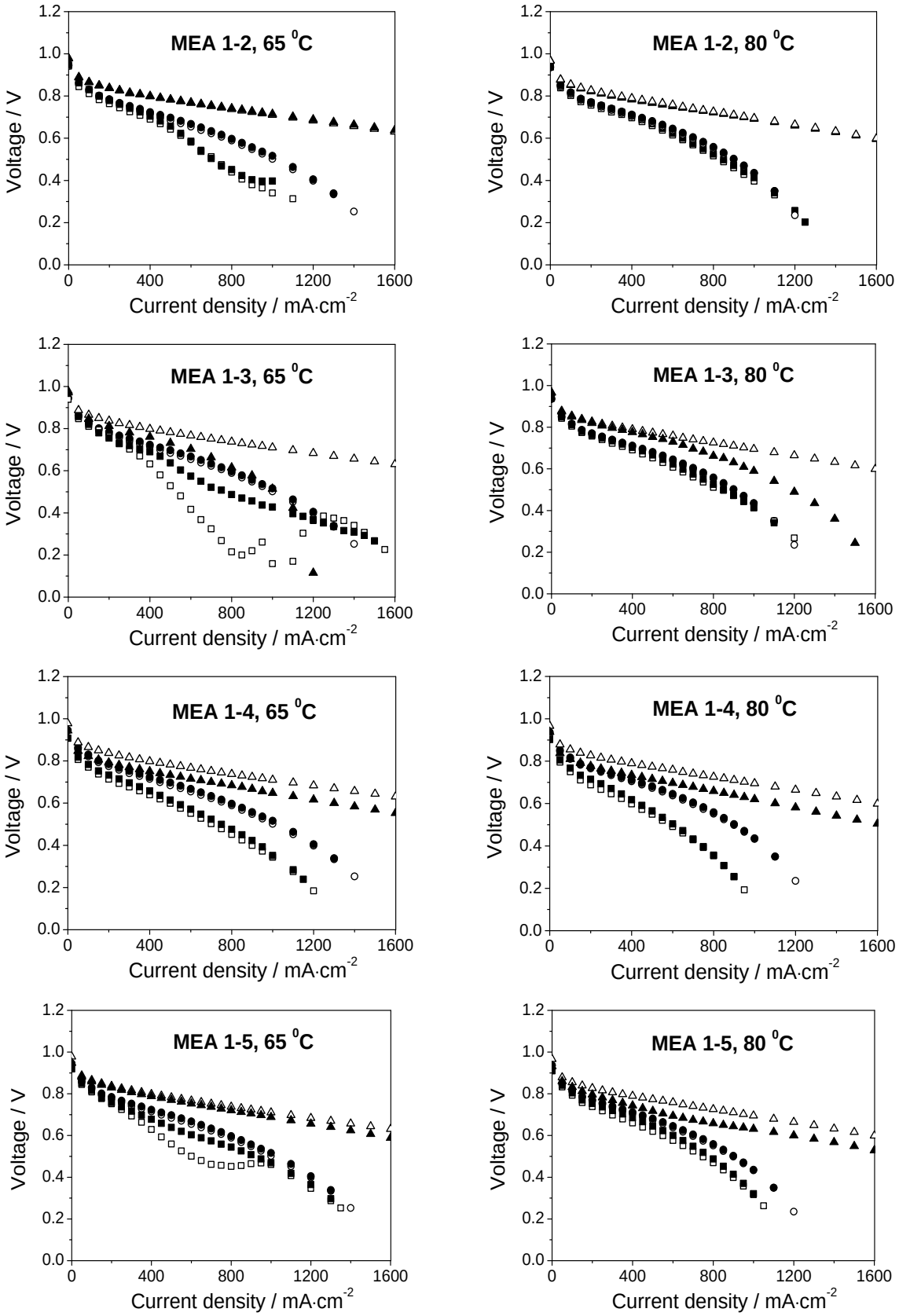

Figure 5.3-a Comparison of the polarization curve of MEA1 (reference) with the polarization curves of MEA2, MEA3, MEA4 and MEA5 at 65 and 80 °C. The symbols are identified as: ○ MEA1 Air Down, ● MEA1 Air Up, □ MEAX Air Down, ■ MEAX Air Up, Δ Oxygen MEA-1, ▲ Oxygen MEAX where X represents 2, 3, 4 and 5.

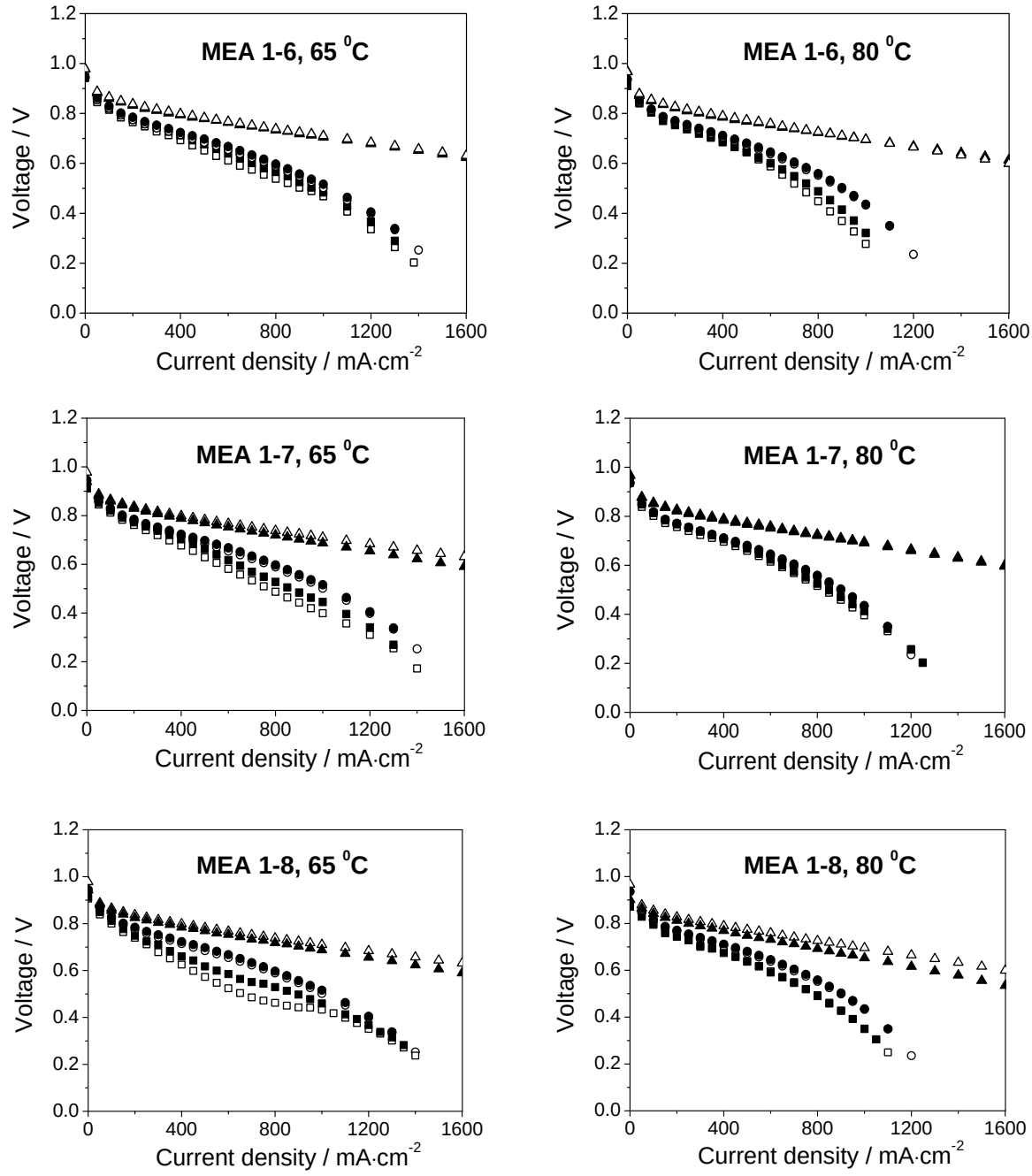

Figure 5.3-b Comparison of the polarization curve of MEA1 (reference) with the polarization curves of MEA6, MEA7 and MEA8 at 65 and 80 °C. The symbols are identified as: ○ MEA1 Air Down, ● MEA1 Air Up, □ MEAY Air Down, ■ MEAY Air Up, Δ Oxygen MEA-1, ▲ Oxygen MEAY where Y represents 6, 7, or 8.

MEA1 showed no hysteresis at both operating temperatures whereas MEA2 showed a slight hysteresis at high current density at 65 °C (Figure 5.3-a). Either an increase in the PTFE loading on CNFs (MEA6) or using the PTFE-CNF-carbon paper on both sides (MEA7) removed the effect of the observed hysteresis indicating a better water management in the Ohmic region. Using PTFE-CNF-

carbon paper at the anode of MEA4 did not result in any hysteresis at both operating temperatures. Compared to the reference MEA, MEA4 showed a poor performance indicating a catalyst utilization problem rather than flooding which will also be confirmed by the cyclic voltammograms. PSMA30 loaded CNF grown carbon papers caused flooding in the Ohmic region at 65 °C. However, at 80 °C, this effect was either reduced or disappeared. The hysteresis of MEA3 at 65 °C was very large indicating an evidence of strong flooding.

Source of the cathode feed: Air and pure oxygen

The source of the cathode feed can be used to describe the influence of water management in MEAs. The concentration of oxygen in air is five times lower than in pure oxygen, which in turn reduces the concentration of oxygen on the catalyst surface [33]. The electrochemical reaction of oxygen on the catalyst decreases the oxygen concentration while increasing the nitrogen concentration. Therefore, oxygen in air should diffuse to reach to the catalyst surface through highly concentrated nitrogen environment. The mass transport of oxygen is therefore governed by diffusion limitations at low oxygen fractions in the cathode feed [34]. When pure oxygen is used as cathode feed, mass transport is limited by convection rather than diffusion. Convection is driven by the oxygen concentration difference between the catalyst surface and gas feed. While no other effects present in the PEM fuel cell, there should be a nearly constant difference in between the plots of oxygen and air operations at any current density. At high current densities, owing to the increased rate of water formation within the catalyst layer, flooding starts to limit the electrochemical performance due to the reduction in the diffusion rate of oxygen in liquid water.

Figures 5.2, 5.3, and 5.4 show the influence of the oxidant on the polarization curves. At any current density for all MEAs except MEA3, oxygen operation results in a better performance compared to the air operation. MEA3 showed an even lower performance compared to the air operation at 65 °C (Figure 5.2). The lower performance is due to the flooding occurring at high current

densities decreasing the oxygen diffusion to the catalyst layer. Owing to the decrease in flooding, operating the fuel cell at a higher temperature increased the electrochemical performance at high current densities. The air performance of MEA3 at 65 °C is the same as oxygen performance at 80 °C at the high current density region. There is a slight performance loss at the high current density region between 65 and 80 °C for oxygen plots of MEA4, MEA5, MEA6, MEA7 and MEA8 due to a decrease in the mass transport of oxygen at a higher operating temperature.

Influence of stoichiometry

The oxygen and hydrogen stoichiometries have a large influence on the performance and degradation of the PEM fuel cells. If a PEM fuel cell is operated at a stoichiometric ratio of 1 for the anode, all hydrogen should be consumed causing a local fuel starvation and therefore degradation of the catalyst. On the other hand, using excess hydrogen is a loss of fuel increasing the cost of operation. Therefore, PEM fuel cells are mostly operated at the stoichiometric ratios in between 1 and 1.5 for the anode. Although air is not a cost issue, a lower air stoichiometry at the cathode (less than 1.2) results in a heterogeneous current distribution owing to the concentration inhomogeneity of oxygen [35]. A lower stoichiometry applied at both anode and cathode decreases the total gas flow rate which in turn decreases the gas velocities. Lower gas velocities result in a lower electrochemical performance since condensed water within the GDL causes flooding and thereby, reduces the diffusion of oxygen.

The effect of gas flow on the electrochemical performance was measured at a fuel cell operating temperature of 65 °C for all MEAs (Figure 5.4) except for MEA1, since MEA1 did not show any difference on stoichiometry change. The measurements were performed at a higher stoichiometry, 3 for the anode and 4 for the cathode. The obtained data is compared with the data obtained for the stoichiometric ratios of 1.25 for the anode and of 2.0 for the cathode. A higher stoichiometry provides not only a higher amount of reactants to the catalyst surface

but also increases the total gas flow rate, which increases the force applied on liquid water accumulated within the GDLs. As shown in Figure 5.4, the electrochemical performance of MEA2 and MEA3 at high current densities improved by the increase in the stoichiometric ratios. However, the stoichiometry did not influence the electrochemical performances of MEA4, MEA5, MEA6 and MEA8 at high current densities. The electrochemical performance of MEA7 even reduced with the increased gas stoichiometry indicating a drying at either cathode or anode side of the MEA.

MEA stability

The lower operating temperature, 65 °C, generally causes instabilities in the operating voltage since the water vapor capacity is lower compared to the operating temperature of 80 °C and this influences the oxygen diffusion to a large extent. Stability measurements were performed at 65 and 80 °C for 15 min and shown in Figure 5.5. MEA1 was rather stable during 15 minutes of continuous operation at 65 °C while only 20 mV was lost at 80 °C. MEA2 did not show any fluctuations at both operating temperatures. The stability test of MEA3 at 80 °C showed fluctuations due to the flooding, however, when the accumulated water was expelled from the GDL, it reached its stable operating voltage. The same behavior was observed for MEA4. MEA4 showed a fluctuation pattern with a two minute period due to an inhomogeneous PTFE loading on the CNFs. The stability of MEA5 was improved compared to MEA3 due to an increase in the loading of PSMA30 and crosslinking of the polymer on CNFs. MEA6 and MEA7 were as stable as MEA2 proving that the use of PTFE on CNFs did not result in stability problems. Finally, MEA8 showed no fluctuations in the stability measurements at both operating temperatures; however, the performance was either increasing (65 °C) or decreasing (80 °C) to reach the equilibrium voltage. This is an indication of the reorganization of the hydrophilic pathways in the GDL.

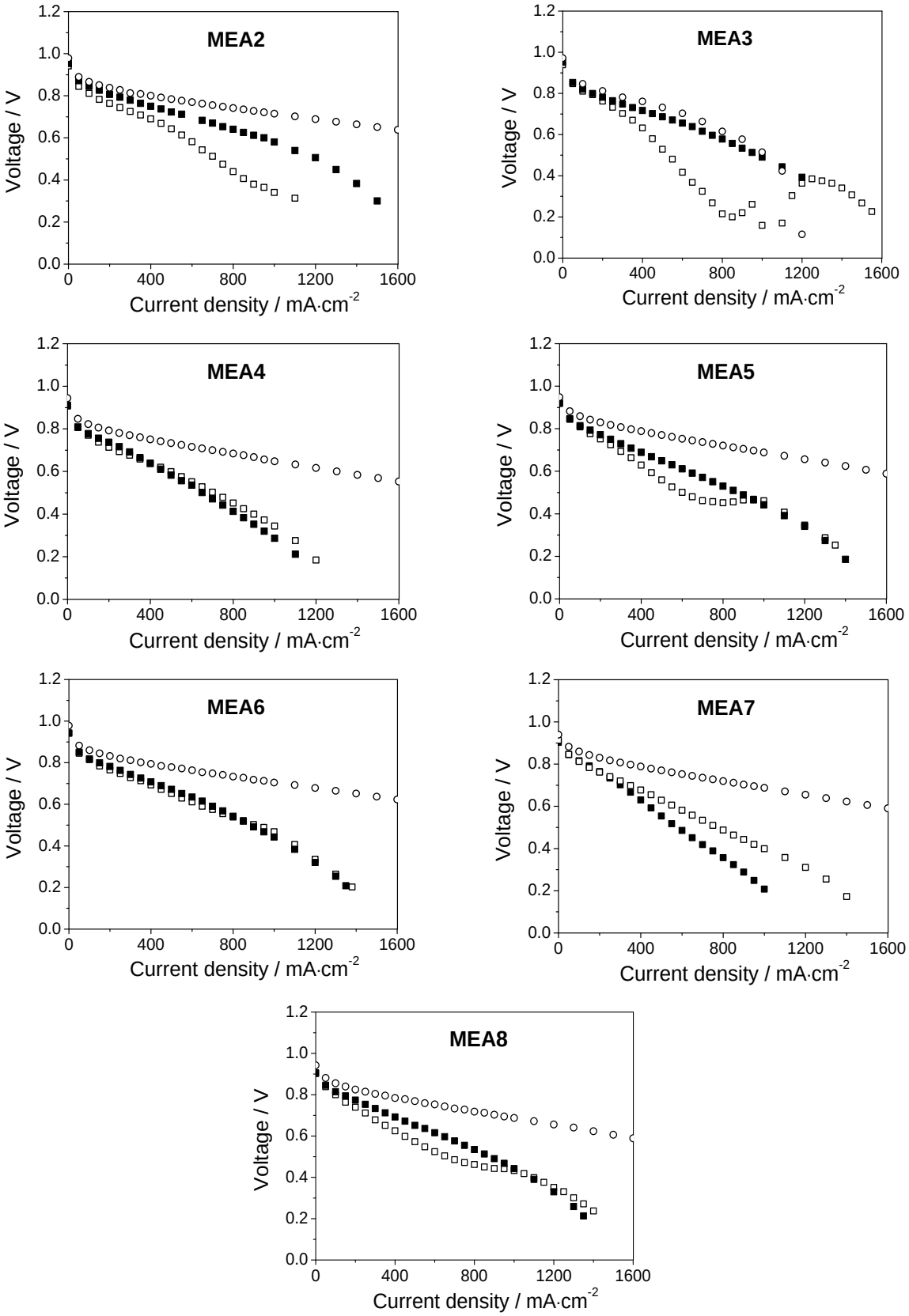

Figure 5.4 The stoichiometry effect on the PEM fuel cell performance. The data presented in these plots are plotted only for Air down operation with its oxygen operation at the stoichiometric ratios of 1.25 for anode and 2.0 for the cathode. The symbols are identified as the following: □ Air down: stoichiometry 1.25||2.0 at 65 °C, ■ Air down: stoichiometry 3.0||4.0 at 65 °C, ○ Oxygen: stoichiometry 1.25||2.0 at 65 °C.

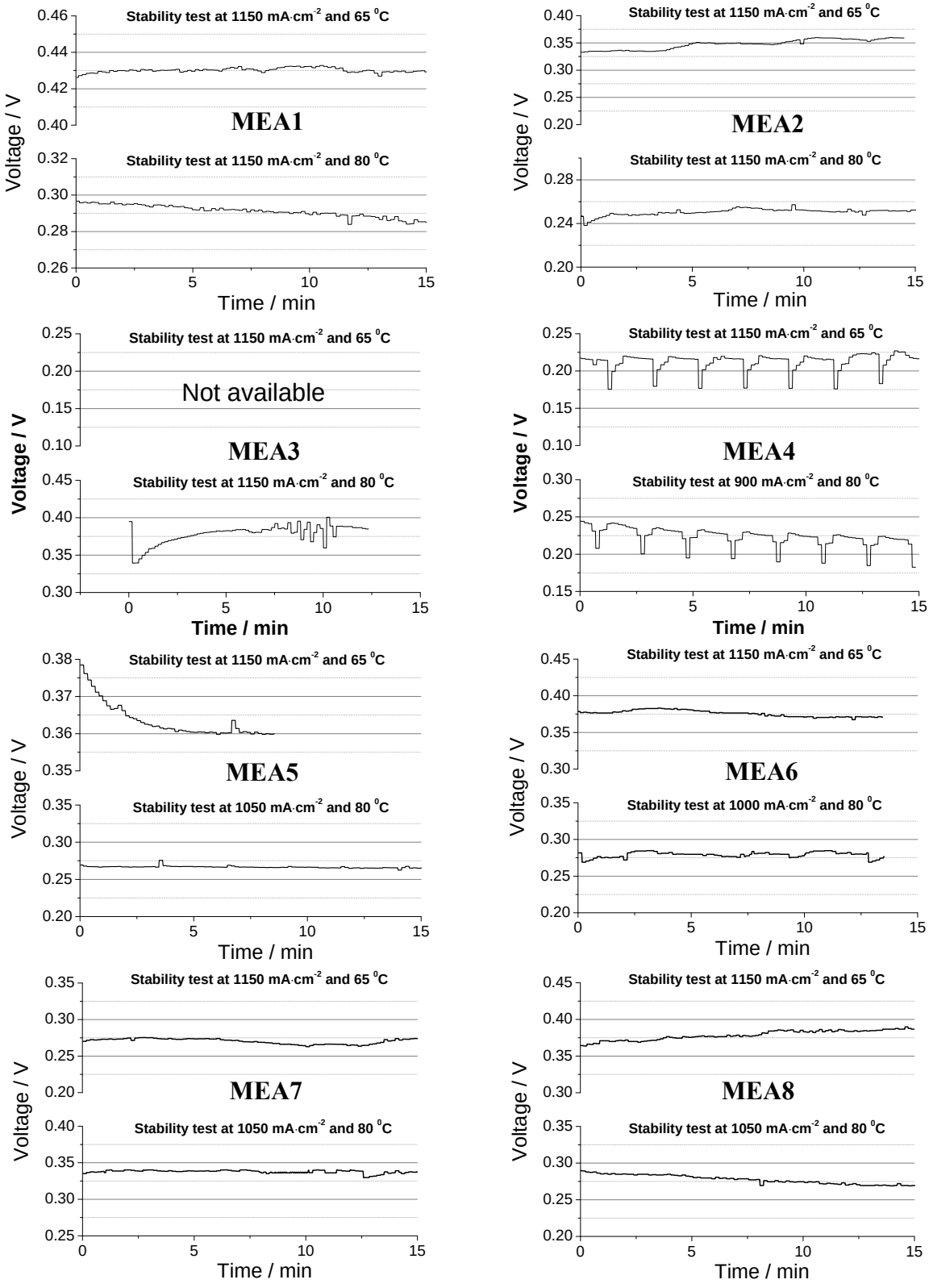

Figure 5.5 Stability tests of MEA1, MEA2, MEA3, MEA4, MEA5, MEA6, MEA7 and MEA8 at 65 and 80 °C. Stoichiometries were 1.25 for the anode and 2.0 for the cathode. Stability test of MEA3 at 65°C was not measurable due to the large voltage fluctuations at 1150 mA·cm^{-2}.

5.3.3 Cyclic voltammetry

In general, cyclic voltammetry refers to the potential sweep in between low and high potential values and records the current density during these cycles. The current density values are plotted against the voltage giving the cyclic voltammogram (Figure 5.6). Cyclic voltammograms give information about surface reactions occurring on the working electrode and the change of state of the double layer at the electrode-electrolyte interface. When the sweep rate increases, the capacitive charge contribution is relatively small compared to the charge contribution of the surface reaction [36]. Therefore, in this study, sweep rate is selected as 50 $mV \cdot s^{-1}$ where the double layer capacitive charge contribution almost disappears. Cyclic voltammogram plots of all MEAs are given in Figure 5.6 with their electrochemical surface area (ESA) values calculated from the region of H_{upd}, assuming one to one adsorption of hydrogen atoms on Pt atoms.

ESA is calculated as [37-41]: $$ESA = \frac{q_{Pt}}{\beta \times L} \times 1000$$

where q_{Pt} is the total charge density obtained by integrating the area under the H_{upd} peaks in $C \cdot cm^{-2}_{electrode}$, β is the charge required to reduce a monolayer of hydrogen atoms on Pt given as 2.1 $C \cdot m^{-2}_{pt}$, L is the Pt loading at the cathode side of the CCM given as 0.6 $mg_{pt} \cdot cm^{-2}_{electrode}$ from the manufacturer, and thereby, ESA is in $m^2_{pt} \cdot g_{pt}^{-1}$.

In Figure 5.6, it can be seen that the ESA of MEA4 is one fourth of the others, indicating a catalyst utilization problem appeared in the conditioning cycles and performance measurements. The ESA values of the other MEAs are similar, thereby, the electrochemical performance tests of these MEAs can be comparable. The ESA values are only given for the Pt catalyst deposited on the cathode side of the CCMs since the setup did not allow the operation of the MEA in the reverse mode.

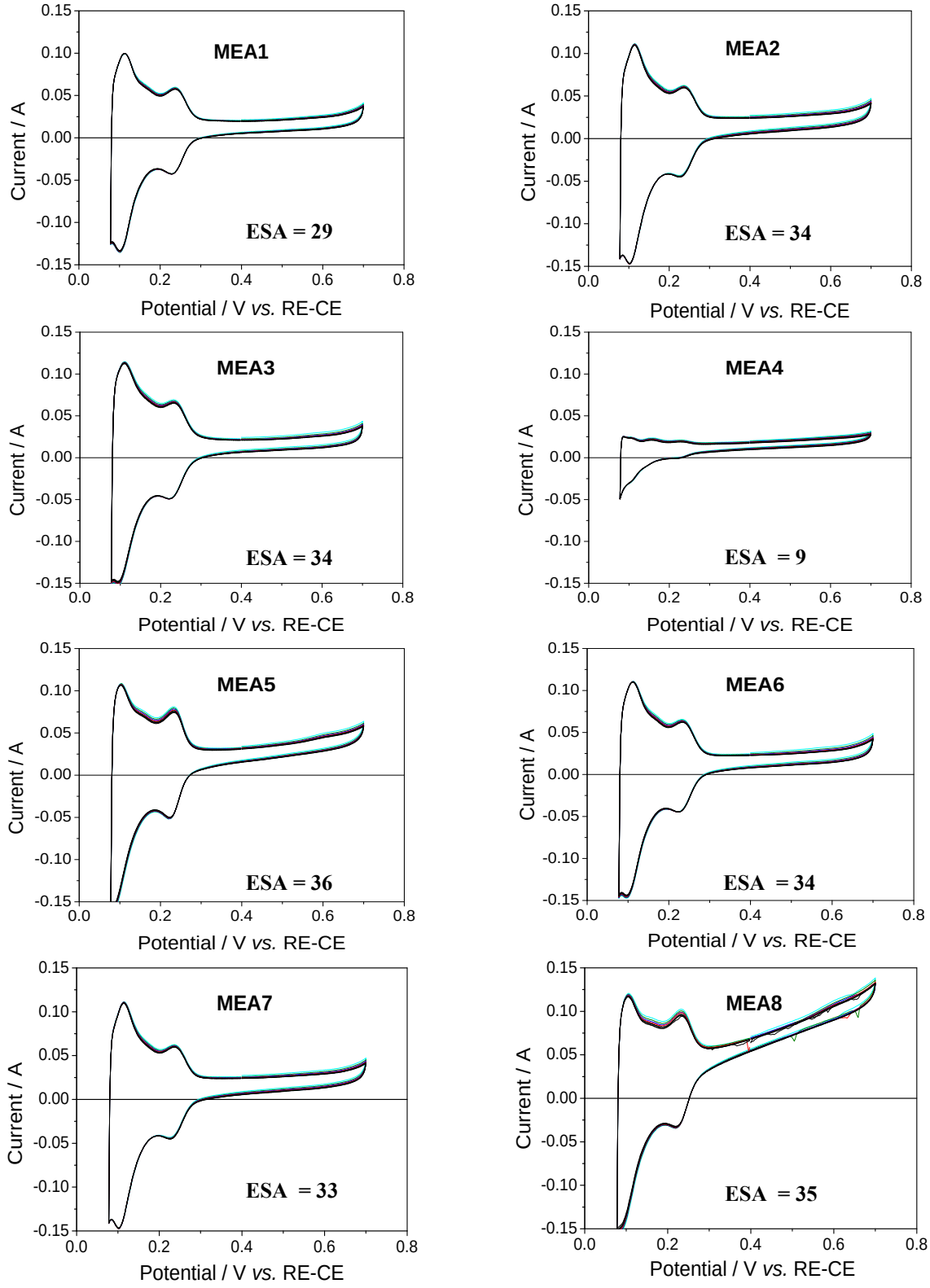

Figure 5.6 Cyclic voltammograms of the cathode part of the MEA. The measurement was done under nitrogen flow (10 ml·min^{-1}) at the cathode and hydrogen flow (10 ml·min^{-1}) at the anode part of the corresponding MEA. Ten subsequent scans were taken and the first two scans are not represented in the figures. The area under the hydrogen adsorption peaks in between 0.1 and 0.3 V of the last scan was calculated. The scan rate was 50 mV·s^{-1} and the electrode area was 8 cm^2. RE-CE represents the reference electrode and the counter electrode.

5.3.4 Electrochemical impedance spectroscopy

The impedance can be defined as the ability of a system to hinder the flow of electrons. Quantitatively, it is the proportion of the applied voltage to the current in an alternating current (AC) circuit including the phase difference of the applied voltage and current. Electrochemical Impedance Spectroscopy (EIS) is a powerful diagnostic tool for fuel cells to characterize poisoning of the electrocatalyst, proton conductivity of membrane, effect of the operating conditions and the performance of the fuel cell stacks [42, 43]. The EIS graphs are represented generally in Bode and Nyquist plots where the Bode plot shows the frequency (on the x-axis) dependence on the amplitude and phase angle of the impedance (y-axis), and the Nyquist plot relates the imaginary impedance (y-axis) with the real component of the impedance (x-axis). The Nyquist plot has the advantage of showing unique arcs providing the governing mechanism of the corresponding limitation. A typical Nyquist impedance plot of a PEM fuel cell is schematically shown in Figure 5.7. The first arc on the left hand side of the diagram is called as "high frequency arc" where kinetic resistance dominates. The second arc is called as "low frequency arc" and describes the mass transport limitation. The intercept of the high frequency arc with the real axis is the membrane resistance [22] whereas the overall resistance is the intercept of the low frequency arc with the real axis [44].

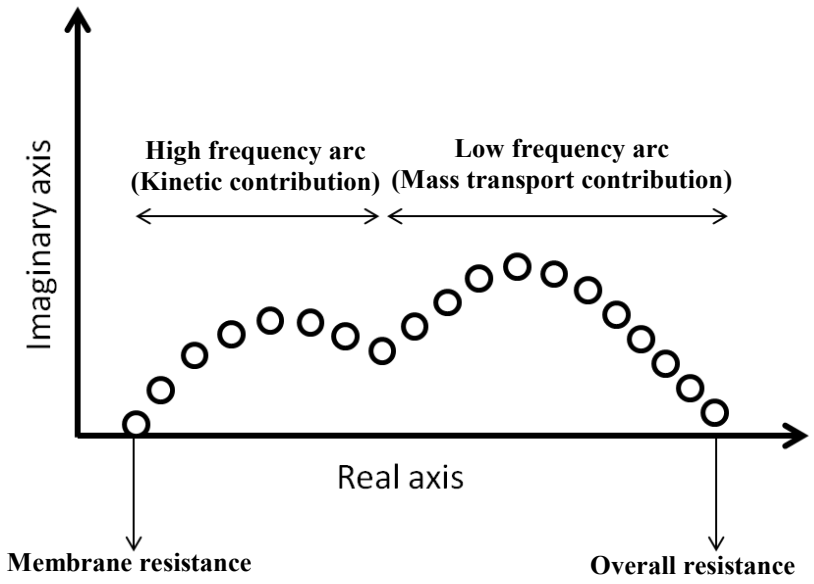

Figure 5.7 Schematic of a typical Nyquist plot of a PEM fuel cell.

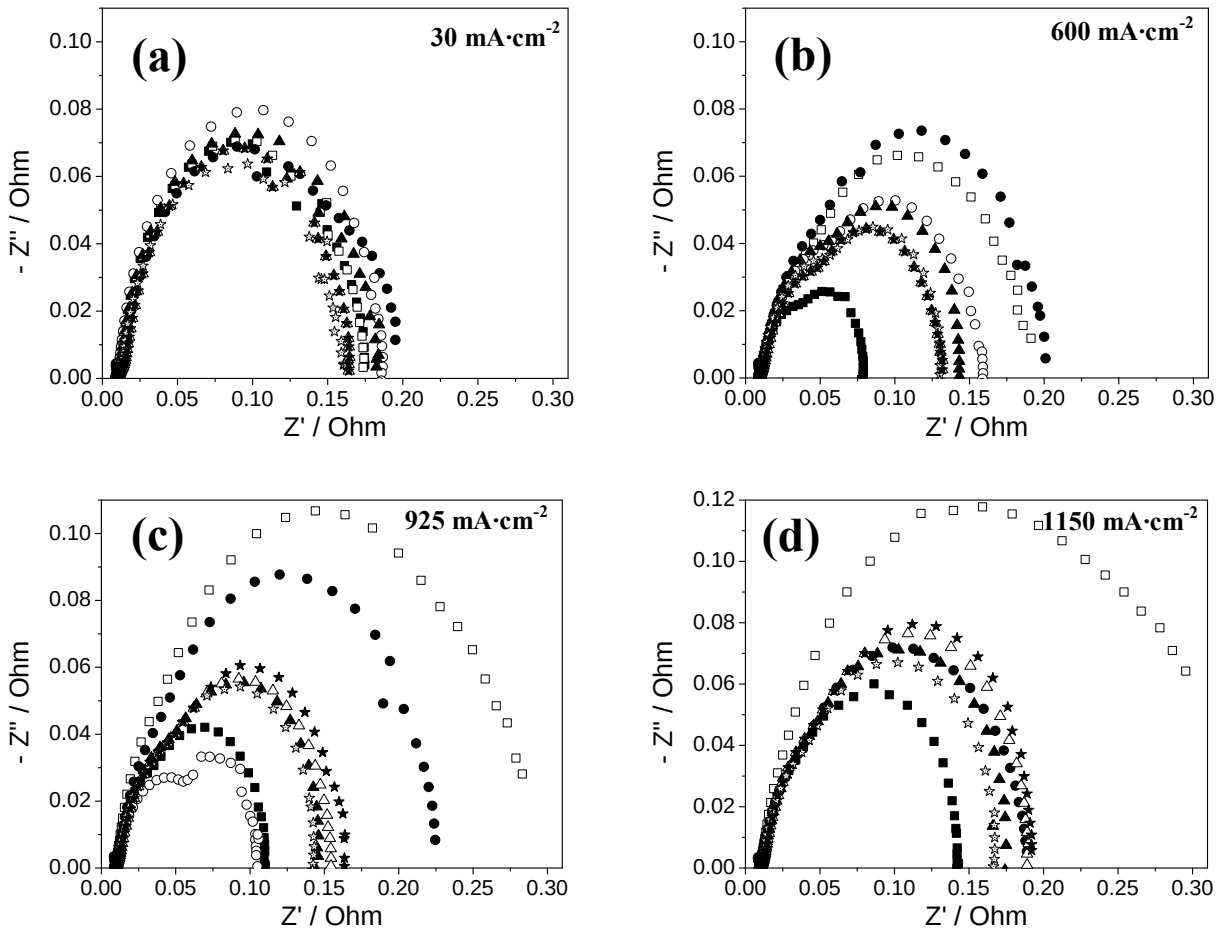

Figure 5.8 Nyquist plots of MEA1, MEA2, MEA3, MEA4, MEA5, MEA6, MEA7 and MEA8 at the current densities of a) 30, b) 600, c) 925 and d) 1150 mA·cm^{-2} at 65 °C. The symbols are identified as the following: ■ MEA1, □ MEA2, ● MEA3, ○ MEA4, ▲ MEA5, △ MEA6, ★ MEA7 and ☆ MEA8. The impedance measurement of MEA4 was not performed at 1150 mA·cm^{-2} due to a lower voltage than 0.2 V.

Fuel cells undergo three fundamental limitations when an AC voltage applied: The first is called as “kinetic” limitation and can be described as charge transfer activation, the second is described as Ohmic limitation including the ion and electron transport losses, and the third considers the mass transfer limitation and can be called as concentration polarization due to the flooding of the catalyst layer and the GDL [38]. The MEAs were characterized at the current densities of 30, 600, 925, 1150 mA·cm^{-2}. For the kinetic region, 30 mA·cm^{-2} was selected since the minimum flow rates of the feed gases, oxygen and hydrogen were higher than required. This region generally gives information about the ORR at the cathode. At a current density of 600 mA·cm^{-2}, the resistance to the flow of electrons from the Pt electrocatalyst to the external current collectors and the resistance of ion transport

through the membrane dominated on the MEA performance. Flooding started to dominate at a current density of 925 mA·cm^{-2} which was selected as another measurement point. The current density at 1150 mA·cm^{-2} was strongly influenced by flooding.

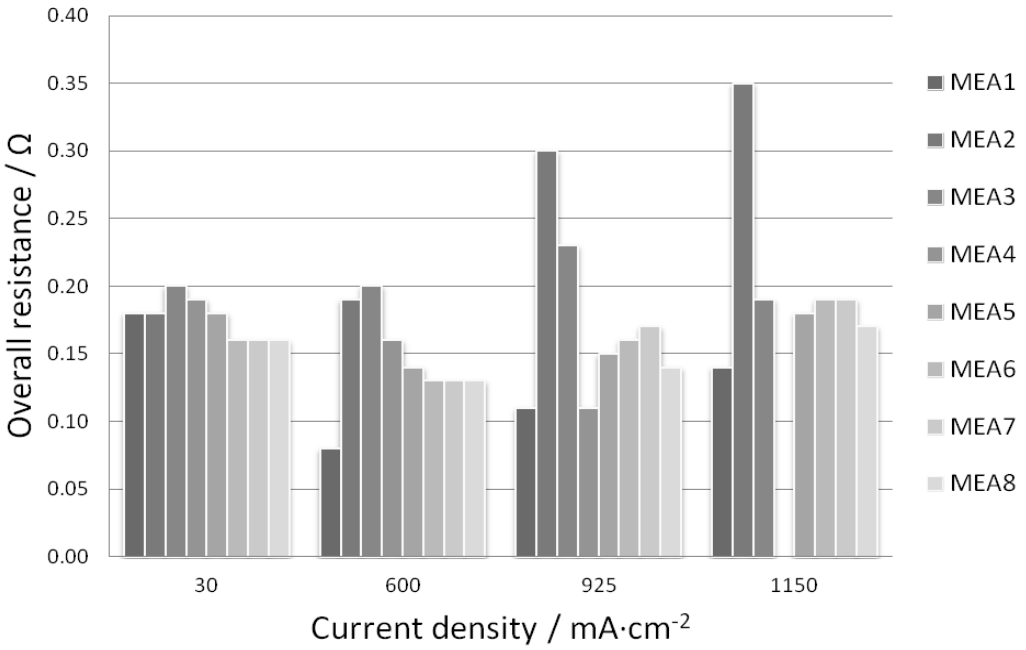

Figure 5.9 Overall resistances of the MEAs read from Figure 5.8. Resistances have an error of ±0.01 Ω. The impedance measurement of MEA4 was not performed at 1150 mA·cm^{-2} due to a lower voltage than 0.2 V.

In Figure 5.8, it is observed that except for the impedance plot of MEA4 at the current density of 925 mA·cm^{-2}, the two semicircles shown in Figure 5.7 are overlapping in all EIS measurements. Therefore, it is difficult to make a comment on the kinetic and mass transport contributions to the overall resistance. The intersection of the high frequency arc with the real axis provides the membrane resistance, measured as 0.01 Ω for all MEAs. The overall resistances of the MEAs are shown in Figure 5.9. The overall resistance of MEA1 decreased when the current density increased to 600 mA·cm^{-2}. This is an expected behavior since the kinetic contribution to the resistance decreased and mass transport resistance did not contribute to the overall resistance at this current density. However, going to the higher current densities starting from 600 mA·cm^{-2}, mass transport limitations start to dominate, thereby, the overall resistance increases. This type of behavior

was observed for MEA5, MEA6, MEA7 and MEA8. The overall resistance of MEA2 increased gradually due to the worse water management. Contrarily, the overall resistance of MEA3 was lower at 1150 $mA \cdot cm^{-2}$ compared to 925 $mA \cdot cm^{-2}$ suggesting a change in water distribution within the CNF layer due to the increased total gas flow rate.

5.4 Concluding remarks

This comprehensive study on the use of CNFs as a MPL in PEM fuel cells suggested that the electrochemical performance of the PEM fuel cells was strongly influenced by the hydrophilic or hydrophobic character of the gas diffusion layer and its overall resistance. The following major conclusions can be drawn from this study.

1) The GDL 25 BC performed better with respect to polymer loaded CNF grown carbon papers at the stoichiometric ratios of 1.25 for the anode and 2.0 for the cathode.

2) As long as the stoichiometric ratios were increased to 3.0 for the anode and 4.0 for the cathode, the electrochemical performances increased for the MEAs where polymer loaded CNF grown GDLs were applied only at the cathode.

3) Crosslinking of PDMS modified PSMA was a necessity for its use in the PEM fuel cell operation.

4) At high current densities, 19.2 wt.% PTFE loading on the CNF-carbon paper electrode showed better performance than 10 wt.% PTFE loading, however, the stability in both cases was not influenced by polymer loading.

5) Flooding observed in between 400-800 $mA \cdot cm^{-2}$ (MEA2) disappeared by loading 19.2 wt.% PTFE only at the cathode (MEA6) or nearly 10 wt.% PTFE both at the cathode and anode (MEA7).

6) Considering the performance of the reference MEA at 65 °C, 10 wt.% PSMA-CNF-carbon paper employed on both sides of MEA8 performed slightly better than 10 wt.% PTFE-CNF-carbon paper employed on both sides of MEA7. Increasing the temperature to 80 °C, PTFE took the lead compared to PDMS-PSMA. Stability was not influenced by the polymer type.

7) Flooding was not influential on hysteresis at 80 °C compared to 65 °C for all MEAs.

8) The overall resistance of the polymer-CNF-carbon paper used only at the cathode increased at high current densities due to the high degree of flooding.

9) CCM employed in MEA4 did not have identical ESA with the other CCMs determined by Cyclic Voltammetry. This limited the comparison of electrochemical performance with other MEAs.

10) The stability of the MEAs was influenced by the heterogeneous loading of the hydrophobic polymer on CNFs. Homogeneous loading of the polymer can prevent the water accumulation on the GDL.

In conclusion, some of the MEAs studied in this work reached the performance of the reference MEA at low stoichiometric ratios at the operating temperatures of 65 and 80 °C. The increase in gas stoichiometry results in a better performance while using the CNF grown carbon paper at the cathode. The humidification of the feed gases should be decreased to avoid flooding at low current densities and to obtain a better performance at high current densities.

Appendix: Leak tests and conditioning

Leak tests and conditioning of the MEAs were performed before starting the electrochemical performance tests. The MEAs were fabricated attaching the electrodes and membrane on top of each other. The mechanical compression applied on the MEAs exerted a pressure of 5 bar. Despite using a Teflon gasket on both sides of the MEA, a gas leakage can occur reducing the fuel cell performance and can make the comparison of the polarization curves meaningless. In addition to that, the permeability of hydrogen through the membrane increases with increased humidification level in the membrane [45]. Due to the operation of the MEAs in a fully humidified environment and assembling technique necessitate a leak test before starting any performance measurements.

The leak tests were performed for two minutes setting the cathode flow to zero and anode flow to 20 $ml \cdot min^{-1}$. After 120 seconds, among all the MEAs, only voltage of MEA5 dropped to 0.3 V (Figure 5.A.1). In the electrochemical performance measurements, the minimum cathode flow rate was set at 40 $ml \cdot min^{-1}$ and anode flow rate was set at 20 $ml \cdot min^{-1}$. The pressure exerted on the membrane from the cathode towards anode was always higher decreasing the rate of hydrogen crossover. Therefore, if the voltage does not drop suddenly below 0.2 V in 30 seconds, the hydrogen crossover is generally in the acceptable range. The hydrogen crossover observed in MEA5, therefore, does not influence the electrochemical performance measurements.

After the leak test, the MEAs should be conditioned in order to obtain steady state performance of the Pt catalyst. Manthiram et al. showed that the conditioning does not influence the catalyst activity, oxygen transport or membrane resistance but it affects the membrane hydration in the steady state operation of a direct methanol fuel cell [41]. In our measurements, the reference MEA, MEA1, showed a current density increase up to the 6^{th} cycle and then the maximum current density did not change for the last four cycles. The amount of current driven by the cell was about 1450 $mA \cdot cm^{-2}$ and maintained in the other cycles. MEA2 showed a

maximum at 1590 mA·cm^{-2} and then decreased to 1570 mA·cm^{-2} at the final cycle. This showed that the activation of the cell was completed at the end of cycle 3, however a subsequent degradation was observed. Nevertheless, the current density obtained at 0.2 V was 120 mA·cm^{-2} higher than MEA1 where the Pt loadings were the same in both CCMs. This shows a significant performance increase for the PTFE loaded CNF grown carbon paper at the stoichiometric ratios 2 for the anode and 2 for the cathode. MEA3 (non-crosslinked 5.1 wt.% PSMA-30 loaded CNF grown carbon paper at the cathode and GDL 25 BC at the anode) reached to its highest performance after its fourth conditioning cycle (from 1495 mA·cm^{-2} to 1540 mA·cm^{-2}) and then decreased gradually to 1525 mA·cm^{-2}. MEA3 performed better than MEA1 after 10 conditioning cycles. When the PTFE deposited CNF grown carbon paper (MEA4) was used at the anode, a linear increase for the current density values was observed. However, the final current density value was around 1150 mA·cm^{-2}. This value was much lower than the same value obtained for similar CNF grown carbon paper used at the cathode of MEA2. The activation cycles of MEA4 showed an unstable behavior at 0.2 V. Sudden voltage fluctuations indicated a flooding problem which was also observed in stability analysis. This might be due to the inhomogeneous PTFE deposition on the CNF grown carbon paper. MEA5 presented a current density of 1425 mA·cm^{-2} after the first cycle and 1400 mA·cm^{-2} at the last cycle (Figure 5.A.3). The difference between the maximum current densities of the crosslinked and non-crosslinked (MEA3) PSMA30 loaded CNFs grown carbon paper was around 125 mA·cm^{-2}. When the conditioning of MEA6 is compared with MEA2, it is seen that the maximum current density at the applied stoichiometric ratios was 170 mA·cm^{-2} higher for MEA2 which had lower PTFE loading. MEA7 and MEA8 were prepared by using PTFE and PSMA30 loaded CNF grown carbon papers on both sides of the MEAs. The difference between MEA7 and MEA2 is the change of GDL 25 BC at the anode. Both MEAs showed stable activation cycles whereas the highest current density obtained in MEA7 was lower than the highest current density obtained in MEA2. The highest current density obtained at the last activation cycle was the same for MEA5 and MEA8.

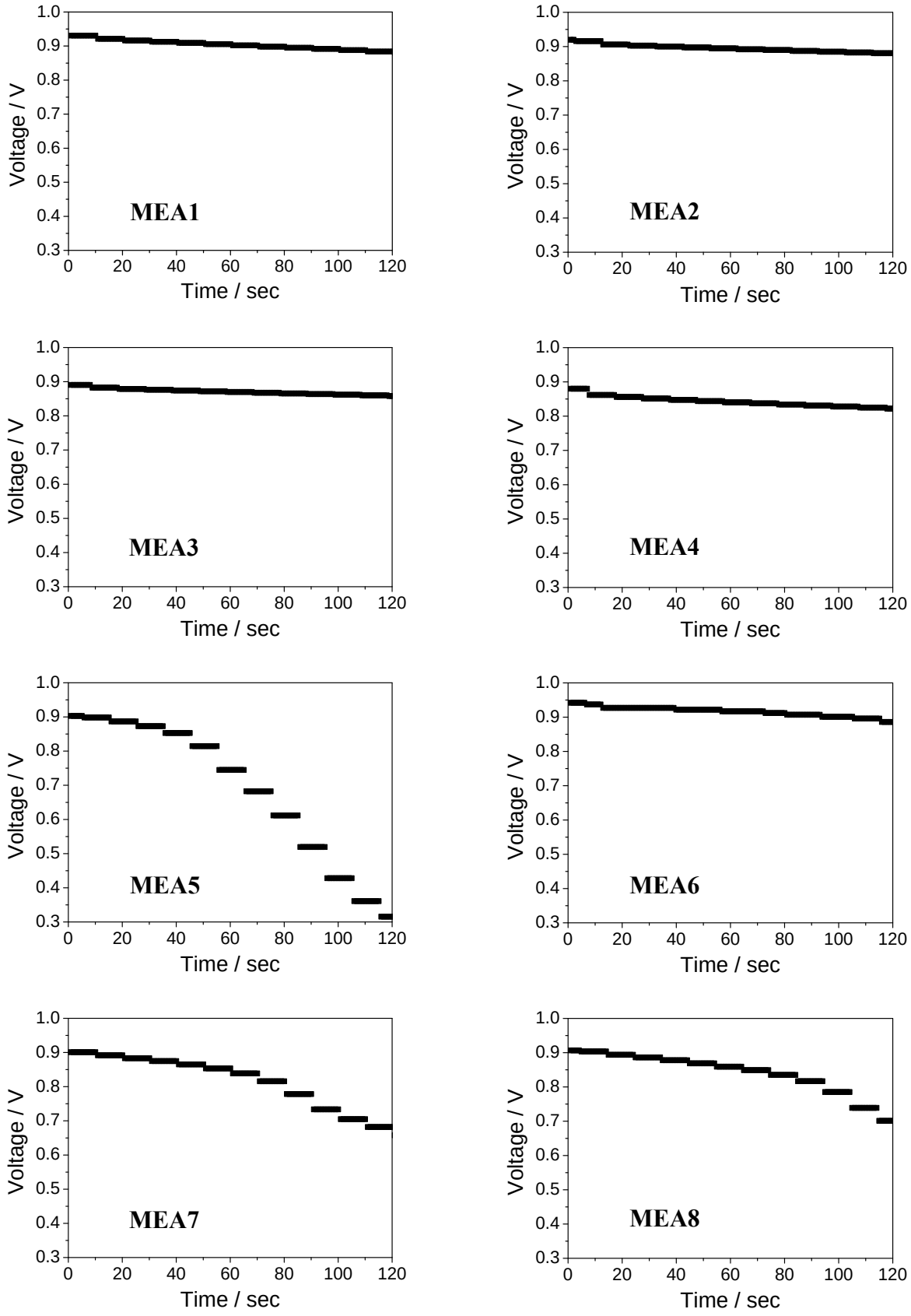

Figure 5.A.1 Leak tests of the MEA1, MEA2, MEA3, MEA4, MEA5, MEA6, MEA7 and MEA8.

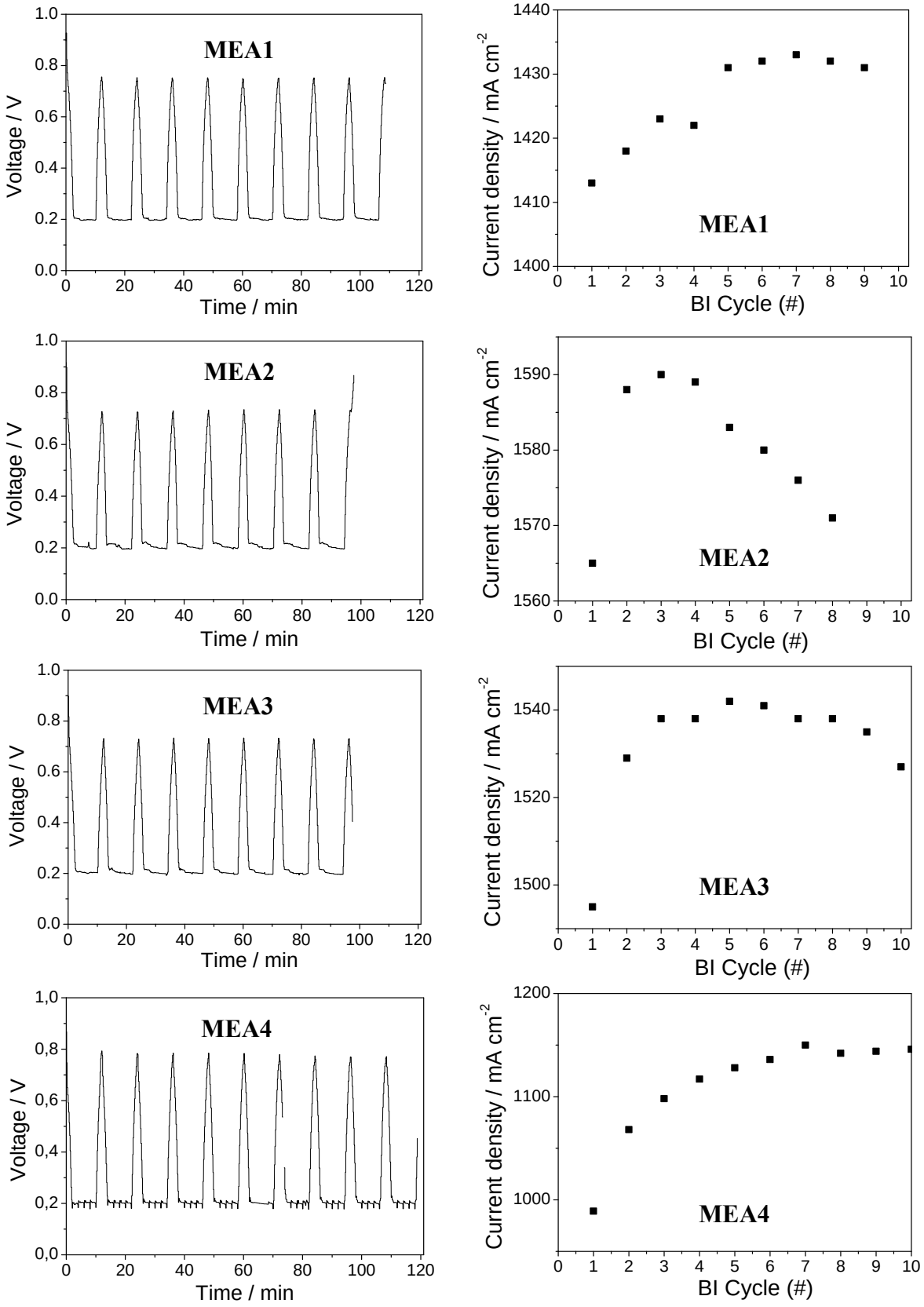

Figure 5.A.2 Conditioning (activation) cycles and corresponding current density values at the end of each conditioning cycle of the MEA1, MEA2, MEA3, and MEA4. BI represents Break-In which is frequently used in fuel cell terminology instead of conditioning cycle.

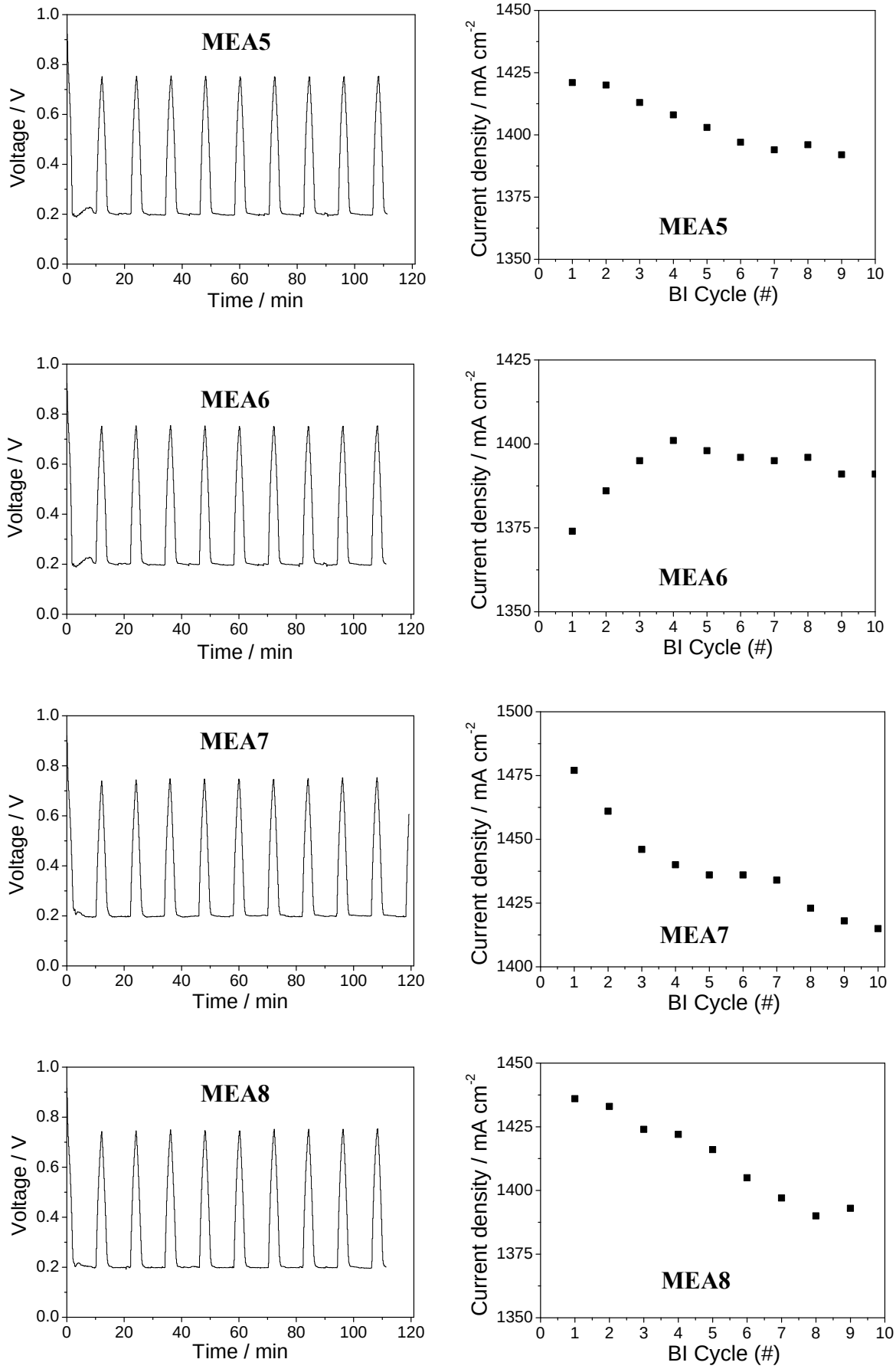

Figure 5.A.3 Conditioning cycles and corresponding current density values at the end of each conditioning cycle of the MEA5, MEA6, MEA7, and MEA8.

References

[1] R.F. Keeling, S.C. Piper, A.F. Bollenbacher, J.S. Walker, Carbon Dioxide Information Analysis Center, Oak Ridge National Laboratory, 2009.
[2] A.B. Stambouli, Renewable & Sustainable Energy Reviews, 15 (2011) 4507-4520.
[3] A. Veziroglu, R. Macario, Int J Hydrogen Energy, 36 (2011) 25-43.
[4] R.K. Ishii, First Int Conference on Energy Efficiency and Conservation, Hong Kong, 2003, pp. 57-73.
[5] F.T. Wagner, B. Lakshmanan, M.F. Mathias, J Phys Chem Letters, 1 (2010) 2204-2219.
[6] F.A. de Bruijn, Int Workshop on Advanced Material for New and Renewable Energy, AIP, Jakarta (Indonesia), 2009, pp. 3-12.
[7] K. Jiao, X. Li, Prog in Energy and Combustion Science, 37 (2011) 221-291.
[8] Z.J. Lu, M.M. Daino, C. Rath, S.G. Kandlikar, Int J Hydrogen Energy, 35 (2010) 4222-4233.
[9] W. Dai, H. Wang, X.-Z. Yuan, J.J. Martin, D. Yang, J. Qiao, J. Ma, Int J Hydrogen Energy, 34 (2009) 9461-9478.
[10] M.B. Ji, Z.D. Wei, Energies, 2 (2009) 1057-1106.
[11] F.A. de Bruijn, V.A.T. Dam, G.J.M. Janssen, Fuel Cells, 8 (2008) 3-22.
[12] W. Bi, T.F. Fuller, J Power Sources, 178 (2008) 188-196.
[13] S. Zhang, X.-Z. Yuan, J.N.C. Hin, H. Wang, K.A. Friedrich, M. Schulze, J Power Sources, 194 (2009) 588-600.
[14] C.J. Tseng, S.K. Lo, Energy Conversion and Management, 51 (2010) 677-684.
[15] Z.G. Qi, A. Kaufman, J Power Sources, 109 (2002) 38-46.
[16] G.J.M. Janssen, M.L.J. Overvelde, J Power Sources, 101 (2001) 117-125.
[17] J. Chen, T. Matsuura, M. Hori, J Power Sources, 131 (2004) 155-161.
[18] U. Pasaogullari, C.Y. Wang, Electrochimica Acta, 49 (2004) 4359-4369.
[19] F. Lufrano, E. Passalacqua, G. Squadrito, A. Patti, L. Giorgi, J Appl Electrochem, 29 (1999) 445-448.
[20] G.G. Park, Y.J. Sohn, S.D. Yim, T.H. Yang, Y.G. Yoon, W.Y. Lee, K. Eguchi, C.S. Kim, J Power Sources, 163 (2006) 113-118.
[21] P.H. Maheshwari, R.B. Mathur, Electrochimica Acta, 54 (2009) 7476-7482.
[22] C.Y. Du, B.R. Wang, X.Q. Cheng, J Power Sources, 187 (2009) 505-508.
[23] E. Dujardin, T.W. Ebbesen, A. Krishnan, M.M.J. Treacy, Adv Mater, 10 (1998) 611.
[24] X. Wang, M. Waje, Y.S. Yan, Electrochemical and Solid State Letters, 8 (2005) A42-A44.

[25] I.D. Gunbas, M.E.L. Wouters, M.M.R.M. Hendrix, R.A.T.M. van Benthem, C.E. Koning, B.A.J. Noordover, J Appl Polymer Science, (2012) n/a-n/a.
[26] SGL Technologies, Germany, 2007. Available in www.sglgroup.com.
[27] T.E. Springer, T.A. Zawodzinski, M.S. Wilson, S. Gottesfeld, J Electrochem Soc, 143 (1996) 587-599.
[28] M. Coppo, N.P. Siegel, M.R.v. Spakovsky, J Power Sources, 159 (2006) 560-569.
[29] M. Amirinejad, S. Rowshanzamir, M.H. Eikani, J Power Sources, 161 (2006) 872-875.
[30] S. Park, J.W. Lee, B.N. Popov, J Power Sources, 177 (2008) 457-463.
[31] S. Park, B.N. Popov, Fuel, 88 (2009) 2068-2073.
[32] R.P. Ramasamy, E.C. Kumbur, M.M. Mench, W. Liu, D. Moore, M. Murthy, Int J Hydrogen Energy, 33 (2008) 3351-3367.
[33] F. Barbir, PEM Fuel Cells: Theory and Practice, Academic Press, 2005.
[34] J. Benziger, E. Kimball, R. Mejia-Ariza, I. Kevrekidis, AIChE Journal, 57 (2011) 2505-2517.
[35] M. Dou, M. Hou, D. Liang, Q. Shen, H. Zhang, W. Lu, Z. Shao, B. Yi, J Power Sources, 196 (2011) 2759-2762.
[36] H. Kumpulainen, T. Peltonen, U. Koponen, M. Bergelin, M. Valkiainen, M. Wasberg, VTT Tiedotteita research notes 2137 (2002).
[37] F. Gloaguen, J.M. Le´Ger, C. Lamy, J Appl Electrochem, 27 (1997) 1052-1060.
[38] J.F. Wu, X.Z. Yuan, H.J. Wang, M. Blanco, J.J. Martin, J.J. Zhang, Int J Hydrogen Energy, 33 (2008) 1735-1746.
[39] K.R. Cooper, Scribner Associates Incorporated (2008). Available in www.scribner.com
[40] Application note #11, Bio-Logic Science Instruments. Available in http://www.bio-logic.info.
[41] X. Zhao, W. Li, A. Manthiram, J Power Sources, 201 (2012) 37-42.
[42] M. Hunsom, EIS for PEM fuel cells, Spectroscopic Properties of Inorganic and Organometallic Compounds: Techniques, Materials and Applications, The Royal Society of Chemistry (2012).
[43] X.-Z. Yuan, C. Song, H. Wang, J. Zhang, Electrochemical Impedance Spectroscopy in PEM Fuel Cells (2010).
[44] G. Dotelli, L. Omati, P. Gallo Stampino, P. Grassini, D. Brivio, J Power Sources, 196 (2011) 8955-8966.
[45] S. Tsushima, T. Nanjo, S. Hirai, ECS Meeting Abstracts, 702 (2007) 408-408.

Platinum supported CNFs on carbon paper as PEM fuel cell electrodes

6

Abstract

The use of directly grown carbon nanofibers (CNFs) on carbon paper as a catalyst support for proton exchange membrane fuel cells was investigated. The CNFs were directly grown on carbon paper by chemical vapour deposition using nickel as a growth catalyst, which was deposited as nickel hydroxide by homogeneous deposition precipitation. Platinum (Pt) was deposited via a polyol method on the nitric acid treated CNF grown carbon paper and 0.29 mg Pt per cm^2 of carbon paper was obtained. The deposited Pt nanoparticles were characterized by TEM and SEM. The average particle size of the Pt nanoparticles was found to be 4 nm and the EDX mapping analyses revealed that the Pt nanoparticles were dispersed homogeneously. The electrochemical performance of the MEA, where Pt deposited CNF grown carbon paper was used at the cathode, remained poor due to the inefficient contact of the catalyst and Nafion ionomer. The electrochemical performance of the MEA was increased considerably by the increase in the minimum gas flow rates, providing a strong evidence for the extreme flooding at the cathode. The contact of the Nafion ionomer with the catalyst, and the superhydrophobicity of the underlying layer of the catalyst layer should be optimized in order to reveal the benefits of the CNFs as a catalyst support layer.

6.1 Introduction

Increasing demand for energy directs the energy research to renewable energy sources. The transformation of the chemical energy stored in hydrogen is a renewable energy alternative and various types of fuel cells have been investigated. Especially for transport applications, proton exchange membrane (PEM) fuel cells have received significant attention as a potential electricity generator from the chemical energy stored in hydrogen [1]. PEM fuel cells provide a high efficiency, a high energy density and low emissions to the environment compared to the internal combustion engines. A PEM fuel cell consists of an anode and a cathode, in which the anode is responsible for the hydrogen oxidation reaction (HOR) and the cathode is responsible for the oxygen reduction reaction (ORR). The platinum (Pt) catalyst used for the HOR is fast compared to the ORR, due to the sluggish ORR kinetics on Pt. Therefore, the amount of Pt used on the ORR is higher than the amount on HOR. The demand to decrease the Pt catalyst on ORR necessitates the optimization of the catalyst utilization. In order to improve the ORR kinetics, two approaches are developed: The first is the improvement or a replacement of the catalyst used in the ORR [2-6] and the second is the implementation of different catalyst supports [7-14].

Under the highly oxidizing conditions of the anode compartment of the PEM fuel cells, a catalyst support should have a good corrosion resistance, provide a low electric resistance and offer a highly accessible area for the gas transport to the catalyst surface. Although the currently used carbon supports, like Vulcan XC-72R, provide some sort of corrosion resistance and electric conductivity, the metal particles trapped in the pores of carbon blacks cannot be used effectively. Carbon nanofibers (CNFs) have received significant attention to meet all the requirements discussed above. They offer a highly accessible surface area, high electron conductivity and corrosion resistance compared to the carbon blacks used as a catalyst support [15, 16].

In chapters 2 and 3, the CNFs were grown directly on carbon paper to construct a rigid CNF decorated electrodes. These electrodes were applied as a water management layer without using PTFE (chapter 4) and with PTFE (chapter 5). In this chapter, the potential use of the CNFs as a direct catalyst layer is investigated and compared with a reference electrode.

6.2 Experimental

6.2.1 Preparation of Pt deposited CNF grown carbon paper

The growth of CNFs was performed via nickel hydroxide ($Ni(OH)_2$) deposition on carbon paper. For this purpose, 340 mg $Ni(NO_3)_2 \cdot 6H_2O$ was dissolved in 300 ml distilled water. The prepared solution was added into the catalyst deposition container having carbon paper (TGP-H-060, Toray, 4.0 cm in diameter and 108.5 mg). The solution was stirred continuously and heated up to 90 °C in an oil bath. The pH of the solution was adjusted using 1.0 M nitric acid solution and brought from 6.5 to 2.4. Subsequently, 175 mg Urea in 50 ml distilled water at room temperature was added. After 48 hours of continuous stirring of the solution, 3.3 mg $Ni(OH)_2$ obtained (Figure 6.1-a).

The $Ni(OH)_2$ covered carbon paper was inserted into a vertically aligned tubular reactor ($D_{internal}$ = 5.5 cm) and the gas flow was directed vertically to the carbon paper surface. The reduction of $Ni(OH)_2$ was performed at 500 °C for four hours in 10 % H_2 and balance nitrogen in 100 ml gas flow. CNFs were grown at 600 °C in the presence of 86.5 vol.% N_2, 3.5 vol.% H_2 and 10 vol.% C_2H_4 in 100 $ml \cdot min^{-1}$ gas flow. The total weight of the CNF grown carbon paper was measured as 145.7 mg, which resulted in 35 mg CNFs (24 wt.% on the carbon paper), taking into account the presence of nickel at the tip of CNFs. The sample was oxidized with 4 M nitric acid at room temperature for 2 hours and then ultrasonicated in distilled water at room temperature for half an hour. The acid treatment creates anchoring groups on the CNF surface for platinic acid adsorption as well as removes nickel crystals at the tip of CNFs. The SEM picture taken after 30 minutes of continuous ultrasonication is shown in Figure 6.2.

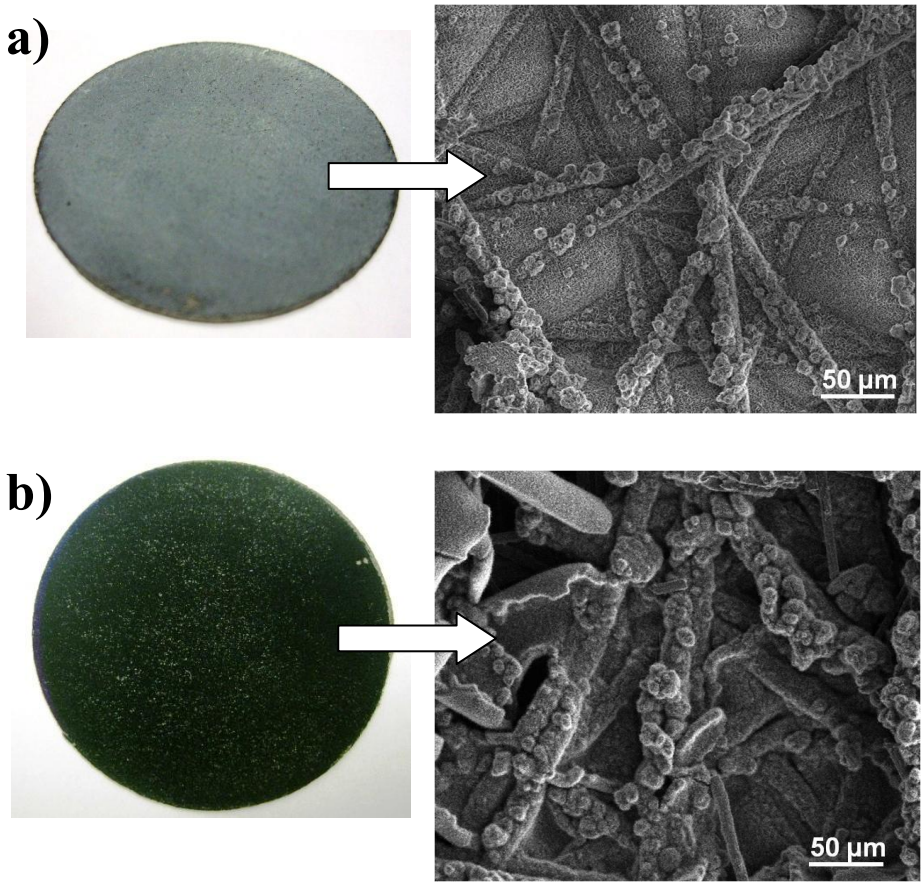

Figure 6.1 a) The image and the corresponding SEM picture of the nickel hydroxide deposited carbon paper. The pores of the carbon paper are covered by nickel hydroxide. b) The image of the carbon paper after ethylene exposure at 600 °C. The pores of the carbon paper are covered by CNFs forming a spider network around the fibers of the carbon paper.

The deposition of Pt on CNFs was performed via a polyol method. 90 mg Chloroplatinic acid (8 wt.% solution in water, Sigma-Aldrich) solution was dissolved in 2 ml ethylene glycol at room temperature. The CNF grown carbon paper was dipped into this solution. The solution pH was adjusted to 8.0 with KOH and it was heated to 130 °C for half an hour and then cooled down to room temperature resulting to a Pt loading of 0.29 $mg.cm^{-2}$ on the CNF grown carbon paper. After washing and drying the carbon paper at room temperature, the Pt-CNFs was reduced further in 50 $ml \cdot min^{-1}$ H_2 flow for an hour to obtain fully reduced Pt nanoparticles on CNF surface. A detailed discussion on the polyol method for the Pt deposition on CNFs was given by Lee et al [17].

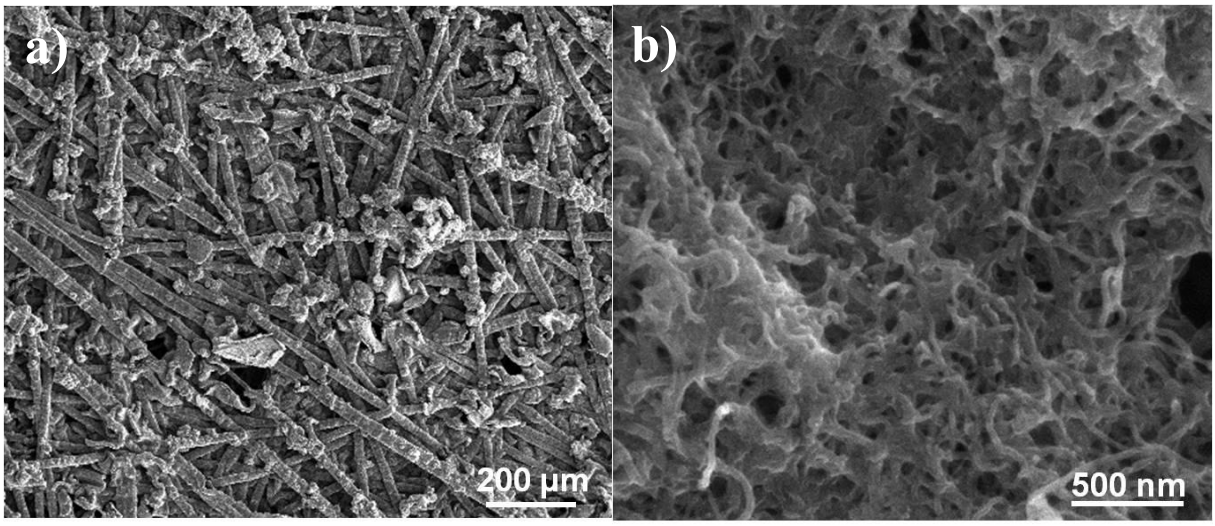

Figure 6.2 a) The SEM image of the CNF grown carbon paper after acid treatment and ultrasonication b) magnified view of the picture shown in a.

Transmission electron microscope (TEM) images were recorded with a FEI Tecnai G2 Sphera operated at an accelerating voltage of 200 kV. For TEM analyses, a small amount of Pt deposited CNFs was scratched from the carbon paper and suspended in ethanol. 40 µl of the suspension was put onto a carbon coated copper grid and the grid was dried at ambient temperature. ImageJ software was used for the histogram analyses of Pt nanoparticles on CNFs. Scanning electron microscopy (SEM) images of the CNFs were taken using a FEI Quanta 3D FEG. The surface of Pt deposited CNFs was mapped with Energy Dispersive X-ray (EDX) analyses to show the dispersion of Pt, oxygen, carbon and nickel on CNF surface.

6.2.2 Preparation of membrane electrode assembly

The membrane electrode assembly (MEA) was prepared using 10 % PTFE treated carbon paper (TG-060, Toray) at the anode and Pt deposited CNF grown carbon paper at the cathode (Figure 6.4). For the anode catalyst, an ink was prepared by mixing Hispec 9100 Pt (60%)/C catalyst (5%), DE1021 Nafion solution from IonPower, and 1,2-propanediol as a solvent [18]. This ink was decal printed onto EPDM (ethylene propylene diene monomer) rubber and then

transferred onto the anode side of NRE-211CS membrane at 135 °C and 34 bar for 1 minute. Nafion solution DE1021 was sprayed onto the CNF grown carbon paper to provide the proton conductivity through the catalyst layer and the membrane. The final Pt loadings were 0.14 mgPt·cm^{-2} at the anode and 0.29 mgPt·cm^{-2} at the cathode. A similar MEA was prepared as reference by printing the ink on EPDM. The decals were transferred onto the anode and the cathode side of the NRE-211CS membrane. The Pt loading at the anode amounted to 0.61 mg·cm^{-2}, while at the cathode the Pt loading amounted to 0.82 mg·cm^{-2}.

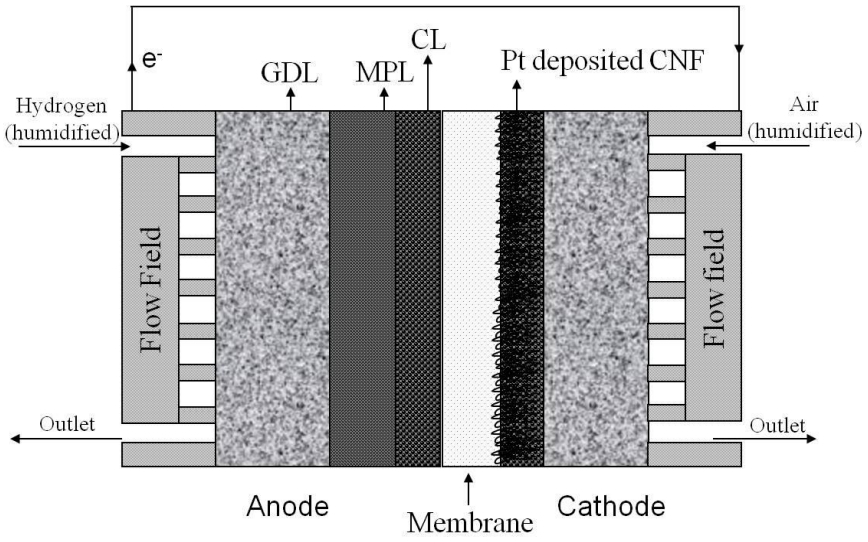

Figure 6.3 Schematic of the membrane electrode assembly with Pt deposited CNFs at the cathode. GDL: gas diffusion layer (carbon paper), MPL: microporous layer, CL: catalyst layer.

6.2.3 Cell operation and electrochemical characterizations

The MEAs with a circular active area of 8 cm^2 were installed in 5W single cell test stations located at the Energy Research Center of the Netherlands. The flow field, as already explained in chapter 4, consisted of a single serpentine structure with channel dimensions of 1x1mm cross/section at 1 mm spacing. The pneumatic cell compression used in this study was 2 bar and the sealing was provided by Viton O-rings. The minimum gas flow rates were 20 ml·min^{-1} for H_2 at the anode and 40 ml·min^{-1} for air or O_2 at the cathode. The minimum gas flow rates were increased to 250 ml·min^{-1} because of the occurrence of the flooding on the

CNF grown carbon paper. The leak tests, the conditioning cycles and the electrochemical characterization of the MEAs were performed as explained in chapter 5. The MEAs were operated with fully humidified gas feeds at 65 °C and atmospheric pressure.

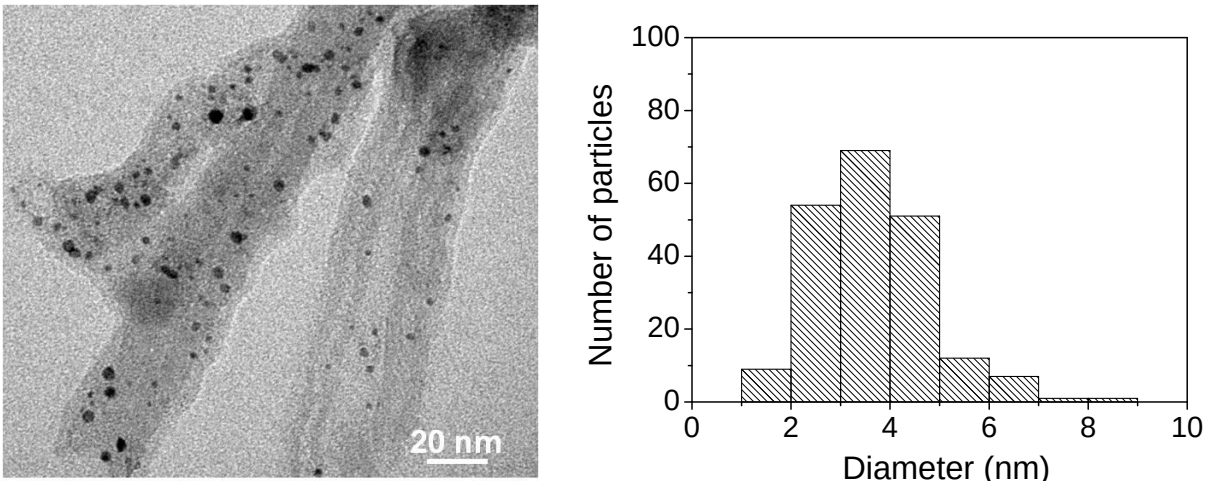

Figure 6.4 The TEM image of the Pt deposited CNFs scratched from the CNF grown carbon paper and its corresponding Pt nanoparticle histogram.

6.3 Results and discussion

The loading of $Ni(OH)_2$ on the carbon paper was calculated to be 0.26 $mg \cdot cm^{-2}$ and the corresponding CNF density obtained was 2.8 $mg \cdot cm^{-2}$. The $Ni(OH)_2$ covered the surface of the carbon paper completely as shown in Figure 6.1-a. However, the CNF growth results in openings on the carbon paper surface, indicating that the loading of CNF was not enough to completely cover the surface of the carbon paper (Figure 6.1-b). The nitric acid treatment and the ultrasonication of the CNF grown carbon paper did not result in any detachment of the CNFs from the carbon paper surface (Figure 6.2). The nitric acid treatment provides oxygen groups allowing the adsorption of platinic acid groups [19]. The reduction of the absorbed groups on the surface of CNFs in H_2 flow at 500 °C produced Pt nanoparticles with an average diameter of 4 nm (Figure 6.4). The reduction of Pt groups made the surface of the CNF surface superhydrophobic with a contact angle of 145°. This superhydrophobicity was the result of reducing the oxygen groups via

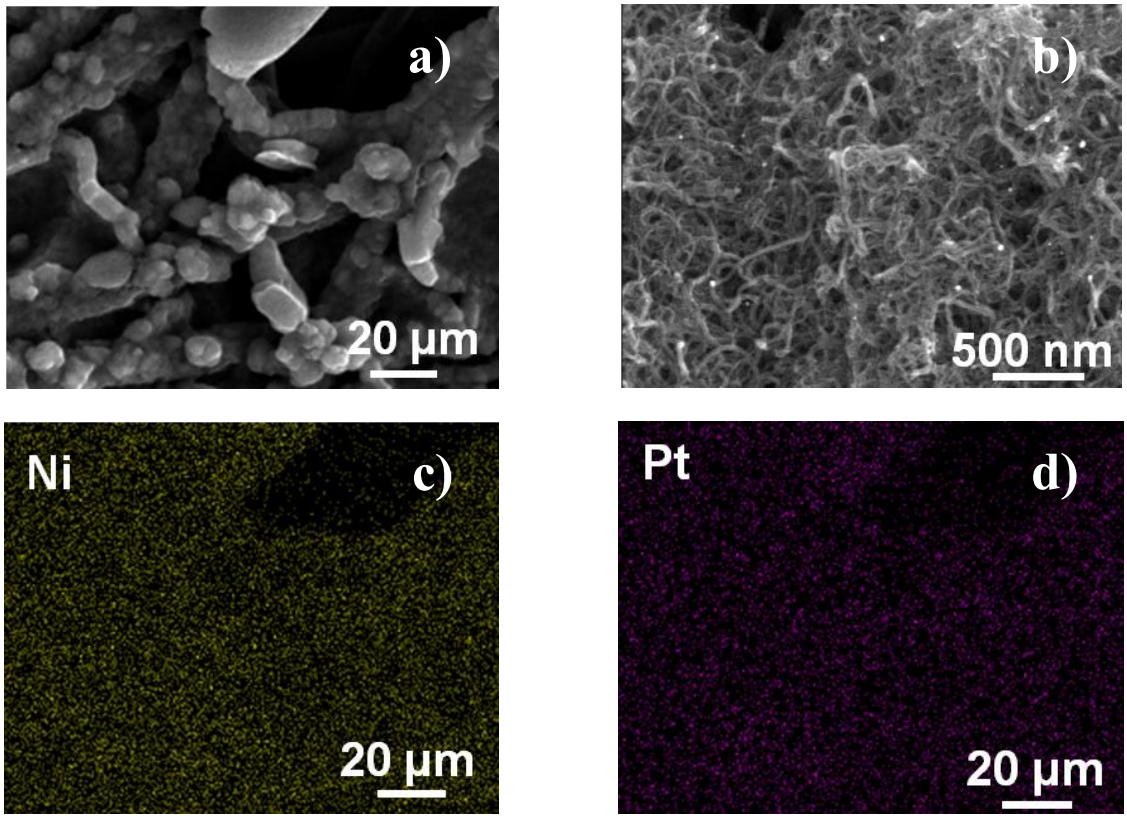

Figure 6.5 a) The SEM image of the EDX mapped area of the Pt deposited CNFs. b) Magnified view of the EDX area. EDX mapping of c) Nickel, d) Platinum.

the catalytic water formation reaction over the Pt catalyst. Attempts to reduce the oxygen groups at a temperature of 500 °C or even higher without chloroplatinic acid adsorption were unsuccessful and the CNF layer remained hydrophilic. Water was easily absorbed by the CNF layer, which was not desirable for the PEM fuel cell environment as was explained in chapter 4. The surface of the Pt supported CNFs was mapped with EDX on SEM. In Figure 6.5-a, the mapped area is shown with a magnified SEM picture in Figure 6.5-b. At the tip of the CNFs, nickel crystals are visible suggesting that the carbon encapsulation prevents the complete removal of nickel, which was also discussed in chapter 3. The mapping of nickel showed that the nickel crystals spread over the surface of CNF layer smoothly (Figure 6.5-c). The mapping of the Pt nanoparticles showed that the nanoparticles were also smoothly dispersed over the CNF layer (Figure 6.5-d). Some of the Pt can be absorbed on the carbon fibers of the carbon paper during polyol process, however, since the surface area of the CNFs is considerably higher than these

macro fibers (nearly 900 times), the adsorption of Pt is primarily occurring on the CNFs.

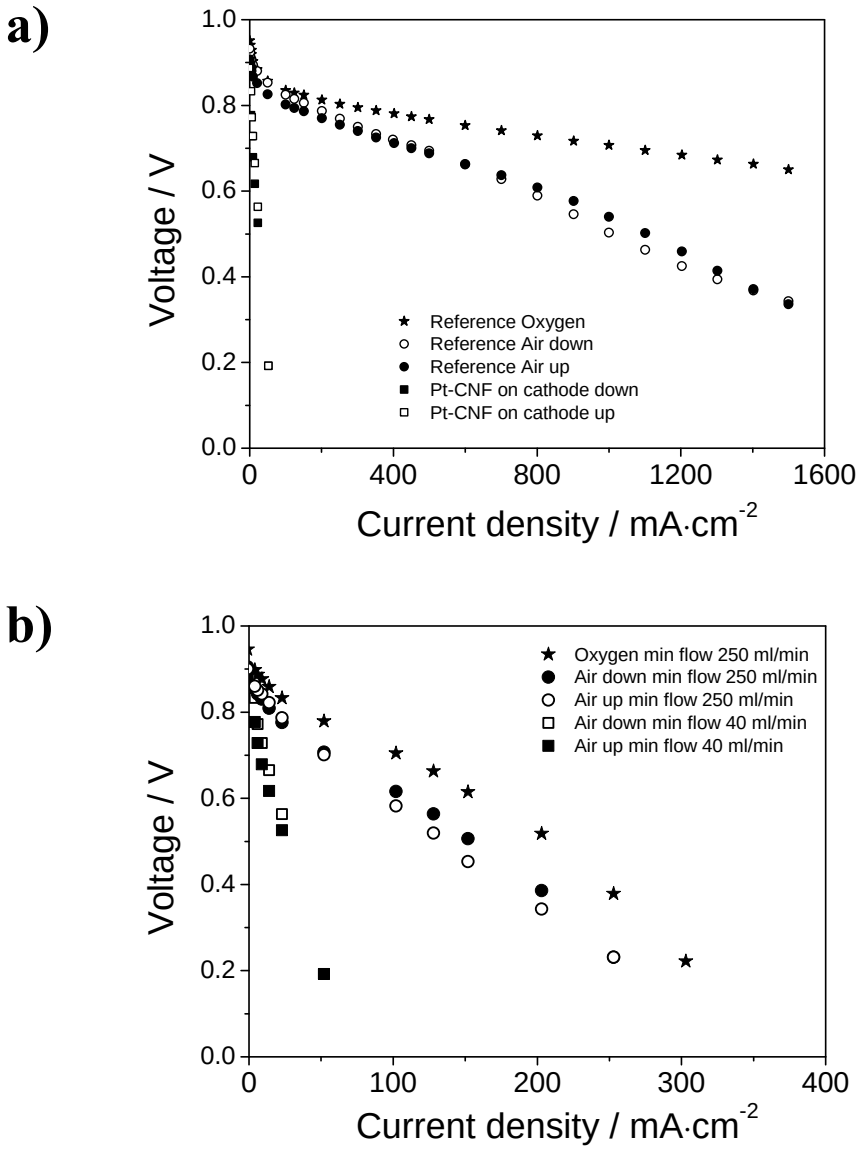

Figure 6.6 a) Polarization curves of the reference MEA and the CNF-Pt integrated MEA under oxygen and air operations at 65 °C. The poor performance of the Pt-CNF electrode inserted at the cathode is shown. b) The performance dependence on the minimum gas flow of the MEA where the electrode with Pt deposited CNFs is used at the cathode.

The electrochemical performance tests of the MEA compared to the reference MEA showed poor performance (Figure 6.6-a). The catalyst loading in the reference MEA at the anode and at the cathode was relatively higher than the MEA with Pt deposited CNFs at the cathode. Thereby, the expected performance of the reference MEA is comparable to the performance reported in chapter 4 with the

CNF grown layer. The obtained voltage is 0.72 V in oxygen and around 0.5 V in air at a current density of 1000 $mA \cdot cm^{-2}$. The reference MEA shows slight hysteresis in air operation after a current density of 800 $mA \cdot cm^{-2}$.

The use of Pt as a direct catalyst layer on CNF grown carbon paper has shown two main problems that have to be improved: inefficient Nafion contact with the deposited Pt on CNF surface and the considerable flooding within the catalyst layer. As already explained in chapter 3 (Figure 3.1), the integration scheme of the Pt catalyst onto its support is different in directly grown CNF on carbon paper compared to the activated carbon powders or the ink solutions. The ink is conventionally prepared with three components: Nafion ionomer, catalyst and catalyst support. Pt catalyst is deposited via impregnation, ion exchange or polyol processes and then the Nafion solution is proportionally mixed and stirred to make a proper contact with Pt on carbon. In the case of CNF grown carbon paper, Pt is deposited using the polyol process and therefore, ink preparation is not required. As depicted in Figure 6.6-a, the performance of such an electrode fails because of the inefficient Nafion contact with the Pt. Most of the Pt nanoparticles are not used in the ORR which thereby becomes a kinetically limited reaction. The performance of the cell is measured to be lower than 0.2 V at a current density of 50 $mA \cdot cm^{-2}$.

Wang et al. measured the electrochemical performance of an MEA prepared by carbon nanotubes (CNTs) grown directly on a cobalt electrodeposited carbon paper and reported a much lower performance than the performance of the CNF integrated MEA reported in this research [20]. They attributed this lower performance to the bigger Pt nanoparticles and claimed that the conventional electrodes with the same Pt loading gives a much better performance. Gangeri et al. discussed the use of Pt on carbon nanostructures on a 1 cm^2 MEA, reaching Pt nanoparticle sizes around 2 nm and reported even much lower performances although the Pt loadings on both anode and cathode were around 0.4 $mgPt \cdot cm^{-2}$ [21]. Waje et al. applied the CNTs on the cathode part of the MEA and reported a very high performance reaching 0.6 V at a current density of 300 $mA \cdot cm^{-2}$ with a Pt

catalyst loading lower than 0.1 $mg \cdot cm^{-2}$ [22]. However, there is no discussion about the Nafion-Pt contact and hydrophobicity of the CNTs after Nafion loading.

The effect of the flooding on the CNF grown layer was investigated by increasing the minimum gas flow rate supplied to the cathode compartment Figure 6.6-b. Here the minimum gas flow rates were increased from 40 to 250 $ml \cdot min^{-1}$ both for the cathode and the anode. The increase in the minimum gas flow rate is necessary for the anode as well in order to prevent a large pressure difference on the anode and the cathode compartment, which can cause pinhole formation in the membrane. The increase in the minimum gas flow improved the performance and the voltage obtained at a current density of 250 $mA \cdot cm^{-2}$ is around 0.2V in air operation. Therefore, the catalyst layer composed of Nafion and Pt deposited CNFs is hydrophilic which results in a water film formation. The voltage loss is mainly due to the poor catalyst utilization for both the oxygen and air operations shown in Figure 6.6-a.

6.4 Concluding remarks

This chapter presents the use of CNF grown carbon paper as a catalyst support at the cathode compartment of a PEM fuel cell. The deposition of Pt on CNFs via polyol process and its subsequent reduction in hydrogen formed homogeneously dispersed Pt nanoparticles on CNFs confirmed by TEM and SEM investigations. The CNF growth catalyst, nickel, was not completely removed by the nitric acid treatment due to the encapsulation of carbon on the nickel crystals. The electrochemical performance tests of the MEA showed a poor performance compared to the conventional carbon bulk Pt catalysts due to the two main reasons:

1- The poor contact with the Nafion ionomer with the Pt nanoparticles decreases the effective catalyst utilization of Pt catalyst.

2- Nafion spraying makes the catalyst layer hydrophilic resulting in extreme flooding within the catalyst layer.

To solve these two problems, PTFE loading on the Pt supported CNF layer should be varied and the electrochemical performance should be measured with different gas flow rates. Another alternative of providing a good proton contact is to modify the Nafion ionomer with a group which directly binds to the exterior surface of the Pt nanoparticles. After a sufficient heat treatment in this way, Pt nanoparticles can be used effectively.

The objectives of the use of directly grown CNFs on the carbon paper were to provide a strong network of CNFs around the fibers of the carbon paper and to improve the catalyst utilization using CNFs which have more open surface with respect to carbon blacks used in the conventional catalysts. The poor performance of the Pt deposited CNF electrode is due to the poorly optimized Nafion Pt contact. Further experiments on this optimization are necessary to explore the benefits of using directly grown CNFs in PEM fuel cells.

References

[1] F. de Bruijn, Green Chem, 7 (2005) 132-150.
[2] K. Kwon, K.H. Lee, S.A. Jin, D.J. You, C. Pak, Electrochemistry Communications, 13 (2011) 1067-1069.
[3] K. Jayasayee, PhD Thesis, Eindhoven University of Technology, Eindhoven, 2011, pp. 183.
[4] Li, J.L. Qiao, D.J. Yang, J.S. Zheng, J.X. Ma, J.J. Zhang, H.J. Wang, Electrochimica Acta, 54 (2009) 5614-5620.
[5] H. Boennemann, G. Khelashvili, Appl Organometallic Chem, 24 (2010) 257-268.
[6] E. Antolini, Energy & Environmental Science, 2 (2009) 915-931.
[7] B. Seger, A. Kongkanand, K. Vinodgopal, P.V. Kamat, J Electroanalytical Chem, 621 (2008) 198-204.
[8] J.P. Dodelet, D. Villers, S.H. Sun, A.M. Serventi, S. Desilets, J Phys Chem B, 110 (2006) 25916-25925.
[9] I. Kvande, S.T. Briskeby, M. Tsypkin, M. Ronning, S. Sunde, R. Tunold, D. Chen, Top Catal, 45 (2007) 81-85.
[10] F. Yuan, H.K. Yu, H. Ryu, Electrochimica Acta, 50 (2004) 685-691.
[11] P. Ramesh, M.E. Itkis, J.M. Tang, R.C. Haddon, J Phys Chem, 112 (2008) 9089-9094.
[12] W.Z. Li, C.H. Liang, W.J. Zhou, J.S. Qiu, Z.H. Zhou, G.Q. Sun, Q. Xin, J Phys Chem B, 107 (2003) 6292-6299.
[13] A. Caillard, C. Charles, R. Boswell, P. Brault, Nanotechnology, 18 (2007) 1-9.
[14] E. Antolini, E.R. Gonzalez, Solid State Ionics, 180 (2009) 746-763.
[15] X. Wang, W.Z. Li, Z.W. Chen, M. Waje, Y.S. Yan, J Power Sources, 158 (2006) 154-159.
[16] Y.Y. Shao, G.P. Yin, Y.Z. Gao, P.F. Shi, J Electrochem Soc, 153 (2006) A1093-A1097.
[17] K. Lee, J.J. Zhang, H.J. Wang, D.P. Wilkinson, J Appl Electrochem, 36 (2006) 507-522.
[18] G.J.M. Janssen, E.F. Sitters, A. Pfrang, J Power Sources, 191 (2009) 501-509.
[19] S. Sun, D. Yang, G. Zhang, E. Sacher, J.P. Dodelet, Chem Mater, 19 (2007) 6376-6378.
[20] C. Wang, M. Waje, X. Wang, J.M. Tang, R.C. Haddon, Y.S. Yan, Nano Letters, 4 (2004) 345-348.
[21] A. Gangeri, G. Centi, A. La Malfa, S. Perathoner, R. Vieira, C. Pham-Huu, M.J. Ledoux, Catal Today, 102 (2005) 50-57.

[22] M.M. Waje, X. Wang, W.Z. Li, Y.S. Yan, Nanotechnology, 16 (2005) S395-S400.

7 Conclusions and outlook

7.1 Conclusions

This thesis demonstrates two distinct preparation techniques of CNF growth on carbon paper and provides a comprehensive understanding for the application of the produced CNF grown carbon papers as a water management layer and a direct catalyst layer in a proton exchange membrane (PEM) fuel cell. The growth of CNFs on carbon paper was performed according to the requirements of the PEM fuel cell operation elucidated from preliminary single cell measurements. Various factors were considered in the development and application of CNF grown carbon papers including; the choice of the CNF growth catalyst, remaining growth catalyst on CNFs, and the catalyst and CNF loading on the carbon paper as well as surface homogeneity and hydrophobicity, and CNF layer thickness.

The first preparation method presented in chapter 2 was the usage of nickel complex particles for the growth of CNFs on carbon paper. It was shown that particles composing of nickel hydrazine chloride and nickel ammine chloride can be selectively deposited either throughout or on a single side of carbon paper by using different dispersing solvents. The deposition of the CNF growth catalyst was rather fast since pre-synthesized particles were dispersed in a suitable solvent,

simply shaken and then applied directly on the carbon paper. In this way, the nickel complex particles are physically attached on carbon fibers but reduced later at a high temperature in hydrogen, which chemically attached them on the surface of carbon fibers. However, the control of the loading of the nickel particles on the carbon paper was rather poor, which in turn affected the control of the loading of CNFs. Nevertheless, CNF layer was grown on the carbon paper with the required properties such as porosity (> 50 %) and homogeneity covering all the carbon fibers on the top surface of the carbon paper.

The need for a better control on the loading of the nickel catalyst on the carbon paper directed us to implement a new method which is called homogeneous deposition precipitation (HDP) of nickel (chapter 3). HDP of nickel on powdered supports was previously applied in many studies, however, it has not been reported before in literature for carbon paper. Selective $Ni(OH)_2$ deposition on a single side of the carbon paper was achieved by making use of the hydrophobic nature of the carbon paper. The deposition of $Ni(OH)_2$ in this manner resulted in repeated leaflets on the carbon paper and covered the entire carbon paper surface after 72 hours of deposition. The leaflet texture formed a spongy structure on the carbon paper increasing the mass transfer of the carbon containing gases to the catalyst surface during the CNF growth. This resulted in an efficient usage of the nickel catalyst. CNFs were homogeneously grown on the carbon paper with an approximate layer thickness of 5 to 15 μm depending on the local density of the nickel catalyst. HDP of nickel on the carbon paper provided a better control of the nickel loading and thereby the CNF loading compared to the CNF growth method using nickel complex particles in chapter 2.

A preliminary study (chapter 4**)** was carried out to describe the effects of the introduction of CNF grown carbon paper as a gas diffusion medium in a membrane electrode assembly (MEA). The electrochemical performance of MEAs was affected by the stoichiometry, humidification and operating temperature. In this work, the hydrophobic nature of CNF grown carbon papers was not modified. It was observed that the hydrophobicity played an important role on flooding at even

low current densities due to low gas flow rates. The water hold up increased due to the large number of hydrophilic pathways within the CNF layer. However, a remarkable performance recovery was obtained at high current densities and increased gas stoichiometries of 3.0 for anode and 4.0 for cathode, suggesting an internal re-distribution of liquid water enabling superior power densities. The operation of the MEA at 80 °C in 'normal' and 'reverse' mode did not show a considerable difference in electrochemical performance. The difference between the flooding effects at 65 °C and 80 °C was attributed to the increased water vapour carriage capacity of air at a higher temperature. Dry gas feeds used in the MEA operation caused drying of the membrane and a strong hysteresis in the polarization curves.

A comprehensive study on the use of CNFs as microporous layer (MPL) in PEM fuel cells was done by constructing eight MEAs using nine distinct hydrophobic polymer loaded CNF grown carbon papers supplemented by identical commercially available MPL coated GDLs (chapter 5). The nickel loading was controlled in between 0.46-0.62 $mg \cdot cm^{-2}$, and thereby the CNF loading was kept in between 4.5-5.8 $mg \cdot cm^{-2}$. Carbon papers were integrated with commercially available catalyst coated membranes and the constructed MEAs were tested in a single cell test station. PTFE and PSMA were used to decrease the hydrophilic pathways and thereby decrease the water retention on the CNF grown carbon paper. The testing was performed at 65 and 80 °C at industrially applied stoichiometric ratios, 1.25 for the anode and 2.0 for the cathode to characterize the mass transport of the oxygen in air, specifically at high current density region. This work suggested that the electrochemical performance of the PEM fuel cells was strongly influenced by the hydrophilic or hydrophobic character of the GDL and its electron conductivity. If the stoichiometric ratios were increased to 3.0 for the anode and 4.0 for the cathode, a considerable increase was observed in the electrochemical performance of the MEAs constructed with the polymer loaded CNF grown carbon papers applied only at the cathode. When using the polymer loaded CNF grown carbon papers on both sides of the MEA, a stable and promising MEA performance

was obtained compared to reference MEA, however, the maximum power density could not surpass the reference MEA.

The use of CNF grown carbon paper as a direct catalyst support was investigated for the cathode part of an MEA (chapter 6). The overall resistance of the MEA as well as the proton conductivity of the Pt-Carbon-Nafion structures should be optimized as much as possible to obtain a good electrochemical performance. To do this, in conventional catalyst applications, Pt was deposited on carbon powder and then mixed with Nafion as homogeneous as possible. In the preparation method described here, Pt was homogeneously deposited on CNFs, however, Nafion spraying was not homogeneous on the Pt catalyst. This inhomogeneity brought poor contact with the Nafion-ionomer and Pt nanoparticles and substantially decreased the electrochemical performance. Nafion spraying caused also an increase in the hydrophilic pathways within the Pt-deposited CNF layer and therefore increased flooding even at low current densities. The objectives of the use of directly grown CNFs on the carbon paper were to provide a strong network of CNFs around the fibers of the carbon paper and to improve the catalyst utilization using CNFs, which have more open surface with respect to carbon black used in the conventional catalysts. The poor performance of the Pt-CNF electrodes was due to the poorly optimized Pt-Nafion contact.

7.2 Outlook

Direct growth of CNFs on a carbon paper is a promising approach for the development of PEM fuel cell electrodes utilizing a carbon support not only as a catalyst support material but also as a water management layer. This approach was investigated separately to explore the advantages taking into account the limits of the PEM fuel cell operation.

In this thesis, CNF growth was performed by two distinct growth methods. It was difficult to control the loading of nickel complex particles on the carbon paper since these particles were only adsorbed physically on the surface, and therefore this method was not reproducible. These particles can simply be

functionalized by a suitable chemical and in this way, the nickel loading can be controlled effectively. Nickel hydroxide deposition on carbon paper gave a better control compared to the deposition of nickel powders on the carbon paper. Besides, nickel hydroxide deposition formed a complete layer on the carbon paper whereas nickel powders attached on the walls of the carbon paper fibers and did not form a complete layer. A water management layer should not have pores over a few microns. A large pore is a cause of the local water retention and reduces the mass transport of oxygen especially at high current densities. The recommended CNF growth approach is therefore the nickel hydroxide deposition.

The growth of CNFs on a carbon paper made the carbon paper surface highly rough and increased the surface hydrophobicity after adding a sufficient amount of a hydrophobic polymer such as PTFE or PDMS modified PSMA. When CNF grown carbon paper was used as a catalyst layer without any PTFE addition, it was observed that flooding and improper Pt-Nafion contact decreased the fuel cell performance considerably. These disadvantages brought a complexity to the production of hydrophobic Pt loaded CNFs since when a hydrophobic polymer was first loaded on CNFs, the Pt catalyst could not be deposited on CNFs homogeneously. One approach to solve this problem can be the deposition of Pt on CNF as given here and then conducting experiments with different PTFE loadings to explore the benefits of introducing hydrophobicity providing a proper contact with Nafion. This challenging problem should be solved to reveal the benefits of combined water management and catalyst support properties of directly CNF grown carbon papers.

List of abbreviations

AC	Alternating Current
CCM	Catalyst Coated Membrane
CL	Catalyst Layer
CNF	Carbon NanoFiber
CNT	Carbon NanoTube
DI water	De-Ionized water
ECN	Energy Research Center of the Netherlands
EIS	Electrochemical Impedance Spectroscopy
EDX	Energy Dispersive X-ray
ESA	Electrochemical Surface Area
FRA	Frequency Response Analyser
FTIR	Fourier Transform Infrared spectroscopy
GDL	Gas Diffusion Layer
GDM	Gas Diffusion Media
HDP	Homogeneous Deposition Precipitation
HOR	Hydrogen Oxidation Reaction
H_{UPD}	Hydrogen UnderPotential Deposition
ICP	Inductively Coupled Plasma
MEA	Membrane Electrode Assembly
MPL	MicroPorous Layer
MWCNT	Multi-Walled Carbon NanoTube
OCV	Open Circuit Voltage
ORR	Oxygen Reduction Reaction
PDMS	PolyDiMethyl Siloxane

PEM fuel cell	Proton Exchange Membrane Fuel Cell
PSMA	Poly-Styrene-alt-Maleic Anhydride
Pt	Platinum
PTFE	PolyTetraFluoroEthylene
SEM	Scanning Electron Microscopy
TEM	Transmission Electron Microscopy
XPS	X-ray Photoelectron Spectroscopy
XRD	X-Ray Diffraction

Acknowledgements

I would never imagine that a country could completely change a person's life before coming to the Netherlands. There is a huge difference between "the first and the last step", which convinced me that I took the right decision to do a PhD in this lovely country. In this last section, I would like to convey my acknowledgements to the people I shared four years of my life with.

First of all, I would sincerely present my upmost gratitude for Prof.dr.ir Jaap Schouten for this life changing opportunity he offered me in joining the Chemical Reactor Engineering group at the Eindhoven University of Technology. I would like to thank my daily supervisor Xander Nijhuis whose motivation, guidance and support speeded me up in this research. His fastness and patience on reading and correcting of my draft papers was admirable. I am grateful to John and Frank for their support throughout this study and their excellent suggestions on this thesis. I would like to give special thanks to Peter Bouwman and Hakan Yıldırım who helped me in the fuel cell measurements. Without their help and guidance, I would never truly understand the behaviour of a proton exchange membrane fuel cell under different measurement conditions.

A critical factor for conducting good experiments is the need for good technical support which is excellent in the Chemical Reactor Engineering group. I would like to specially thank Frans Kuijpers from the glass department in TNO. He constructed very critical parts of my experimental setup and allowed me to produce unique materials. I express my gratitude to Erik and his colleagues for their great help and immediate solutions. I am highly grateful to Peter, Anton, Madan, Marlies and Chris for their excellent assistance. I would like to acknowledge Carlo Buijs for his great effort and patience on taking the scanning electron microscope images of my hairy carbon papers. I think he will never take the photographs of such an

amount of samples. I would like to specially thank to Denise, the best secretary that I have ever seen, for her great assistance. She had always an idea and a rather fast solution for any problem. In the four years, what I saw, she was a woman helping everyone in the group with great enthusiasm.

A PhD does not depend only on the experiments that you perform in the lab. Sometimes, you need an extra motivation while you are sitting in front of your computer and in that situation you have to have perfect office mates. Sometimes you should laugh, sometimes understand and solve the problems of your friends and sometimes celebrate something together. We did all these together with my office mates, Lidia and Narendra, in the last three years. We were the first office mates all obtaining their Dutch driving license in the same office. I will never forget the long discussions on driving issues in our cigarette breaks. Many thanks to Maria, Dulce, Faysal, Jack, Stijn, Patrick, Wim, Halabi, Ivana, Nopi, Violeta, Christine, Jovan, Fernanda, Bruno, Jiaqi and Roman with whom I shared most of my time in my PhD study.

Being in a foreign country is always difficult if you are living alone and you need many friends who can help and advise you. During my stay in the Netherlands, luckily, I had many Turkish friends with whom I shared many things. I would like to thank Ergün, Ilhan, Ahmet Koray, Başar, İlkin, Kamil, Volkan, Seda, Gözde, Bahar, Burcu, Gökhan and Uğur for their great friendship and fruitful discussions. I would like to specially thank to Barış, Doğan and Aydın. They helped and advised me the truths in the most critical days of my life. You are really the unique friends that I have ever seen.

In the last two years, I have travelled around Europe with my car which did not stranded me even a single time on the European highways after travelling more than 30,000 km. I specially thank the countries Germany, the Netherlands, Austria, Denmark, Norway and France for their excellent roads. Driving in these countries was a great pleasure for me!

Last but not least, I would like to continue in Turkish to express my gratitude for special people.

Doktora sürecim boyunca yaşadığım onca zorluktan sonra, uzunca bir sure hayatta istediği aradığı insanı bulamamış biri olarak seni bulduğum senle olduğum için kendimi çok şanslı hissediyorum. Doktoramın bitmesinde bana yardımcı olduğun ve bu kadar uzaklığa rağmen sabrettiğin için sana minnettarım. İyi ki varsın herbişeyim!

Son olarak sevgili aileme bana verdikleri sonsuz katkı için çok teşekkür etmek istiyorum. Annem Mürvet ve babam Kazım ve canım kardeşim Serhat, sizler benim bu dünyadaki en büyük mutluluğumsunuz…Herşey için, sonsuz desteğiniz için teşekkürler!

Serdar Çelebi

Eindhoven, October 2012

About the Author

Serdar Çelebi was born on March 1st, 1982 in Istanbul, Turkey. He finished high school education in 2000 in Istanbul. In the same year, he started his bachelor study in Chemical Engineering at the Middle East Technical University in Ankara, Turkey. In 2005, he obtained his B.Sc. degree in Chemical Engineering with a minor degree in Solid State Physics from the Physics department at the same university. He continued his education on Material Science and Engineering at Koç University in Istanbul, where he obtained his M.Sc. degree in 2007 with his master thesis entitled "Design and Synthesis of CdS Quantum Dots and CdS-Fe_3O_4 Hybrid Nanoparticles in Aqueous Solution". In November 2007, he joined the Chemical Reactor Engineering group at the Eindhoven University of Technology under the supervision of dr.ir. T. A. Nijhuis and prof.dr.ir. J. C. Schouten. His work was focused on the development and usage of carbon nanofibers directly grown on carbon paper for proton exchange membrane fuel cells. Since January 2012, he is employed as R&D Engineer at Turkish Petroleum Refineries Cooperation in Kocaeli, Turkey.

List of publications

Journal Articles

S. Celebi, H. Yildirim, T.A. Nijhuis, J. van der Schaaf, F.A. de Bruijn, J.C. Schouten. Carbon nanofiber grown carbon paper as a water management layer for PEM fuel cells, in preparation.

S. Celebi, I.D. Gunbas, B.A.J. Noordover, T.A. Nijhuis, J. van der Schaaf, F.A. de Bruijn, J.C. Schouten. The use of PDMS modified PSMA loaded carbon nanofibers in PEM fuel cells, in preparation.

S. Celebi, I. Kokal, T.A. Nijhuis, J. van der Schaaf, F.A. de Bruijn, J.C. Schouten. Carbon nanofiber growth on carbon paper using nickel complex particles, in preparation.

K. Jayasayee, van J.A.R. Veen, T.G. Manivasagam, **S. Celebi,** E.J.M. Hensen, F.A. de Bruijn, Oxygen reduction reaction (ORR) activity and durability of carbon supported Pt-M (Co, Ni, Cu) alloys: influence of particle size and non-noble metals, Applied Catalysis B, Environmental, 111-112 (2012) *515-526.*

S. Celebi, T.A. Nijhuis, J. van der Schaaf, F.A. de Bruijn, J.C. Schouten. Carbon nanofiber growth on carbon paper for proton exchange membrane fuel cells, Carbon, 49 (2) (2011) 501-507.

K. Jayasayee, V.A.T. Dam, M.W.G.M. Verhoeven, **S. Celebi,** F.A. de Bruijn, Oxygen reduction kinetics on electrodeposited PtCo as a model catalyst for proton exchange membrane fuel cell cathodes: Stability as a function of PtCo composition, J Physical Chemistry C,113 (47) (2009) 20371-20381.

Refereed conference proceedings

S. Celebi, T.A. Nijhuis, J. van der Schaaf, F.A. de Bruijn, J.C. Schouten, The use of directly grown carbon nanofibers on carbon paper as a microporous layer in proton exchange membrane fuel cells. Proceedings of the 22nd North American Catalysis Society Meeting, (pp. OF68-1/2) June 5-10, 2011, Detroit, Michigan, United States.

S. Celebi, T.A. Nijhuis, J. van der Schaaf, F.A. de Bruijn, J.C. Schouten, Direct carbon nanofiber growth on carbon paper by nickel catalyst for use in proton exchange membrane fuel cells. Proceedings of the Netherlands Catalysis and Chemistry Conference (NCCC-12), February 28 - March 2, 2011, Noordwijkerhout, the Netherlands.

S. Celebi, T.A. Nijhuis, J. van der Schaaf, F.A. de Bruijn, J.C. Schouten, The use of directly grown carbon nanofibers on carbon paper as a microporous layer in proton exchange membrane fuel cells. Proceedings of the 2nd Symposium Advances in Dutch Hydrogen and Fuel Cell Research, (pp. 1-1), March 24, 2011, Eindhoven, the Netherlands.

S. Celebi, T.A. Nijhuis, J. van der Schaaf, F.A. de Bruijn, J.C. Schouten, Nickel deposition effects on the growth of carbon nanofibers on carbon paper. Proceedings 21st International Symposium on Chemical Reaction Engineering (ISCRE-21), (pp. 113), June 13-16, 2010, Philadelphia, United States.

S. Celebi, T.A. Nijhuis, J. van der Schaaf, F.A. de Bruijn, J.C. Schouten, Nickel deposition effects on the growth of carbon nanofibers on carbon paper. Proceedings of the XIth Netherlands Catalysis and Chemistry Conference (NCCC XI), (pp. 297-297), March 01-03, 2010, Noordwijkerhout, the Netherlands.

S. Celebi, T.A. Nijhuis, J. van der Schaaf, F.A. de Bruijn, J.C. Schouten, Carbon nanofiber growth on graphite paper for PEM fuel cell applications. Proceedings of the Xth Netherlands Catalysis and Chemistry Conference (NCCC X), (pp. 177-177), March 02-04, 2009, Noordwijkerhout, the Netherlands.

S. Celebi, T.A. Nijhuis, J. van der Schaaf, F.A. de Bruijn, J.C. Schouten, Carbon nanofiber growth on carbon paper for fuel cell applications. Netherlands Process Technology Symposium (NPS-9), *(*pp. pp-1), October 26-28, 2009, Veldhoven, the Netherlands.

S. Celebi, T.A. Nijhuis, F.A. de Bruijn, J.C. Schouten, Carbon nanofiber growth on graphite disks and paper for fuel cells. Proceedings of the International Fuel Cell Conference (European European Fuel Cell Forum 2009), June 29– July 2, 2009, *(*pp. A0710-Abstract 099-1/6*)*, Luzern, Switzerland.